Mechanics and Development of Tarsal Cartilage Anlagen – Insights From a Human Study

A Thesis

Submitted to the Faculty

of

Drexel University

by

Roza Mahmoodian

in partial fulfillment of the

requirements for the degree

of

Doctor of Philosophy

December 2010

DEDICATIONS

I dedicate this thesis to my loving parents: to my father, my eternal sunshine, who has always supported and motivated me with his positive thinking and endless love and magnanimity ever since I can recall; and to my mother, my beloved role model, for all her sacrifices, and the love, encouragement and inspiration she has given me. I owe every bit of my being and anything I have accomplished to them.

TABLE OF CONTENTS

LIST OF TABLES

LIST OF FIGURES

Abstract

Mechanics and Development of Tarsal Cartilage Anlagen – Insights from a Human Study

Roza Mahmoodian

Sorin Siegler, Ph.D.

Franco Capaldi, Ph.D.

Fetal cartilage anlage provides a framework for endochondral ossification and organization into articular cartilage. Deficiency or retardation of these developmental processes causes musculoskeletal deformities. The mechanical environment can modulate development, highlighting the indispensable role of accurate mechanical models in reliable biomechanical analyses and improving shortcomings of models of morphogenesis. While much attention has been paid to the mechanical characterization of articular and growth plate cartilage, the need for investigating the developing cartilage anlage mechanics has not been answered. Additionally, finite element (FE) models are required for studying problems of soft tissue as they generally involve complex geometries, boundary conditions, and/or complicated material behavior. This makes the importance of FE implementation of material models evident. Furthermore, with the work on osteogenesis of limbs being predominantly focused on long bones, studying the mechanisms of endochondral ossification in short bones seems invaluable to understanding the normal growth patterns and etiology of their deformities. One such important case is the clubfoot deformity which can lead to severe handicap if untreated. The Ponseti technique, based on serial manipulation and immobilization, is commonly used to treat infant clubfoot. Despite the numerous studies describing theses deformities, little information is available on the correction mechanisms under this treatment method.

In the present study, the mechanical properties of developing cartilage anlage in near full-term human fetal talus were determined in confined and unconfined compression indicating the cartilage under study was softer and more permeable than e.g. articular cartilage. A straightforward method was formulated to model cartilage under large deformations using the strain energy function of the finite deformation biphasic theory, by directly incorporating the commonly extracted mechanical properties. A unique “human experiment” was conducted to elicit the effects of manipulation therapy of new-born clubfooted infants undergoing Ponseti treatment. Correction of anlagen deformities and positional relationships was observed in all patients. Ossification was enhanced under treatment, especially in the talus and cuboid, and was faster in clubfoot than normal. Patient-specific FE analysis was conducted suggesting the presence of a positive correlation between both the strain energy density and the pore fluid velocity magnitude with the amount of bone added between each two visits.

INTRODUCTION

Osteogenesis is the process of laying down new bone material by osteoblasts. It occurs either by intramembranous osteogenesis (the direct laying down of bone into the primitive connective tissue or mesenchyme), or by endochondral ossification (involving a cartilage precursor). Early in fetal development, the skeleton is cartilaginous. This *temporary* cartilage – which will generally be referred to as *cartilage anlagen* throughout this text - is gradually replaced by bone mostly by endochondral ossification, ending at puberty. In contrast, the cartilage in the joints remains unossified during the whole of life and is, therefore, *permanent* [1]. Deficiency or retardation of these developmental processes during fetal and postnatal development resulting from different causes lead to musculoskeletal deformities, e.g. various types of talipes (congenital clubfoot) in which the foot is twisted out of position or shape, usually with delayed growth and ossification.

The biological factors and mechanical environment cause changes in form during embryonic, fetal, and postnatal stages in normal and pathological conditions. For example, it has been previously hypothesized that the evolution of form of the growth plate follows the contours of principal tensile stresses [2] and minimum shear stress [3] under physiological loads. The state of such stresses in the tissue depends on its mechanical behavior, highlighting the indispensable role of accurate mechanical models of the tissue as a key to reliable biomechanical analyses and improving shortcomings of models of morphogenesis. Although much attention has been paid to mechanical characterization of articular cartilage and in some studies the mechanics of growth plate cartilage, there is still a need for investigating the developing cartilage anlage, of tarsus

for instance, to be able to model its mechanics. Finally, since most of the work on osteogenesis of limbs has been focused on development of long bones, gaining further insight into endochondral ossification mechanisms in short bones such as tarsal anlagen, is invaluable to the studies of etiology of deformities involving the foot and alike.

The temporary skeleton is made of cartilage. Cartilage is a composite organic matrix consisting of interstitial fluid and a solid matrix primarily constituted of two structural macromolecules, i.e. collagen fibers and proteoglycan aggregates. The biphasic theory [4] is the most traditional and the most commonly used model of cartilage which takes the interstitial fluid movement into account. The theory assumes that cartilage is composed of two intrinsically incompressible phases: an interstitial fluid phase and an isotropic, homogeneous, porous, permeable elastic solid. Since the assumption of isotropy is not very accurate for tissues with anisotropic architectural organization such as articular cartilage, various investigators have developed more complicated biphasic models (representing the solid matrix as transversely isotropic elastic [5], viscoelastic [6], fibril reinforced elastic [7], and conewise linear elastic [8]), as well as multi-phasic theories such as triphasic [9] and quadriphasic [10] theories. Despite development of more complex soft tissue theories, the biphasic theory in its early form has remained attractive owing to the relative simplicity of the experimental work needed to delineate the material properties of the tissue, and to its satisfactory predictions of tissue behavior in many cases. In one study of collagen fiber orientation and concentration of collagen and proteoglycan macromolecules in talar cartilage over a range of gestational ages in our group [11], the assumption of isotropy and homogeneity appeared reasonable for the anlage even in late fetal stages. It is still important however, to use a suitable material

model for the solid matrix that can account for large deformations while keeping the solid phase deformation within a physically reasonable bound, because soft tissues normally experience large deformations and the flow of fluid within the matrix can substantially alter the deformation of the solid phase of the tissue due to frictional drag forces. To achieve this goal, we determined the mechanical properties of developing cartilage anlage in near full-term (as the closest approximation to new-born due to its unavailability) human fetal talus (ankle "bone") by performing confined and unconfined compression tests of the tissue, and curve fitting to the constitutive equations of the finite deformation biphasic theory while taking into account strain-dependent permeability.

Finite element models are required for solving complicated biological problems where analytical solutions are infeasible, such as where complex geometries and boundary conditions are involved. The importance of finite-strain models for analysis of soft cartilage structures [12-13], as well as evaluation of the Helmholtz energy function for FE applications [14] has been demonstrated. A straightforward method [15] was formulated in this study to model cartilage under large deformations in FE programs using the strain energy function proposed by Holmes and Mow [16] for the solid matrix. The proposed method allows for directly incorporating the mechanical properties (permeability parameters, aggregate modulus and its strain dependent coefficient, and the Young's modulus (or the Poisson's ratio)) obtained from common test geometries. The constitutive model of the material was coded in as a user material subroutine (UMAT) in Fortran for use in Abaqus which allows for defining constitutive equations of custom materials (other commercial packages such as ANSYS also provide similar capabilities).

The capability of the user material subroutine in predicting the instantaneous and long-term behavior of the cartilage anlage was examined in several cases.

Clubfoot is a common birth deformity, yet with obscure etiology. A common non-surgical procedure for infant clubfoot - providing many advantages over surgical procedures and thus important to understand - is the Ponseti technique which is based on serial manipulation and immobilization. Despite the numerous amounts of studies on hand describing the deformities and comparisons between the normal and clubfeet, we have found little information on the presumed mechanism by which serial casting corrects these deformities and induces shape changes. The most common view [17-19] suggests that the casting loads produce stretching of tight ligaments, capsule and tendons which then restore more normal boney architecture. No evidence is available to support this view and no mention is made of how the abnormal shapes of the anlagen are corrected. Besides identifying the deformities and their improvement with treatment, the mechanism by which correction successfully occurs is also of great importance because it will likely explain why treatment succeeds or fails even when applied in newborn infants by attentive practitioners and with motivated, cooperating parents.

Based on surface models from MRI, we previously reported deformation and adaptation of these cartilage anlagen during treatment by manipulation and immobilization [20]. Immediate shape changes occurred following casting, and when after one week the cast was removed the anlagen did not elastically return to their original shape and position prior to casting. Furthermore, the growth rate of some of the clubfoot anlagen (mostly talus, thus the reason for selection) was faster than normal. It

was concluded that the mechanism of adaptation to the casting loads was quick deformation immediately upon cast application followed by adaptation to the new shape in the cast. These were qualitative findings which led to the motivation for quantitative studies of the mechanics and development of the new-born tarsal anlage. In the present study, we utilized the model of developing talar cartilage anlage to investigate the mechanisms of correction in non surgical treatment of clubfoot deformity in a unique "human experiment".

In summary, as most of the work on osteogenesis of limbs has been focused on development of long bones, constructing a reliable model for tarsal anlage and their development is undoubtedly invaluable. The acquired insight may then be applied to etiological studies of not only the clubfoot deformity, but also other deformities of the foot, to create a general understanding of the response of the involved tissue to mechanical loads and explore new treatment options or infer relationships between an existing treatment and the observed changes in growth pattern. Such studies can potentially provide guidance for the betterment of available treatment techniques or be employed to propose new ones.

The present thesis is organized as follows.

In Chapter 1, an overview of skeletal development, the clubfoot deformity and the common non-surgical method practiced for its treatment has been presented. Chapter 2 provides a review of experimental and theoretical work on the mechanical regulation of growth, ossification, and adaptation.

Chapter 3 provides a background on the structure and composition of bone and cartilage. Chapter 4 starts with a review of the biphasic theories of soft tissues, and is continued with a presentation of the formulation of the classical biphasic theory in finite deformations and infinitesimal strains. The reduction of the constitutive equations to the case of one dimensional compression is provided.

In Chapter 5, the materials and methods used in the study have been described. First, the mechanical testing of talar cartilage anlage is detailed followed by extraction of the material properties. Next, development of a user material subroutine based on the finite deformation biphasic theory and the experimental results has been presented. The test cases designed to evaluate the material model have also been described. Examples using this material formulation modeled in Abaqus were presented to demonstrate the advantage of a more accurate material model over a linear elastic material. The protocol for acquisition of the patients' MRI scans, reconstruction of anlage geometries, the qualitative study of correction of deformities and the quantitative analysis of the progress of ossification have been documented. Finally, the finite element study of treatment has been presented aimed at eliciting the relationship between correction and treatment induced stimulation.

Chapter 6 delivers the results obtained following the methods of Chapter 5. Chapter 7 provides a discussion of our findings and the limitations of the study, and presents ideas and directions for future work.

CHAPTER 1. SKELETAL DEVELOPMENT AND DEFORMITIES

The musculoskeletal system consists of skeletal connective tissues (bone, cartilage, and dense fibrous tissues) and muscle. Normal structure and function of depend on the formation and growth of these tissues, and their integration into the system that provides the stability and mobility of the body. This formation and organization occur in early prenatal life so that by 6 months the final form of the musculoskeletal systems is easily recognized (Figure 1.1). Disturbances of these processes cause congenital abnormalities such as congenital dislocation of the hip, clubfeet, and absence of part or all of a limb. The musculoskeletal system continues to grow and modify its form after birth until the physes (growth plates) close.

Broadly defined, congenital abnormalities occur in 6% of live births. About 3% of newborns have major structural abnormalities. At present the cause of 50-60% of birth defects is unknown. Chromosomal abnormalities contribute 6-7% of the abnormalities and specific gene mutations cause 7-8%. Environmental teratogens are responsible for 7-10% of the defects. Combined genetic predisposition with environmental factors causes the remaining 20-25% of congenital abnormalities [1].

The prenatal period of development is normally divided into embryonic (first 8 weeks of development) and fetal stages (9^{th} through 38^{th} weeks of development). During the embryonic period, all major internal and external structures are established. The fetal period mainly consists of growth and differentiation of tissues and organs that began development in the embryonic period.

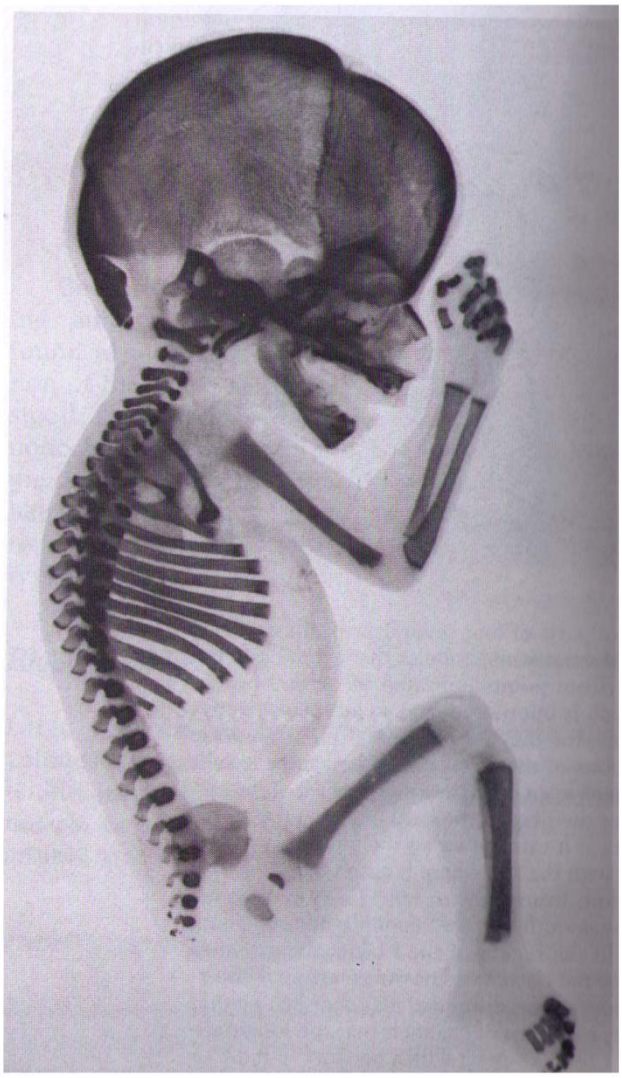

Figure 1.1. Skeletal development of a 6-month old fetus (From Turek's Orthopaedics [1]).

As early as the fifth embryonic week, the mesenchymal cells enlarge, become more compact, and differentiate into a sheet of cells recognized as pre-cartilage. Then matrix is laid down between the cells, and cartilage increases in thickness by both internal and external growth. Bone formation occurs either within mesenchymal

membranes (e.g. intramembranous formation as occurs in facial and cranial bones) or from cartilage (e.g., endochondral bone formation, as occurs long bone). In the latter case, cartilage must be removed before bone is laid down.

Intramembranous ossification – A connective tissue membrane forms the original model of the bones. Then ossification begins at one or more central points of the membrane. These centers are characterized by the appearance of osteoblasts that lay down bony trabeculae spreading radially in all directions. The tissue at the periphery differentiates into a fibrous sheath (the periosteum), the undersurface of which differentiates into osteoblasts, which in turn deposit parallel plates of compact bone (the lamellae). This periosteal ossification forms the inner and outer shells of skulls created.

Endochondral ossification – A cartilaginous model of the structure precedes destruction of cartilage and its replacement by bone. Two processes are involved: central ossification within the cartilage (endochondral ossification), and peripheral ossification beneath the perichondrium or periosteum (perichondrial or periosteal ossification). In the center of the cartilaginous precursor, the cells enlarge and become arranged radially as the matrix mineralizes. Invading blood vessels from the perichondrium bring osteoblasts that deposit new bone which replaces cartilage. As the central bone formation occurs, the cells of the inner layer of perichondrium lay down parallel layers of compact bone. The cartilaginous physes appear at the end of each long bone and produce endochondral bone throughout skeletal growth. Periosteal ossification contributes to growth of thickness of the structure.

The Pediatric Foot

There are 26 bones in the foot with many articulations (Figures 1.2, 1.3). Anatomically, the foot can be divided into three sections: forefoot (consisting of metatarsals and phalanges), midfoot (comprised of cuneiform, cuboid, navicular), and hindfoot (calcaneus and talus). In the hindfoot, the calcaneus ossifies first. Periosteal bone formation occurs on the inferolateral aspect of the calcaneus in a 93-mm fetus [21]. The endochondral center of ossification appears at 125mm [22]. Both talus and calcaneus are primarily cartilaginous at birth and have small ossific nuclei [23-29]. The talus may begin to ossify in the eight lunar month, but an ossification center is not always present at birth [22]. The cuboid is the last tarsal element that exhibits prenatal ossification; it develops an ossific nucleus just before or after birth. The navicular remains entirely cartilaginous for one or two years [1, 30-32]. At age 1 year in girls and 1.5 years in boys, the foot has achieved half the adult dimension. The skeletal development changes initiated during the fetal period continue until adulthood.

1.1 Clubfoot Deformity and Ponseti Technique

Clubfoot or talipes equinovarus, a complex foot deformity readily apparent at birth, may be classified into four types: teratologic, syndromic, positional and congenital. The origin of congenital clubfoot in otherwise normal patients has remained unknown. Etiological theories include intrauterine molding defect, blastemic defect of the tarsal cartilage, primary nerve lesion with secondary muscle dysfunction, vascular abnormalities, arrested embryonic development, abnormal tendon insertions, and primary fibrotic contracture. The most widely accepted is that of polygenic inheritance modified by environmental

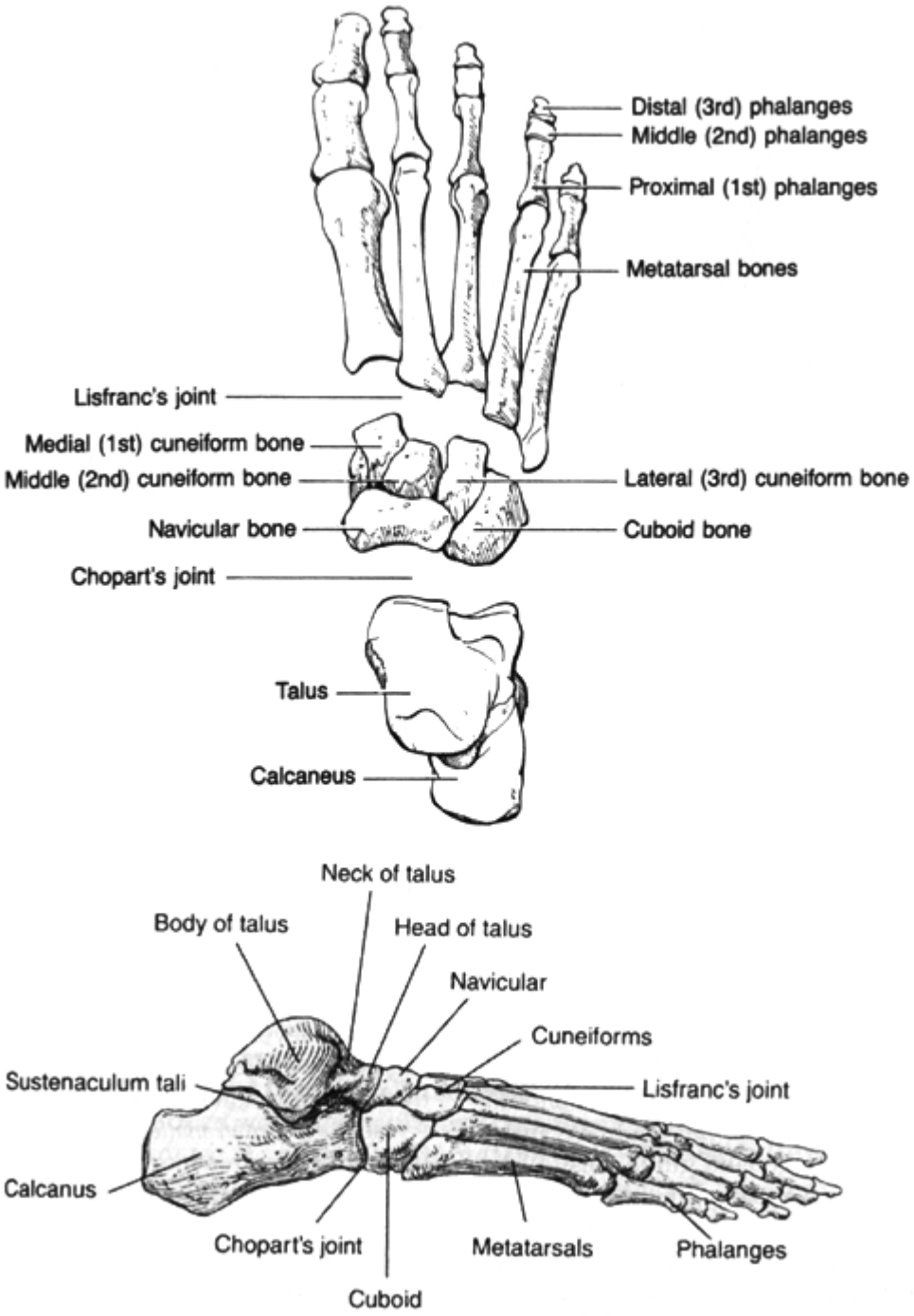

Figure 1.2. Bones of the foot: Axial view (top) showing the forefoot at the top, mid-foot in the middle, and hind-foot in the bottom; Lateral view (bottom) displaying the same from right to left (From Handbook of orthopaedic emergencies. Philadelphia: Lippincott Raven, 1999 [33]).

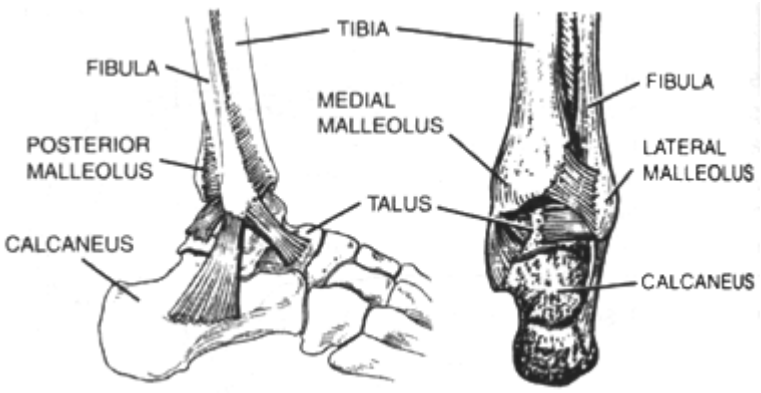

Figure 1.3. The ankle (From Handbook of orthopaedic emergencies. Philadelphia: Lippincott Raven, 1999 [33]).

Factors [1]. Congenital clubfoot occurs in up to 1 in 1000 live births and is the most common type of clubfoot. It has a male predominance of 2:1 and an incidence of bilaterality of about 50% [1]. A primary deformity of the talus is believed to be the basis of congenital clubfoot. Talar abnormalities have been found in all categories of clubfoot, raising the question as to whether they are primary or secondary [34].

The ossification of short or irregular bones such as talus mainly proceeds as endochondral ossification, but it has been shown by some investigators that periosteal bone formation is also present in the normal talus and calcaneus [21, 35-37], and the existence of cortical bone has been pointed out for the clubfoot talus [34]. The ossification center of the normal talus normally forms near the geometric center of the talus, whereas in clubfoot it is situated eccentrically in the neck which includes the non-articulating surfaces of the talus, and more laterally than that of the normal talus. Periosteal bone joins the endochondral ossification center below (surfaces of the sinus and canalis tarsi), and in well-differentiated specimens also above (tibiotalar joint) [36].

The normal ossification of calcaneus occurs in a precise sequence of perichondral and endochondral ossification [37]. Within the clubfoot calcaneus, the coordination of perichondral and endochondral ossification is disturbed, ossification grooves and associated cartilage canals are not found in regular positions, and the process of endochondral ossification is disrupted [37]. The ossific nuclei in the calcaneus and talus are smaller in clubfoot than normal [24], and the appearance of an ossific nucleus in the cuboid and navicular is delayed [38].

All clubfeet are not of the same severity, although all have the basic components of adduction and inversion of the forefoot and midfoot, heel varus, and fixed equinus (see Appendix A and Figure 1.4). The primary abnormality in clubfoot has been described as deformity of the anterior part of the talus, with the head and neck being shortened and angulated medially and plantarly [29, 39-40]. Other major deformities include talonavicular misalignment and medial shift of the navicular. The navicular articulates with the medial aspect of the talar neck, and is wedge-shaped laterally, with a prominent tuberosity. The calcaneus is small, often with an absent anterior facet. The calcaneus is also medially shifted beneath the talar head and rotated to a considerable degree. Calcaneus and talus display parallelism on both the AP (anteroposterior) and lateral radiographs indicating hindfoot varus and equinus. In unilateral deformities, the foot is smaller on the noninvolved side.

Clubfoot deformity, regardless of origin, often results in a severe handicap unless corrected. The primary treatment for clubfoot has consisted initially of manipulation and bandaging or splinting [41-43]. With the advent of simple surgery (Achilles tenotomy

[44-45]) in the mid 19th century, and then the possibility of more complex surgery (hind-foot osteotomies, ligament releases[42-43]) as a result of anesthesia and antiseptic surgery in the late 19th century, surgery became more popular as a result of unsuccessful non-operative treatment. Kite, seeing many patients with neglected clubfoot, advocated in the late 1930s repeated gentle manipulations without anesthesia and stressed the importance of sequentially correcting the adduction, varus, and equinus rather than correcting them together [46]. While the point is difficult to document in the literature, Mosca suggests many could not replicate the results reported by Kite and others [18]. McKay [47] for example, suggested the rate of correction by casting is only 5%, but most authors report substantially higher numbers, up to 84-90% [48-49]. Failure to achieve correction perhaps explains the seeming late 20th century popularity of surgery for clubfoot even in infants, and was likely related to two major factors: 1) initiation of treatment too late to influence the adaptation of the cartilage anlage, 2) inappropriate application of manipulation and splinting or casting.

Ponseti [29, 40] in the late 1940s and 1950s, recognizing the failures of surgery, and manipulation and casting, developed an approach to manipulation and corrective casting which many authors have found successful [50-55]. He emphasized four deformities: varus, adductus, cavus, and equinus. In contrast to Kite's suggestion of sequential correction, he proposed correcting the first three together with the rationale that the motions of the hind-foot anlagen are linked and cannot be separated as Kite had suggested, and claimed that attempting to do so would effectively block correction and induce deformity. On the other hand Ponseti argued that after the first three were

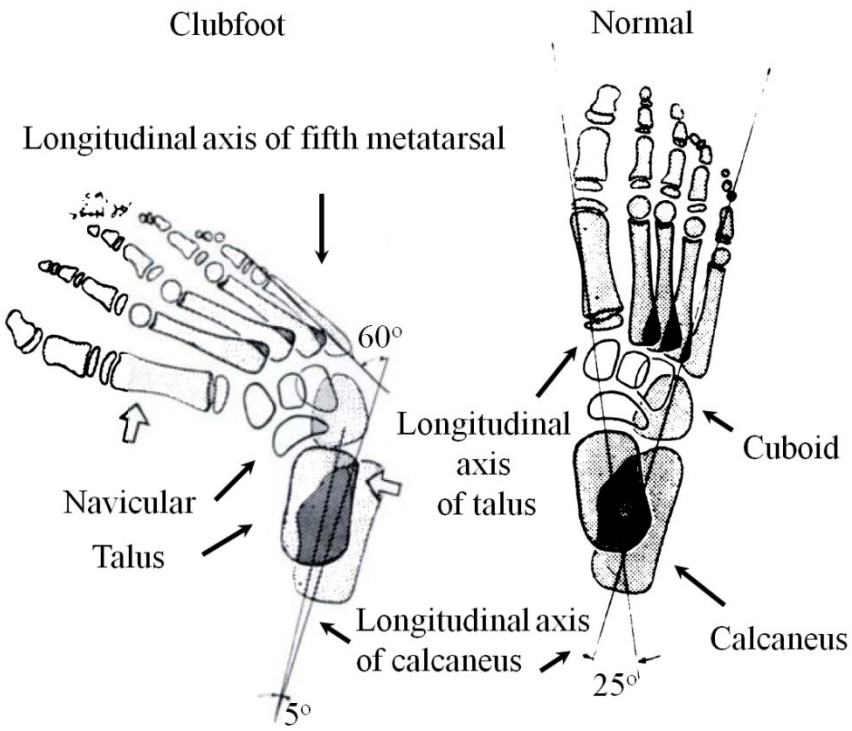

Figure 1.4. Ponseti's classic diagrammatic figure clarifying the relationships among the bones on the anteroposterior view of a normal foot (left), a foot with metatarsus adductus (middle), and a clubfoot (right). Hollow arrows indicate the sites and directions of molding during corrective cast manipulation and plaster cast application (Source: I. V. Ponseti; JBJS 1966; 48(4):702-11 [56]).

corrected, equinus (which is not kinematically linked to the other three but relates primarily to a tight heel cord) could be independently corrected (Figures 1.5, 1.6).

Despite the numerous studies describing the deformities and making comparisons between the normal and clubfeet, there is little information on the presumed mechanism by which serial casting corrects these deformities and induces shape changes. The most common view [17-19] suggests that the casting loads produce stretching of tight ligaments, capsule and tendons which then somehow restore more normal boney

architecture. No evidence is available to support this view and no mention is made of the anlagen and their abnormal shape or if and how these shapes are corrected.

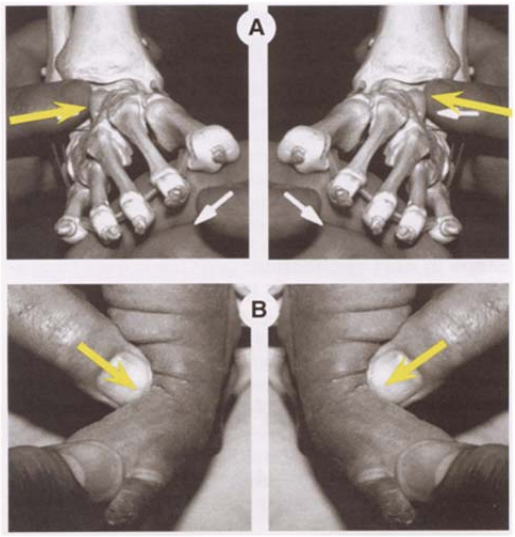

Figure 1.5. Ponseti treatment: (A) Stabilizing the talus by placing the thumb over its head provides a pivot point around which the foot is abducted. The index finger of the same hand is place behind the lateral malleolus to further stabilize the ankle joint, (B) Abduction of the foot. The lateral motion of the navicular and of the anterior part of the calcaneus increases as the clubfoot deformity corrects (From Clubfoot: Ponseti Management; Global-HELP Publications).

Figure 1.6. Ponseti cast sequence. The first cast shows the correction of the *cavus* and *adductus* while the foot remains in marked *equinus*. Casts 2 through 4 show correction of *adductus* and *varus*. The *equinus* deformity gradually improves with correction of adductus and varus (because the calcaneus dorsiflexes as it abducts under the talus). Full correction of equinus requires a heel cord tenotomy (From Clubfoot: Ponseti Management; Global-HELP Publications).

CHAPTER 2. MECHANICAL REGULATION OF GROWTH, OSSIFICATION, AND ADAPTATION

2.1 Experimental Evidence

Mechanical stimulation experimentally influences skeletal cell metabolism. Mechanotransduction, or the conversion of a biophysical force into a cellular response, is an essential mechanism for a wide variety of physiologic functions which allow living organisms to respond to the mechanical environment [57].

Endochondral ossification is an important process in osteogenesis, structural growth, and fracture healing which follows a sequence of events involving the proliferation of chondrocytes, chondrocyte hypertrophy, matrix mineralization, resorption of mineralized matrix by osteoclasts, and finally deposition of bone by osteoblasts (may remove). Many *in vitro* studies have shown that mechanical stimulation influences chondrocytes metabolism [58-70]. Wright et al. [71] reported chondrocytes responded to strains as low as 15 microstrain. In a study by Tanck and coworkers [72], it was found that the largest strains occurred where hypertrophied chondrocytes were present, and concluded it is likely that strain influences mineralization process. *In vitro* organ culture models of fetal murine metatarsal bones have been used to determine the effects of different biophysical stimuli on the process of endochondral ossification [73-75], where hydrostatic compression was found to stimulate chondrocyte hypertrophy and the extracellular matrix mineralization. Burger et al. [73] tested effect of intermittent compressive force (ICF) and continuous compressive force (CCF) on ossifying long bones and calvarial rudiments, and reported that ICF did not accelerate the onset of cartilage hypertrophy, but once a hypertrophic zone had developed, ICF accelerated

mineralization in this zone. In these studies the effect of hydrostatic stress was ascribed to development of shear stresses at the interface of mineralized and non-mineralized tissue. In an investigation of influence of ICF and CCF on calcification of growth plate cartilage, Klein-Nulend and colleagues [76] reported that hypertrophic chondrocytes responded directly to ICF and CCF by an increased deposition of calcium-phosphate mineral in the matrix, and that discontinuous mechanical stimulation evoked a higher cellular response than did continuous stimulation.

Mechanical loading of bone not only deforms the bone tissue, but also causes movement of extracellular fluid through the bone's lacuno-canalicular system. Such fluid flow may stimulate bone cells via wall shear stress, streaming potentials, or chemo-transport related effects [77-79]. It is hypothesized that the osteocytes and bone lining cells detect mechanical signals and communicate those signals to the bone surface. Soluble mediators which include prostaglandins (PGs) and nitric oxide (NO) are released and cause the recruitment and/or differentiation of osteoblasts from proliferating and nonproliferating osteoprogenitor cells [80]. Explants cannot be used for experiments of longer than 24 hours duration, so many investigators have used bone cells in primary cultures or cell lines [81]. Glucksmann [82] pioneered studies on mechanotransduction using biologic materials to apply loads to bone cell cultures. More recently, hydrostatic compression, longitudinal and axisymmetric substrate distension, substrate bending, fluid shear, and combinations of these models have been developed to mimic the physiological components of the mechanical stimuli presumed to occur in vivo. These methodologies have been reviewed by Brown [83]. The response of bone cells to the varied mechanical stimuli has provided some insight into the relative importance of each type of stimulus to

the ultimate generation of an adaptive response [81]. There is growing body of evidence that fluid flow within the canaliculi and lacunae of bone is primarily responsible for mechano-chemical signal transduction in bone cells [80]. The dominant determinant of the bone cell's response to this fluid flow is hypothesized to be due to fluid shear stresses that stimulate cell wall processes [84-87], causing cell deformation and subsequent metabolic activity via integrins and the cytoskeleton [81], however, it is more than probable that bone cells respond to more than one component of their mechanical environment. This is suggested strongly by the ability of mechanical strain as well as fluid flow stimuli to promote bone cell activity [84, 88-89]. Since in vivo loading is always accompanied by fluid flow, bone cells may respond to changes in their strain environment via an integrated assessment of changes in multiple parameters associated with both fluid flow and physical deformation [81].

2.2 Theoretical Modeling

Growth and remodeling are fundamental processes in the development of tissues. This field has been an important research topic in biomechanics over the recent decades (Refer to articles by Humphrey [90] and Taber [91] for numerous related references). The description of the biological process of growth and remodeling is of interest both because of its importance as a fundamental mechanical process that occurs in normal development and in a number of pathological conditions, and because it offers an interesting and unusual application of continuum mechanics.

A number of earlier authors constructed kinematical descriptions of growth using the methods of continuum mechanics, but the work of Hsu [92], Cowin and Hegedus

[93], Skalak [94], and Skalak et al. [95] are the initial efforts made to formulate mechanical theories to describe the growth of biological tissues. Growth is the process of gradual increase of net volume of a tissue, but it may also include some resorption. A distinction is made between growth on the surface (appositional) and within the substance (interstitial) of the tissue. Hard tissues such as bone and teeth grow by apposition, and soft tissues grow interstitially [96].

During the past quarter century, mechanical theories of growth have been formulated beginning with a study of uniform growth by Hsu [92], and the *theory of adaptive elasticity* proposed by Cowin and Hegedus [93], whereby they proposed general forms for stress-growth constitutive relations. These initial theories laid down the foundation for later work. Skalak [94-95] formalized the general kinematic descriptions of finite volumetric and surface growth. Fung [97-98] postulated a relatively simple relation between stress and growth rate. Later, combining and extending ideas of Fung, Skalak and coworkers, Rodriguez et al. [99] formulated a continuum theory that accounts for the coupling between stress and finite growth. This work characterizes the change in tissue mass through a multiplicative decomposition of the deformation gradient into a growth part and an elastic part, as first introduced in the context of plasticity by Lee [100]. In this approach mass changes are attributed to change in volume while the density remains constant.

Volumetric growth, from a mechanics perspective, is analogous to thermal expansion as pointed out by Skalak [94]. In linear elastic problems, growth (and thermal) stresses can be superposed on the mechanical stress field, but in nonlinear problems

another approach must be used. The fundamental idea is to refer the strain measures in the constitutive equations of each material element to its *current* zero-stress configuration, which changes as the element grows. This approach has been classically applied to model soft tissues undergoing large deformations, e.g. the arterial wall.

In bones, all growth can be classified as *surface growth* [91]. Bone grows primarily by accretion or resorption at a surface. Even internal growth is due to deposition on surfaces, such as the surfaces of the trabeculae or the walls of canals excavated by osteoclasts. Bone growth has received less attention than bone remodeling for a couple of reasons: (1) As Wolff [101] stated, modification of external form of the bone is often secondary to internal remodeling. (2) Moving boundary-value problems are often more difficult to solve than those with fixed boundaries. A variation of the adaptive elasticity theory is the surface growth theory of Cowin and Van Buskirk [102], which uses some average strain as the remodeling stimulus. It has formed the basis of several computational models. For example, Hart [103] developed a three-dimensional finite-element model that accounts for growth as in [102] and also includes internal remodeling by using a rate of change in solid volume fraction as developed by [93].

Remodeling involves changes in the internal architecture, apparent density, and (or) material properties while the overall volume remains unaffected. Although in principal applicable for small and large strain, this approach is typically adopted for hard tissues, e.g. bone, which usually undergo small strain deformations. Theories for bone remodeling have been proposed primarily by two groups of investigators. As mentioned earlier, Cowin and coworkers developed a continuum-mechanics-based formulation

which they call the adaptive elasticity theory. Cowin originally developed a form of this theory for cancellous bone [104-106], and Torezen and Skalak [107] extended it to soft tissues. In their theory apparent density and trabecular architecture are generally treated separately. The other approach which accounts for both simultaneously was developed by Carter and colleagues. This theory uses an average measure of the entire stress history for the remodeling stimulus. Variations of this theory have been used to study bone development including ossification, adaptation, and fracture healing [108-109].

For creating phenomenological models for tissue growth and adaptation, a parameter must be selected to represent the effect of mechanical loading on the development of the tissue. Biomechanical models have examined various mechanical quantities such as stress, strain or strain energy in the tissue as possible modulators of growth and remodeling. It is not clear however which mechanical quantity better explains these phenomena. Experimental data can be found in support of each. Furthermore, the driving-mechanism may be tissue-dependent and therefore, a universal law may not exist [91, 99]. Cowin [110] argued that strain is the most likely candidate since it is a primary, directly measurable, physical quantity that can be measured by stretch-activated receptors, whereas stress is an abstract concept that can be measured only indirectly. On the other hand, strain depends on the choice of a reference configuration, which may not be well-defined especially in soft tissues which undergo large deformations. The loading *rate* of deformation has been suggested as a stimulus since shear stress caused by fluid flow over the endothelial and bone cells is a stimulus for their activity, and shear stress is proportional to the rate of deformation of the fluid. Furthermore, the loading rate of deformation is an instantaneous kinematic measure independent of the reference

configuration and therefore, does not have the disadvantage of excluding strain as a growth stimulus [96]. Carter et al. [111] favor strain energy or an effective cyclic stress. They hypothesize heat energy generated during cyclic loading may trigger chemical reactions. Moreover, they showed for small strains that stress, strain, and strain-energy criteria all have similar mathematical forms. Carter and coworkers argue that hydrostatic pressure inhibits cartilage growth and ossification, while octahedral shear stress accelerates ossifications.

CHAPTER 3. STRUCTURE AND COMPOSITION OF CARTILAGE AND BONE

The musculoskeletal system consists of skeletal connective tissues (bone, cartilage, and dense fibrous tissues) and muscle that make possible movement. A tissue is a collection of cells, and extracellular matrix specialized to perform specific functions. The extracellular matrix (ECM) is an active scaffold that endows the tissue with its strength and resilience and regulates cell shape, orientation, movement, and overall function. The matrices of the musculoskeletal tissues consist of highly organized frameworks of organic macromolecules with water. These matrices are in the form of fibrils of multiple types of proteins (e.g. elastin, collagen, fibronectin), embedded in a ground substance consisting primarily of water and proteoglycans. The matrix contains another class of macromolecules called noncollagenous proteins. Each tissue has a unique combination of these classes of macromolecules. In addition to an organic matrix, bone has an inorganic matrix which consists primarily of calcium phosphate. The differences in the matrix composition and structure give the skeletal connective tissues different mechanical properties. Hyaline cartilage has the ability to resist compression, distribute loads and provide low friction surfaces in joints. The dense fibrous tissues (e.g. tendons and ligaments) have tensile strength and flexibility, and bone has strength and stiffness for providing a rigid support for normal function of other tissues. Collagens give the connective tissues their basic form and tensile strength. Tissues vary in collagen concentration and organization, and in their types of collagen. All collagens function as structural proteins in the matrix with a significant portion of each collagen molecule consisting of a triple helix formed from three amino acid chains. Differences in molecular

topology and polymeric form divide the known collagen types into three classes: fibrillar collagens (class I), basement membrane collagens (class II), and short chain collagens (class III).

Class I collagens – Five collagen types are in this group: types I, II, III, V, and IX. Type I collagen forms Collagen type I forms the main matrix macromolecule of skin, bone, meniscus, annulus fibrosis, tendon, ligament, joint capsule, and all other dense fibrous tissues. Type II collagen forms the fibrils found in hyaline cartilage, the nucleus pulposus, and the vitreous humor of the eye. The "minor" fibrillar collagen types, V and XI, also are present in the matrices of connective tissues. Type V forms part of the matrix in tissues containing type I (~3% of type I amount), and type XI forms part of the type II collagen fibrils. Type III collagen is found in association with type I in most tissues other than bone. This type of collagen also appears in repair tissue.

Class II collagens - These include types IV, VII, and VIII, which form critical parts of basement membranes.

Class III collagens – This class include collagen types VI, IX, and X with less understood form and function than the other types. Collagen type VI appears in small quantities in many tissues. Type IX forms covalent bonds with collagen type II molecules and thus contributes to the matrix of hyaline cartilage. Type X occurs in calcified cartilage, articular cartilage, and one fracture callus.

Proteoglycans (PG) are the major nonfibrillar macromolecule of cartilage, intervertebral disc, dense fibrous tissue, bone, and muscle tissue. The highest PG concentration occurs in hyaline cartilage and nucleus pulposus. The dry weight

concentration may reach up 30-40% in these tissues. In fibrous tissues and bone, they contribute at most a few percent of the dry weight.

PG molecules are the basic units of PG aggrecan. Aggrecan consists of protein core filaments with covalently bound side chains. Connective tissue glycosaminoglycans include hyaluronic acid, chondroitin 4 sulfate, chondroitin 6 sulfate, dermatan sulfate, and keratin sulfate. They are negatively charged and bind water and cation in the solution. Aggrecans can expand because of this property. An intact collagen fibril network limits the swelling (Figure 3.1).

3.1 Cartilage

Cartilage consists of cells embedded within an abundant extracellular matrix. The cells make up 5% of the tissue volume and the matrix contributes about 95%. Tissue fluid forms the largest component of cartilage. Depending on its type and age, water contributes 60 to 80% of the wet weight of cartilage. The structural macromolecules form 20 to 40% of the wet weight, and include collagens, proteoglycans, and noncollagenous proteins (Figure 3.2). Differences in matrix composition, mechanical properties, and microscopic and gross appearance differentiate three types of adult human cartilage: hyaline, fibrous and elastic cartilage. Hyaline cartilage, the most abundant form of cartilage, forms most of the skeleton before it is removed and replaced in the process of endochondral ossification. It also forms the physeal cartilage that produces longitudinal

bone growth before the skeletal growth ceases. It persists in adults in several forms including articular cartilage and nasal cartilage.

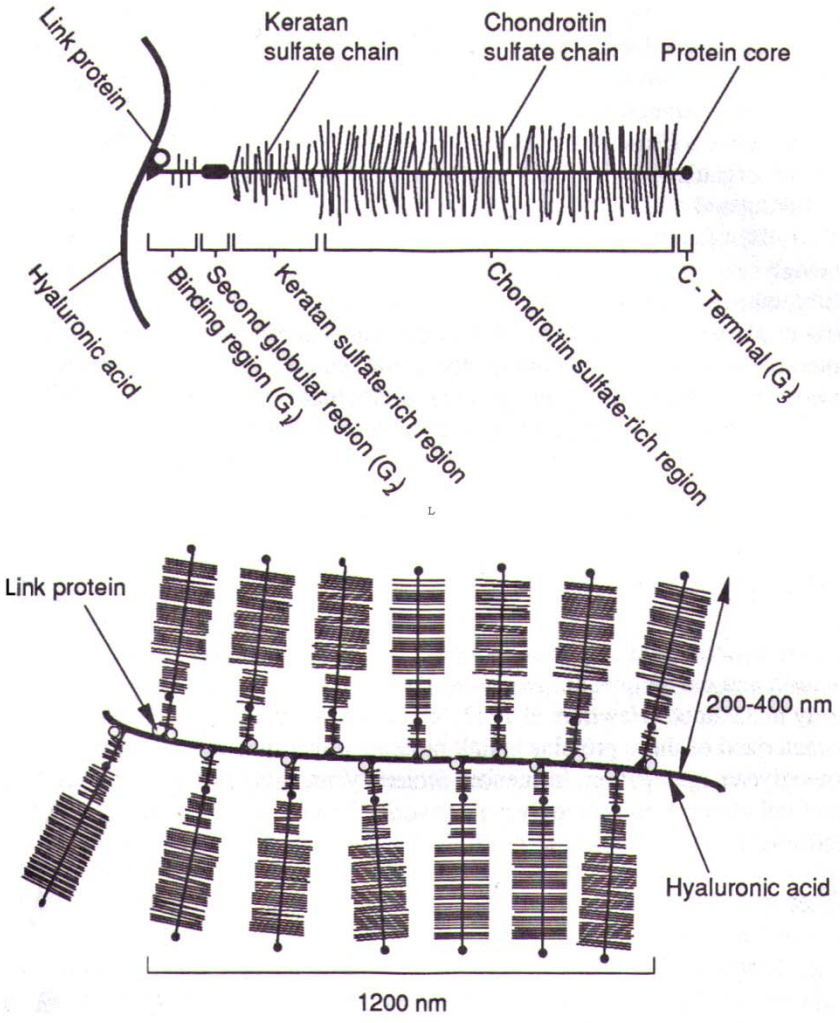

Figure 3.1. Schematic representation of an aggregating proteoglycan monomer (From V. C. Mow et al., Biomechanics of diarthrodial joints, Vol. I; 1990 [112]).

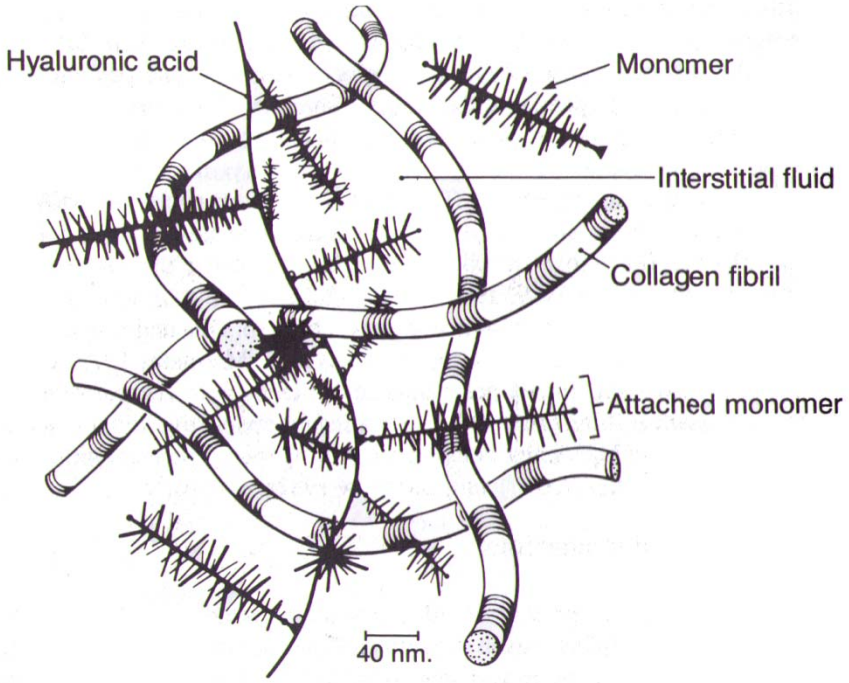

Figure 3.2. Schematic representation of cartilage molecular organization. Collagen and proteoglycan interact to form a porous solid matrix that is swollen with water (From V. C. Mow et al., Biomechanics of diarthrodial joints, Vol. I; 1990 [112]).

Hyaline cartilage does not contain elastin. In most hyaline cartilages, collagens contribute about 50% of the tissue dry weight, proteoglycans about 30-35%, and noncollagenous proteins about 15-20%. Type II collagen fibrils form the cross-banded fibrils accounting for 90-95% of total hyaline cartilage collagen. Hyaline cartilage contains at least two other types of collagen, types IX and XI, and may contain trace amounts of other types. Type X collagen is also present in the mineralizing regions of articular cartilage and growth plate cartilage.

Hyaline cartilage has a high concentration of large aggregating proteoglycans that give the tissue its unique material properties in compression. It also contains smaller nonaggregating proteoglycans like those found in dense fibrous tissues. The large aggregates help control fluid flow in the tissue. Noncollagenous proteins also have an important role in hyaline cartilage, such as increasing the size of PG aggregates, and establishing and maintaining the relationships between the chondrocytes and the matrix macromolecules.

Two important forms of hyaline cartilage, namely articular cartilage and growth cartilage are discussed below.

Articular Cartilage

Articular cartilage is located at the end of articulating bones and provides for a lubricated load bearing and low-friction surface with remarkable durability. It minimizes the stress on subchondral bone by distributing loads. Though at most only a few millimeters thick, it has a highly organized architecture. It can be divided into four zones: the superficial zone, the intermediate (middle or transitional) zone, the deep or radial zone, and the calcified cartilage zones. The matrix composition, water content, collagen fibril orientation, cell alignment and morphology vary across zones.

Growth Cartilage

Bones elongate by growth of the cartilage in the growth plates. The growth cartilage increases its volume by synthesis of new matrix and cell swelling. It has a zonal

organization that differs considerably from that of articular cartilage. The growth plate layers consist of resting or reserve zone, proliferative zone, and hypertrophic or maturing zone. The cells in the resting zone show relatively little evidence of metabolic activity. In the proliferative zone, the chondrocytes divide rapidly and synthesize a new matrix. The cells in this zone assume a highly oriented flattened shape. Toward the bottom of this zone, the proliferative cells begin to enlarge creating the hypertrophic zone. In the last part of the hypertrophic zone is the zone of provisional calcification.

3.2 Bone

Bone matrix consists of mesenchymal cells (undifferentiated or osteoprogenitor cells, osteoblasts, osteocytes, and osteoclasts) and an extracellular matrix. The matrix consists of organic macromolecules, inorganic mineral, and the matrix fluid. The inorganic component contributes about 70-80% of the wet weight of the bone. The organic macromolecules constitute about 20% of the wet weight, and the water about 8-10%. The organic component gives the bones its form and tensile strength, and the mineral component provides it with compressive strength. Type I collagen constitutes over 90% of the organic matrix.

Bones span a variety of shapes and sizes. On the microscale, the osseous tissue has two forms: the cortical or compact bone, and the cancellous, trabecular or spongy bone. As appears form its name, cancellous bone has a spongy form, thus has a higher surface area but is less dense, softer, weaker, and less stiff than the cortical bone. It typically occurs at the ends of long bones, proximal to joints and within the interior of vertebrae. The porosity of the trabecular bone may range from approximately 0.30 to

more than 0.9 [113], where the pores are filled with marrow. On the contrary, the compact (cortical) bone has very low porosity of approximately 0.05 to 0.3 [113]. The pores in the cortical bone consist of Haversian canals which contain capillaries and nerves, the Volkmann's canals which are connections between the Haversian canals, and the resorption cavities which are temporary spaces in remodeling. Cortical bone forms about 80% of the skeleton and as its name implies, it surrounds the thin bars or plates of cancellous bone with compact lamellae.

On the macroscale, bones are classified into three groups based on their shape: long, short, and flat bones. Examples of long bones are the tibia, femur, and humerus that have an expanded metaphysic and epiphysis at either end with a thick walled tubular diaphysis made of cortical bone that surrounds a marrow cavity containing little or no trabecular bone. The metacarpals, metatarsals, and phalanges have the form of long bones. Short bones, like tarsals and carpals, have approximately the same length in all directions. They usually have thinner cortices than the diaphyses of long bones and contain cancellous bone. In flat bones, like the scapula, there is one dimension that is much shorter than the other two.

CHAPTER 4. BIPHASIC MODELS OF MECHANICAL BEHAVIOR OF SOFT TISSUE

4.1 Review

Various models have been used to describe the biomechanical behavior of soft connective tissue under uniaxial compressive loading, including elastic [114], biphasic [4], triphasic [9], poroviscoelastic [115-116], fibril-reinforced [117-118], and transversely isotropic models [5, 119]. The biphasic theory developed by Mow et al. is one simple yet descriptive and widely used model which is well applicable to any biphasic tissue in the body (mature cartilage, meniscus, ligaments, etc.).

Tissues can be classified as mixture-composites, for they consist of multiple solid constituents, with bound and unbound water. It is therefore natural to apply the concept of mixtures to describe certain behaviors of soft tissues, particularly those due to significant exchanges of mass, momentum or energy between constituents. The continuum theory of mixtures in its modern form was presented by Truesdell in 1957 [120]. V. C. Mow and colleagues were the first to apply the continuum mixture theories for biological tissues, specifically articular cartilage [4]. The so-called biphasic theory is the most traditional model of cartilage that assumes cartilage as an isotropic homogeneous tissue composed of two intrinsically incompressible phases: an interstitial fluid phase and an elastic solid phase.

In the classical biphasic theory [4] cartilage matrix was assumed linear elastic. To describe the nonlinear behaviors of cartilage in large deformations, a finite deformation biphasic theory was formulated by Mow and colleagues [16]. Later, Kwan and coworkers

[121] suggested a finite deformation constitutive law for the nonlinear response of the solid phase, which was refined later by Holmes [122] and then by Holmes and Mow [16]. These models assume the solid phase of the cartilage to be hyperelastic and isotropic.

Although successful in predicting the response of tissue in confined compression, the isotropic, homogeneous form of biphasic theory has had shortcomings in predicting viscoelastic behaviors of inhomogeneous and anisotropic materials such as articular cartilage in other testing geometries, e.g., unconfined compression and indentation experiments. Under the general framework of the biphasic theory many mechanical models employing higher levels of tissue material complexity have been proposed.

Effects of intrinsic viscoelastic behavior of the solid matrix were introduced into the framework of biphasic theory by Mak [123] based on the quasi-linear viscoelasticity model of Fung [124]. This addition improved the prediction of the model in unconfined compression as well as material parameter determinations. First attempts at describing the anisotropy of cartilage were made by Cohen et al. incorporating a transversely isotropic material tensor for the solid matrix [5], which improved the predictive power in unconfined compression capturing the high ratios of peak to equilibrium stresses in unconfined compression. However, Bursac et al. [125] showed the model was unable to simultaneously explain the high peak-equilibrium stress ratios in unconfined compression test and fit the radial stresses in a confined compression experiment.

More recent effort by Soulhat et al. [7] incorporated a fibrous microstructure into the linear elastic biphasic theory demonstrating better agreement between the theoretical predictions and experimental data from unconfined compression. The nonlinear tension-

compression property of the matrix was modeled by Soltz and Ateshian [8] based on the concept of conewise linear elasticity [126]. The model accurately predicted deformational behaviors and fluid pressure in confined compression [127]; however, it could not describe the viscoelastic response of cartilage under uniaxial tension well [128]. This suggests that the intrinsic viscoelastic (fluid-independent) property of the solid matrix reveals itself in tension. The biphasic-CLE-QLV model proposed by Huang et al. [128] combines the two previous extensions of the classical biphasic theory, namely the biphasic poroviscoelastic [123], and the biphasic conewise linear elastic [8] models. This theory was able to predict the tensile response of cartilage very well in addition to both confined and unconfined compression behaviors [128-129].

4.2 Formulation of the Biphasic Theory

The finite deformation biphasic theory is able to describe two different classes of nonlinear material behavior: those arising from strain-dependent permeability effects under infinitesimal strain conditions, and those associated with the finite deformation of the solid matrix.

The continuity equation for a biphasic medium with both phases intrinsically incompressible is given by

$$\nabla.(\phi^s \boldsymbol{v}^s + \phi^f \boldsymbol{v}^s) = 0 \tag{4.1}$$

where ϕ^s and ϕ^f are volume fractions for the solid and fluid respectively, $\boldsymbol{v}^s$ and $\boldsymbol{v}^f$ are velocity vectors of solid and fluid phases. Because the matrix is saturated the volume

fractions also satisfy: $\phi^s + \phi^f = 1$. For quasi-static situations, the equations of motion of the phases are:

$$\nabla . \boldsymbol{\sigma^s} + \boldsymbol{\pi} = \mathbf{0}, \quad \nabla . \boldsymbol{\sigma^f} - \boldsymbol{\pi} = \mathbf{0} \tag{4.2a,b}$$

where $\boldsymbol{\sigma^s}$, and $\boldsymbol{\sigma^f}$ are the stress tensors acting on the solid and fluid phases respectively, and π is the interaction force between the two phases, often called the momentum supply from one to the other. The momentum exchange is given by

$$\boldsymbol{\pi} = K(\boldsymbol{v}^f - \boldsymbol{v}^s) + p\nabla\phi^s \tag{4.3}$$

where K is the diffusive drag coefficient, which was shown by Lai and Mow [130] to be related to the permeability k through: $k = (\phi^f)^2/K$.

The Cauchy stresses are given by

$$\boldsymbol{\sigma^s} = -\phi^s p\boldsymbol{I} + \boldsymbol{\sigma^E} \tag{4.4a}$$

$$\boldsymbol{\sigma^f} = -\phi^f p\boldsymbol{I} \tag{4.4b}$$

$$\boldsymbol{\sigma^t} = \boldsymbol{\sigma^s} + \boldsymbol{\sigma^f} = -p\boldsymbol{I} + \boldsymbol{\sigma^E} \tag{4.4c}$$

where $\boldsymbol{\sigma^t}$ is the total stress, p is the fluid pressure, $\boldsymbol{I}$ is the identity tensor, and $\boldsymbol{\sigma^E}$ is the elastic component of the solid stress (effective solid stress tensor representing the portion of the solid stress in excess of the fluid pressure). The solid and fluid fractions are related to the tissue dilatation. The solid phase fraction for a general three-dimensional motion

has the form $\phi^s = \phi_0/\sqrt{I_3}$ where ϕ_0 is the initial solidity. It follows accordingly that $\phi^f = 1 - \phi_0/\sqrt{I_3}$.

Two constitutive laws are required to make the model complete: one for the strain energy function (to determine σ^E) , and one for permeability (to determine K) where both have to satisfy certain conditions detailed by Holmes and Mow [16]. For small strains Lai and Mow [130] found that the permeability is an exponential function of the infinitesimal strain. Based on that observation, Holmes and Mow [16] considered the following form for permeability in finite deformations:

$$k = k_0 \left[\frac{\phi_0 \phi^f}{(1-\phi_0)\phi^s}\right]^2 \exp\{M(I_3 - 1)/2\} \tag{4.5}$$

where k_0 is the permeability when the tissue is not loaded, k is a positive parameter that measures how fast the permeability approaches zero as a result of alterations in tissue porosity, and M is comes from the observation of exponential dependence of permeability on compressive strain.

For finite deformations, Holmes and Mow [16] suggested the following Helmholtz free energy function ψ^s for the solid phase:

$$\rho_0^s \psi^s = \alpha_0 \frac{e^{\alpha_1(I_1-3)+\alpha_2(I_2-3)}}{I_3^\beta} \tag{4.6}$$

where, to satisfy the Baker-Ericksen inequalities, α_0 must be positive, and α_1 and α_2 must be non-negative with at least one being non-zero. The stress is assumed to be zero at equilibrium, so $\beta = \alpha_1 + 2\alpha_2$.

For infinitesimal strains, the KLM (Kwan, Lai, and Mow) theory assumes the solid phase is a linearly elastic material, and the fluid phase is a Newtonian viscous fluid. Under these conditions, the stress-strain relationship becomes

$$\boldsymbol{\sigma^E} = \lambda_s tr(\boldsymbol{\epsilon})\boldsymbol{I} + 2\mu_s\boldsymbol{\epsilon} \tag{4.7}$$

where λ_s and μ_s are the Lame constants of the elastic solid matrix, namely the elastic bulk modulus and the elastic shear modulus respectively. The constants can be written as follows in terms of Young's modulus, E_s, and Poisson's ratio, ν_s:

$$\lambda_s = \frac{\nu_s E_s}{(1+\nu_s)(1-2\nu_s)} \tag{4.8a}$$

$$\mu_s = \frac{E_s}{2(1+\nu_s)} \tag{4.8b}$$

Reduction to the One-Dimensional Confined Compression Case

Let Z denote the material coordinate for the solid in the z direction, and $U(Z,t)$ be the axial deformation expressed in a material reference frame. In the one-dimensional ultra-filtration case (Figure 4.1), the invariants are related to stretch as follows: $I_1 = 2 + \lambda^2$, $I_2 = 1 + 2\lambda^2$, $\mathrm{I}_3 = \lambda^2$ where I_1, I_2, and I_3 are the three principal invariants of the Cauchy-Green deformation tensor for the solid phase, and the stretch in the z direction, λ, is given by $\lambda = 1 + \partial U/\partial Z$.

Since the theory assumes that the solid is hyperelastic, and because of the assumption of homogeneity and isotropy, ψ^s can be written in terms of the invariants of the strain tensor. The equation that relates ψ^s and the stress for such materials is [122]

$$\boldsymbol{\sigma^E} = 2\rho_0^s \lambda \left(\frac{\partial \psi^s}{\partial I_1} + 2\frac{\partial \psi^s}{\partial I_2} + \frac{\partial \psi^s}{\partial I_3} \right) \tag{4.9}$$

In the confined compression experiment, where a circular plug is compressed axially in a cylindrical chamber with impermeable frictionless walls and porous permeable loading platens, the principal stretches reduce to: $\lambda_1 = 1$, $\lambda_2 = 1$, $\lambda_3 = \lambda$ and using the Helmholtz energy function above (Equation 4.6), the axial stress-stretch law becomes:

$$\sigma^E = \frac{1}{2} H_{A0} \left(\frac{\lambda^2 - 1}{\lambda^{2\beta+1}} \right) e^{\beta(\lambda^2 - 1)} \tag{4.10}$$

H_{A0} represents the aggregate modulus and β is a non-dimensional compressive-stiffening coefficient describing the sensitivity of σ^E to large strains [16]. The governing equations of the finite deformation of the tissue are simplified as follows as shown by Holmes [122]:

$$\frac{\partial \boldsymbol{\sigma^E}}{\partial \lambda} \frac{\partial^2 U}{\partial Z^2} = \frac{\lambda}{k} \frac{\partial U}{\partial t} \qquad -\frac{h}{2} \leq Z \leq \frac{h}{2}, t \geq 0 \tag{4.11}$$

with the initial condition $U(Z, 0) = 0$. The boundary conditions are $U(h/2,0) = 0$, and $U(0, t) = U_0(t)/2$ for stress-relaxation, and $\sigma^E(0, t) = \sigma_0^E(t)$ for creep experiments

[131] where the latter two are the prescribed surface displacement and a prescribed surface stress. The system of partial differential equation (Equation 4.11) along with the boundary conditions completes the formulation. Finally, the permeability in Equation 4.5 takes the following form for one-dimensional compression:

$$k = k_0 \left[\frac{\phi_0 \phi^f}{(1-\phi_0)\phi^s} \right]^2 \exp\{M(\lambda^2 - 1)/2\} \tag{4.12}$$

The coefficient H_{A0} above is the finite strain analogue of the aggregate elastic modulus $H_A = \lambda_s + 2\mu_s$ and it has been shown [16] that the stress equation (Equation 4.10) reduces to $\sigma^E \cong H_{A0}\epsilon$ under infinitesimal strain conditions. Under small strains Equation 4.12 reduces to $k = k_0 \epsilon^M$ [130], where ϵ is the infinitesimal strain related to the stretch λ through: $\lambda = 1 + \epsilon$. Using this function for intrinsic permeability, the linear biphasic theory reduces to the so-called nonlinear diffusion equation for uniaxial confined compression tests in small strains [132]:

$$H_A \frac{\partial^2 U}{\partial Z^2} = \frac{1}{k_0} \exp\left(-M \frac{\partial U}{\partial Z}\right) \frac{\partial U}{\partial t} \tag{4.13}$$

It is of interest to point out that the biphasic theory and the poroelastic theory [133] have a slightly different approach, but are equivalent when the fluid phase is inviscid. The biphasic theory specifies the tissue as a continuum of solid and fluid phases, whereas the poroelastic theory describes a continuous distribution of pores in the solid matrix.

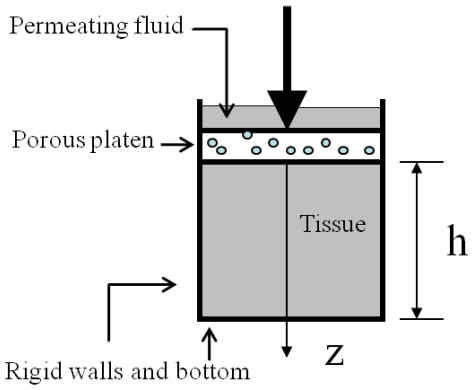

Figure 4.1. Schematic representation of one-dimensional ultra-filtration of cartilage.

CHAPTER 5. MATERIALS AND METHODS

5.1 Characterization of Talar Cartilage Anlage Mechanics

5.1.1 Experiments

Cartilage samples (n=16) were obtained from tali of two still-born fetuses in the third trimester (30 and 32 weeks of gestation). Seven were collected from the younger specimen and nine from the older. The fetal age was determined by measurement of crown-rump [134] lengths. The fetus legs were frozen when obtained and were kept frozen at -80^{o} C until the day of dissection. The feet were thawed and carefully dissected to separate the tali, which were partly ossified (Figures 5.1 and 5.2). The tissue was sagittally sliced (thickness = 1.5 mm) using a manual tissue chopper with a stage whose advancement was controlled by a micrometer. Due to the presence of both bone and cartilage within the tali, obtaining uniform slices was not possible using a cryostat or vibrating microtome. One to four cartilage plugs were gathered from each slice using a biopsy punch with a diameter of 3.00 mm. Plugs were taken from the unossified regions. The thickness of cartilage plugs was measured individually at the time of the experiment. The mean ± standard deviation plug thickness was 1.61 ± 0.37 mm. The samples were submerged in phosphate-buffered saline (PBS) and frozen at −80^{o} C until the day of testing.

On the day of testing, samples were thawed at room temperature and allowed 1.5 hours in PBS to equilibrate before the experiments. Each sample was first tested in confined compression, allowed to recover for 1.5 hours at room temperature, and finally tested in unconfined compression. The samples were submerged in normal saline solution

Figure 5.1. Dissected distal fibula and tibia, hind-foot bones (calcaneus and talus), and two mid-foot bones (navicular and cuboid).

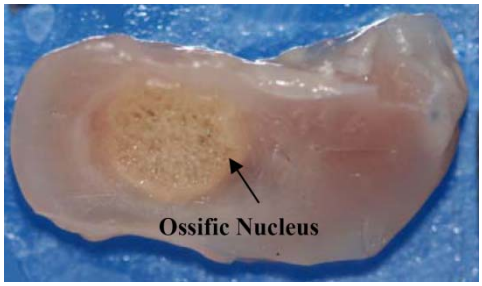

Figure 5.2. Sagittal slice of talus displaying the cartilaginous and ossified regions.

(0.15 mol/L NaCl) containing enzyme inhibitors (2 mmol/L EDTA, 5 mmol/L benzamadine, 10 mmol/L N-ethylmaleimide, 1 mmol/L phenylmethylsulfonyl fluoride) during testing and recovery time between tests. A custom-designed testing apparatus (displacement resolution, 5 μm; force resolution, 0.6 mN) with a smooth stainless steel chamber was used for both test configurations.

In the confined compression, the samples were placed inside a confining chamber with impervious walls and bottom (Figure 5.3) and loaded with a porous indenter (pore size, 50 μm; porosity, 40%). In the unconfined compression experiment, the samples were placed on an impervious surface using a flat solid indenter with a smoothly polished tip. In the latter configuration, all contact surfaces were lubricated with silicone grease to reduce friction.

Before collecting the data, a preconditioning load of 3.3 N (0.47 MPa) was applied to the samples for 60 seconds and then removed, followed by a tare load of 0.06 N (8.5 kPa) for 900 seconds. The thickness of each sample was measured after the tare load was applied right before each actual stress relaxation test. By taking readings from the load cell, the stepper motor revolutions which are convertible to length were counted from when the indenter touched the top surface of the plugs (when the force started to rise just above zero) until the prespecified tare load value was reached. This value was subtracted from the pre-tare-load thickness which was measured in the same manner, to get the post-taring thickness that was used for analysis. The prescribed displacement history consisted of four ramps of 5% strain each at a displacement rate of 1 μm/second, followed by a stress relaxation period of 500 seconds. The stress relaxation period was chosen such that the change in the stress value at the end of the period was smaller than 100 Pa/minute. The loading protocol was the same for both configurations.

Reproducibility of the measurements was examined for both biologic (bovine ankle articular cartilage) and nonbiologic (rubber) reference samples. Repeated testing on the same sample in both confined and unconfined compression produced material parameters that varied by less than 10%. Dry weight of the tissue was calculated using a lyophilizer.

Before deformation, photographs of the cartilage plugs were taken using a high-resolution camera (Canon EOS Rebel XTi; Canon USA, Inc, Lake Success, NY) with a macro lens, fixed on a stage. The diameters were calculated by fitting a circle to the sample's cross-section with a custom-written code using MATLAB (R2009a) image

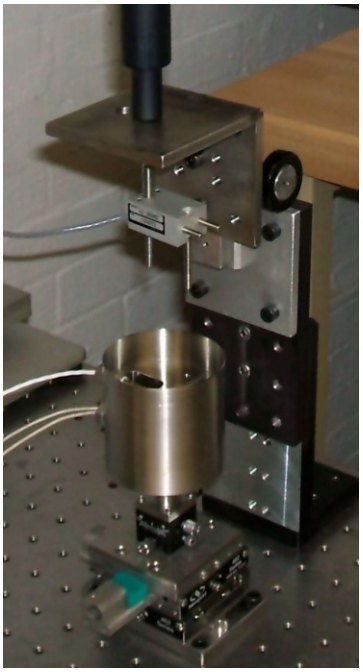

Figure 5.3. Experimental apparatus for confined and unconfined compression tests.

processing toolbox (The MathWorks Inc., Natick, MA). The average sample diameter was 3.29 ± 0.14 mm.

5.1.2 Parameter Extraction

The data of the confined compression experiments were analyzed by applying the finite deformation biphasic theory [16], as adapted and investigated in finite deformations by Ateshian et al. [131]. The compressive mechanical properties of talus anlagen were determined. The initial aggregate modulus H_{A0} and the related compressive-stiffening coefficient β were extracted by fitting the finite deformation constitutive equations to the equilibrium stress-stretch data (Equation 4.10, Figure 6.2). The permeability parameters

(k_o and M) were determined by using a custom-written code in MATLAB to find the best fit of Equations 4.11 and 4.12 to the transient stress-time data as obtained from the confined compression experiments (Figure 6.1). The Young's modulus of the solid matrix was found by fitting a line to the equilibrium stress-strain data of the unconfined compression experiment (Figure 6.3). The following formula was used to assess the goodness of fits:

$$r^2 = 1 - \frac{\sum(y - y_{est})^2}{(y - \bar{y})^2} \tag{5.1}$$

where y represents the experimental variable, y_{est} is the theoretical variable, and $\bar{y}$ is the mean value of y [135]. The Poisson's ratio was determined indirectly from solving the following equation for ν_s:

$$2H_{A0}{\nu_s}^2 + (H_{A0} - E_s)\nu_s - (H_{A0} - E_s) = 0 \tag{5.2}$$

5.2 Development of a User Material Subroutine

Soft hydrated tissues such as cartilage can be effectively modeled in commercial finite element software using their soil consolidation analysis [136-139]. Abaqus Unified FEA (SIMULIA, Providence, RI; formerly ABAQUS) has been used for this purpose extensively [140-143]. Throughout the text Abaqus is specifically referenced to, as our simulations were performed in that environment; however, the main focus remains general and can be implemented in any finite element program that allows user defined material behavior.

A hydrated porous medium is modeled in Abaqus as a multi-phase material where the total stress acting at a point in the medium is assumed to be made up of a macroscopic averaged pressure carried by the fluid (i.e. pore pressure) and an averaged effective stress carried by the solid matrix (i.e. effective stress). Using one specific case of the consolidation formulation in Abaqus in which the pores are saturated with only one fluid, i.e. the interstitial fluid, cartilage can effectively be modeled as a biphasic material. Mechanical properties of the solid matrix and the fluid must be provided to Abaqus. User defined material behavior can be defined in ABQUS through coding a user material subroutine (UMAT in Abaqus/Standard) by means of a programming interface (Fortran). The UMAT requires definition of the spatial tensor of elasticity and the Cauchy stress tensor. Assuming the tissue is isotropic hyperelastic, the strain energy function can be written in terms of the three principal invariants of its argument, and the stresses and elasticity tensors can be derived accordingly. The elastic Cauchy stress is obtained from

$$\boldsymbol{\sigma^E} = 2\rho_0 \left[\left(I_1 \frac{\partial \psi}{\partial I_2} + I_3 \frac{\partial \psi}{\partial I_3} \right) \mathbf{1} + \frac{\partial \psi}{\partial I_1} \boldsymbol{B} - I_3 \frac{\partial \psi}{\partial I_2} \boldsymbol{B}^{-1} \right] \tag{5.3}$$

where B is the left Cauchy-Green deformation tensor and ψ is the strain energy function (bold letters represent second order tensors when not shown in index notation). The choice of strain energy density function was the following as proposed by Holmes and Mow [16] for formulating the finite deformation biphasic theory,

$$\psi = \alpha_0 \frac{e^{\alpha_1(I_1-3)+\alpha_2(I_2-3)}}{I_3^{\beta}} \tag{5.4}$$

where I_1, I_2, and I_3 are the three invariants of the Cauchy-Green deformation tensor. The three parameters appearing in Equation 4.4 correspond to the mechanical properties of the tissue. Mechanical testing is typically performed with creep or stress relaxation using indentation *in situ* or on excised samples, or by tension, shear or compression of samples of cartilage. The material constants appearing in Equation 4.4 will now be derived in terms of the material properties obtained from confined and unconfined compression experiments: H_{A0}, β , and E (or ν_s) . For the confined compression experiment the principal stretches reduce to $\lambda_1 = 1, \lambda_2 = 1, \lambda_3 = \lambda$ and the stretch-strain law becomes [131] (see Chapter 3):

$$\sigma^E = \frac{1}{2} H_{A0} \left(\frac{\lambda^2 - 1}{\lambda^{2\beta+1}} \right) e^{\beta(\lambda^2-1)}$$

First, the stress is written in the form of Equation 3.10 to match the equation which was used in curve fitting to the confined compression experiment data. In the uni-axial compression configuration the three identities $I_1 = 2 + \lambda^2$, $I_2 = 1 + 2\lambda^2$, and $I_3 = \lambda^2$ hold, thus, using the strain energy function in Equation 4.4 the stress tensor is reduced to the following form

$$\sigma_E = 2\alpha_0(\alpha_1 + 2\alpha_2) \left(\frac{\lambda^2 - 1}{\lambda^{2(\alpha_1+2\alpha_2)+1}} \right) e^{(\lambda^2-1)(\alpha_1+2\alpha_2)} \tag{5.5}$$

By comparing Equations 3.10 and 4.5 it is concluded that

$$\alpha_1 + 2\alpha_2 = \beta \quad , \qquad \alpha_0 = \frac{H_{A0}}{4\beta} \tag{5.6a,b}$$

Equation 4.6a corresponds with the assumption of zero stress at equilibrium. To satisfy the Baker-Ericksen inequalities, α_0 must be positive, and α_1 and α_2 must be non-negative with at least one being non-zero [16] . Parameter α_0 is readily determined since H_{A0} and β are available from curve fitting to the confined compression experiment data. Parameters α_1 and α_2 cannot be extracted by solely using the properties obtained from the confined compression configuration, as they appear as a sum in Equation 4.5 which governs the stress-stretch relationship in the confined compression experiment. To obtain an additional equation for extracting α_1 and α_2 we simplify the constitutive equations to the case of infinitesimal strain ($\sigma^E = C_L\epsilon$) by linearizing the Cauchy stress tensor to obtain the relationships between the elasticity matrix (C_L) components in infinitesimal strain and the parameters of the strain energy function

$$\alpha_1 = \frac{C_{L2323}}{\alpha_0} - \beta, \qquad \alpha_2 = -\frac{C_{L2323}}{2\alpha_0} + \beta \tag{5.7a,b}$$

Noting that for a fully isotropic linear elastic material the following holds,

$$\begin{bmatrix}\sigma_{11}\\ \sigma_{22}\\ \sigma_{33}\\ \tau_{12}\\ \tau_{13}\\ \tau_{23}\end{bmatrix} = \begin{bmatrix} C_{L1111} & C_{L1122} & C_{L1122} & 0 & 0 & 0 \\ & C_{L1111} & C_{L1122} & 0 & 0 & 0 \\ & & C_{L1111} & 0 & 0 & 0 \\ & & & C_{L1212} & 0 & 0 \\ & symm. & & & C_{L1212} & 0 \\ & & & & & C_{L1212} \end{bmatrix} \begin{bmatrix}\epsilon_{11}\\ \epsilon_{22}\\ \epsilon_{33}\\ \gamma_{12}\\ \gamma_{13}\\ \gamma_{23}\end{bmatrix} \tag{5.8}$$

we can employ the identity $C_{L2323} = C_{L1212} = E/2(\nu_s + 1)$ to derive

$$\alpha_2 = \beta\left[1 - \frac{E}{(\nu_s + 1)H_{A0}}\right], \quad \alpha_2 = \beta\left[1 - \frac{E}{(\nu_s + 1)H_{A0}}\right] \tag{5.9a,b}$$

or in a more compact form, $\alpha_1 = (1 - 3\nu_s)\beta/(1 - \nu_s)$ and $\alpha_2 = \nu_s\beta/(1 - \nu_s)$. Equations 4.6b and 4.9 complete the formulation of the strain energy function for modeling of tissue's solid matrix. The stress values can now be evaluated using Equation 4.3. Additionally, input of the spatial tensor of elasticity is required. To construct a hyperelastic constitutive relationship using the Cauchy stresses, objectivity must be preserved. Cauchy stress is frame dependent but we may construct a constitutive relationship from an objective corotational rate of the Cauchy stresses. In Abaqus/Standard, the Jaumman rate of the Kirchoff stress $\boldsymbol{\tau} = J\boldsymbol{\sigma}$ is used for solid continuum elements [144]. This rate is defined as

$$\overset{o}{\tau}_{ij} = \frac{\partial \tau_{ij}}{\partial t} + \tau_{ik}\Omega_{kj} - \tau_{kj}\Omega_{ik} \tag{5.10}$$

where $\boldsymbol{\Omega} = asymm(\dot{\boldsymbol{F}} \cdot \boldsymbol{F}^{-1})$ is the spin tensor. Denoting $\mathbf{D} = symm(\dot{\boldsymbol{F}} \cdot \boldsymbol{F}^{-1})$ as the rate-of-deformation tensor, Equation 4.10 is recast as

$$\overset{o}{\tau}_{ij} = JC_{ijkl}D_{kl} \tag{5.11}$$

where C here is a modification of the 4*th* fourth order tensor of elastic moduli [145]. This tensor can be computed using a push forward operation of the 2*nd* fourth order tensor of elastic moduli C_E (blackboard letters represent fourth order tensors when not shown in index notation):

$$C_{ijkl} = F_{im}F_{jn}F_{kp}F_{lq}C_{Emnpq} + \frac{1}{2}\left(\tau_{ik}\delta_{jl} + \tau_{jk}\delta_{il} + \tau_{il}\delta_{jk} + \tau_{jl}\delta_{ik}\right) \tag{5.12}$$

where C_E is given by [146]

$$\mathbb{C}_E = 2\frac{\partial \boldsymbol{S}}{\partial \boldsymbol{C}} = 4\frac{\partial^2 \psi(I_1, I_2, I_3)}{\partial \boldsymbol{C}\partial \boldsymbol{C}} \tag{5.13}$$

$$= \delta_1 \boldsymbol{I} \otimes \boldsymbol{I} + \delta_2(\boldsymbol{I} \otimes \boldsymbol{C} + \boldsymbol{C} \otimes \boldsymbol{I}) + \delta_3(\boldsymbol{I} \otimes \boldsymbol{C}^{-1} + \boldsymbol{C}^{-1} \otimes \boldsymbol{I}) + \delta_4 \boldsymbol{C} \otimes \boldsymbol{C}$$

$$+\delta_5(\boldsymbol{C} \otimes \boldsymbol{C}^{-1} + \boldsymbol{C}^{-1} \otimes \boldsymbol{C}) + \delta_6 \boldsymbol{C}^{-1} \otimes \boldsymbol{C}^{-1} - \delta_7 \, \partial \boldsymbol{C}^{-1}/\partial \boldsymbol{C} + \delta_8$$

where the coefficients defined by

$$\delta_1 = 4\left(\frac{\partial^2 \psi}{\partial I_1 \partial I_1} + 2I_1 \frac{\partial^2 \psi}{\partial I_1 \partial I_2} + \frac{\partial \psi}{\partial I_2} + I_1^2 \frac{\partial^2 \psi}{\partial I_1 \partial I_2}\right)$$

$$\delta_2 = -4\left(\frac{\partial^2 \psi}{\partial I_1 \partial I_2} + I_1 \frac{\partial^2 \psi}{\partial I_2 \partial I_2}\right)$$

$$\delta_3 = 4\left(I_3 \frac{\partial^2 \psi}{\partial I_1 \partial I_3} + I_1 I_3 \frac{\partial^2 \psi}{\partial I_2 \partial I_3}\right)$$

$$\delta_4 = 4\frac{\partial^2 \psi}{\partial I_2 \partial I_2}$$

$$\delta_5 = -4\frac{\partial^2 \psi}{\partial I_2 \partial I_3}$$

$$\delta_6 = 4\left(I_3 \frac{\partial \psi}{\partial I_3} + I_3^2 \frac{\partial^2 \psi}{\partial I_3 \partial I_3}\right)$$

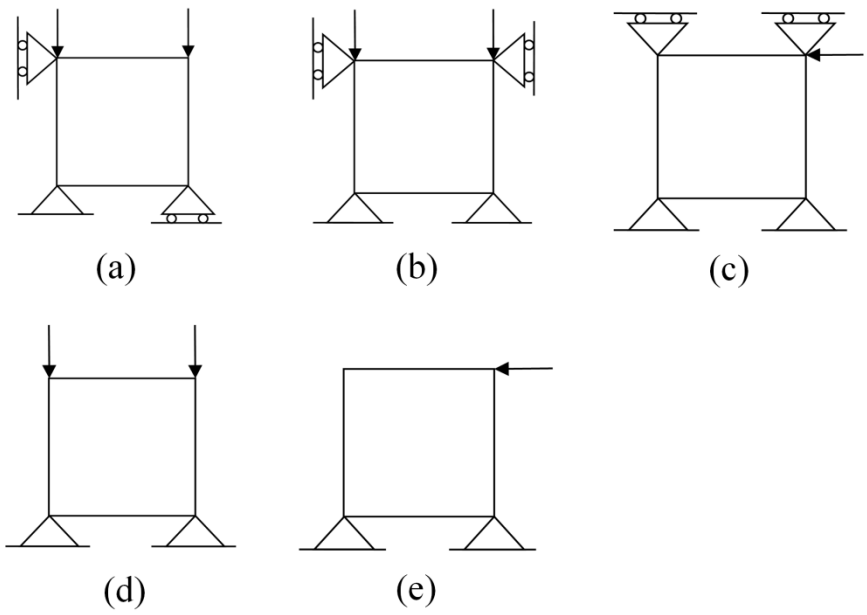

Figure 5.4. Test cases of hand calculations for linear elastic UMAT: (a) Free degrees of freedom: 3, 5, 6, 8; (b) Free degrees of freedom: 6, 8; (c) Free degrees of freedom: 5, 7; (d) Free degrees of freedom: 5, 6, 7, 8; (e) Free degrees of freedom: 5, 6, 7, 8.

$$\delta_7 = -4I_3 \frac{\partial \psi}{\partial I_3}$$

and $\otimes$ denotes the tensor product of two second order tensors creating a fourth order tensor ($\mathbb{D} = \boldsymbol{A} \otimes \boldsymbol{B}$ is $D_{ijkl} = A_{ij}B_{kl}$ in index notation). Tensor C (Equation 5.12) must be programmed into UMAT along with the Cauchy stress tensor. If the material model allows large volume changes and geometric nonlinearity is considered, the exact definition of the consistent Jacobian should be used to ensure rapid convergence [144].

To examine the UMAT formulation, two sets of tests were carried out. First, the general set-up of the user material subroutine was examined by comparing the results of

three different analyses for a linear elastic material in five test cases shown in Figure 5.4. The displacements, stresses and strains for a plane strain element (CPE4) were calculated for each test case using (1) FE analysis with the linear elastic model of Abaqus material library, (2) FE analysis using a linear elastic UMAT, (3) FE analysis using a linear elastic UHYPER, and (4) hand calculations using the isoparametric formulation of the 4-node quadrilateral element. For tasks 1, 2, and 3 the linear static analysis was used in Abaqus.

FE analysis using a linear elastic UMAT: For formulating the linear elastic material model in UMAT, the following strain energy function used [147]:

$$\psi = C_1 J_1^2 + C_2 J_2 \tag{5.14}$$

where $J_1 = (I_1 - 3)/2$, $J_2 = (I_2 - 2I_1 + 3)/4$, $C_1 = (\lambda + 2\mu)/2$, and $C_2 = -2\mu$. The following derivatives were programmed in the subroutine to formulate the Cauchy stress (Equation 5.3) and the Jacobian (Equations 5.12 and 5.13):

$$\frac{\partial \psi}{\partial I_1} = \frac{I_1}{2} C_1 - \frac{1}{2}(3C_1 + C_2)$$

$$\frac{\partial^2 \psi}{\partial I_1^2} = \frac{C_1}{2}$$

$$\frac{\partial \psi}{\partial I_2} = \frac{C_2}{4}$$

$$\frac{\partial^2 \psi}{\partial I_2^2} = \frac{\partial^2 \psi}{\partial I_3} = \frac{\partial^2 \psi}{\partial I_3^2} = 0$$

Hand calculations of the 4-node quadrilateral element: In an isoparametric formulation a parent element is defined in terms of a set of natural coordinates. The shape functions are

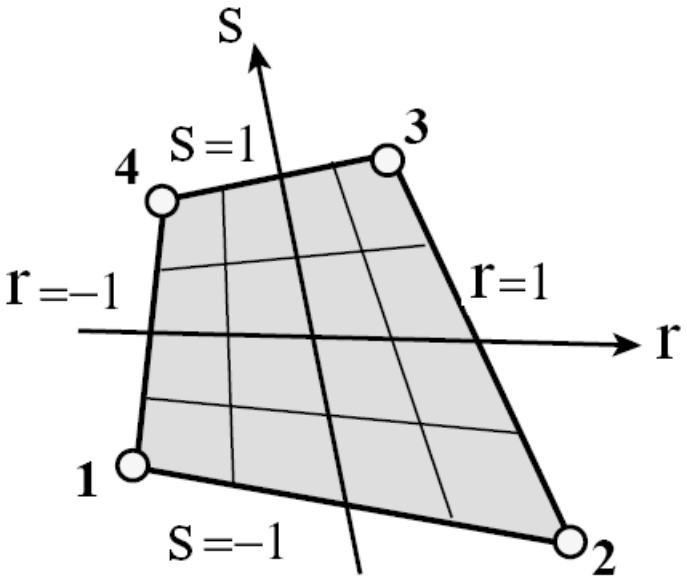

Figure 5.5. A 4-node bilinear quadrilateral element.

constructed on a parent element and used to compute the coordinates and displacements within each element using

$$x = \sum_{i}^{n} N_i x_i\,, \quad y = \sum_{i}^{n} N_i y_i$$
$$u = \sum_{i}^{n} N_i u_i\,, \quad v = \sum_{i}^{n} N_i u_i \tag{5.15}$$

where N_i are the shape functions, n is the number of nodes, x_i and y_i are the nodal coordinates, and u_i and v_i are the nodal displacements. For a quadrilateral element, r and s are the natural coordinates as shown in Figure 5.5. The simplest elements use linear

interpolation giving the following shape functions where the nodes are numbered as shown in Figure 5.5.

$$\begin{aligned} N_1 &= \frac{1}{4}(1-r)(1-s) \\ N_2 &= \frac{1}{4}(1+r)(1-s) \\ N_3 &= \frac{1}{4}(1+r)(1+s) \\ N_4 &= \frac{1}{4}(1-r)(1+s) \end{aligned} \tag{5.16}$$

The strains are then given by

$$\boldsymbol{\epsilon}^T = \left[\epsilon_{xx}, \epsilon_{yy}, \epsilon_{xy}\right] = [\frac{\partial u}{\partial x}, \frac{\partial y}{\partial y}, \frac{\partial u}{\partial y} + \frac{\partial v}{\partial x}] \tag{5.17}$$

where the derivatives are computed using the chain rule given in the matrix form by

$$\begin{bmatrix} \frac{\partial}{\partial r} \\ \frac{\partial}{\partial s} \end{bmatrix} = \begin{bmatrix} \frac{\partial x}{\partial r} & \frac{\partial y}{\partial r} \\ \frac{\partial x}{\partial s} & \frac{\partial y}{\partial s} \end{bmatrix} \begin{bmatrix} \frac{\partial}{\partial x} \\ \frac{\partial}{\partial y} \end{bmatrix} \tag{5.18}$$

$$\begin{bmatrix} \frac{\partial}{\partial x} \\ \frac{\partial}{\partial y} \end{bmatrix}_{\substack{r=r_i \\ s=s_j}} = J_{ij}^{-1} \begin{bmatrix} \frac{\partial}{\partial r} \\ \frac{\partial}{\partial s} \end{bmatrix}_{\substack{r=r_i \\ s=s_j}} \tag{5.19}$$

Finally, using the above shape functions, the following are attained

$$\begin{bmatrix} \frac{\partial u}{\partial x} \\ \frac{\partial u}{\partial y} \end{bmatrix}_{\substack{r=r_i \\ s=s_j}} \tag{5.20a}$$

$$= \frac{1}{4} J_{ij}^{-1} \begin{bmatrix} -(1-s_j) & 0 & (1-s_j) & 0 & (1+s_j) & 0 & -(1+s_j) & 0 \\ -(1-r_i) & 0 & -(1+r_i) & 0 & (1+r_i) & 0 & (1-r_i) & 0 \end{bmatrix}_{\substack{r=r_i \\ s=s_j}} \hat{u}$$

$$\begin{bmatrix} \frac{\partial v}{\partial x} \\ \frac{\partial v}{\partial y} \end{bmatrix}_{\substack{r=r_i \\ s=s_j}} \tag{5.20b}$$

$$= \frac{1}{4} J_{ij}^{-1} \begin{bmatrix} 0 & -(1-s_j) & 0 & (1-s_j) & 0 & (1+s_j) & 0 & -(1+s_j) \\ 0 & -(1-r_i) & 0 & -(1+r_i) & 0 & (1+r_i) & 0 & (1-r_i) \end{bmatrix}_{\substack{r=r_i \\ s=s_j}} \hat{u}$$

where $\hat{\boldsymbol{u}}^T = [u_1, v_1, u_2, v_2, u_3, v_3, u_4, v_4]$. The stiffness matrix is then obtained from

$$\boldsymbol{K} = \int \boldsymbol{F} dr.ds.dt = \int \boldsymbol{B}^T \boldsymbol{C} \boldsymbol{B} (detJ) dr.ds.dt \tag{5.21}$$

where matrix B relates the strains (Equation 5.17) and displacements according to

$$\epsilon_{ij} = B_{ij} \hat{u} \tag{5.22}$$

The solution to $KU = R$ is obtained after imposing the boundary conditions by elimination of rows and columns corresponding to the constrained degrees of freedom ($\widetilde{\boldsymbol{K}}$). For instance, for case number 1 (Figure 5.4), the unconstrained degrees of freedom are u_2, u_3, v_3, and v_4, thus $\widetilde{\boldsymbol{U}} = \begin{bmatrix} u_2 \\ u_3 \\ v_3 \\ v_4 \end{bmatrix}$, $\widetilde{\boldsymbol{R}}^T = \begin{bmatrix} 0 \\ 0 \\ -1 \\ -1 \end{bmatrix}$, and $\widetilde{\boldsymbol{K}} = \begin{bmatrix} K_{33} & K_{35} & K_{36} & K_{38} \\ K_{53} & K_{55} & K_{56} & K_{58} \\ K_{63} & K_{65} & K_{66} & K_{68} \\ K_{83} & K_{85} & K_{86} & K_{88} \end{bmatrix}$,

assuming the magnitude of applied forces is 1 in the appropriate units. For this problem, considering plane strain conditions yields:

$$\begin{bmatrix}\sigma_{11}\\ \sigma_{22}\\ \sigma_{12}\end{bmatrix} = \begin{bmatrix}C_{11} & C_{12} & 0\\ C_{12} & C_{22} & 0\\ 0 & 0 & C_{33}\end{bmatrix}\begin{bmatrix}\epsilon_{11}\\ \epsilon_{22}\\ \epsilon_{12}\end{bmatrix} \tag{5.23}$$

$$\sigma_{11} = (C_{11} - \nu C_{12})\epsilon_{11} \tag{5.24a}$$

$$\sigma_{22} = \left(-\frac{C_{12}}{\nu} + C_{22}\right)\epsilon_{22} \tag{5.24b}$$

$$C = \frac{E(1-\nu)}{(1+\nu)(1-2\nu)}\begin{bmatrix}1 & \frac{\nu}{1-\nu} & 0\\ \frac{\nu}{1-\nu} & 1 & 0\\ 0 & 0 & \frac{1-2\nu}{2(1-\nu)}\end{bmatrix} \tag{5.25}$$

Upon obtaining $\widetilde{\boldsymbol{U}}$, the stresses and strains can be computed using Equations 5.22 through 5.25. MATLAB was used for performing these "hand calculations". The resulting quantities were compared with the outcome of FE analysis with the linear elastic formulation of Abaqus material library, the FE analysis using the linear elastic UMAT, and FE analysis using the linear elastic UHYPER.

The second step for testing the UMAT formulation was comparing its output using the formulation of the strain energy density function given in Equation 4.4, with the output of Abaqus UHYPER subroutine which requires a much simpler formulation. The confined compression experiment was simulated using the formulation of the material in UMAT and UHYPER.

The user subroutine UHYPER can be used for defining the strain energy density function for isotropic hyperelastic materials; however, it does not allow incorporation of "add-ons" such as adaptivity of a material to mechanical loading which makes UMAT the only viable option for mechanobiological studies. The constitutive behavior of a hyperelastic material in UHYPER is defined as a total stress–total strain relationship, rather than as the rate formulation. It is based on the deviatoric part of the deformation with the volumetric changes eliminated, i.e. the (deviatoric) deformation gradient is defined as $\overline{\boldsymbol{F}} = J^{-1/3}\boldsymbol{F}$, where $\boldsymbol{F}$ is the total deformation gradient and J is the total volume change given by $J = det\ (\boldsymbol{F})$. The deviatoric stretch matrix (the left Cauchy-Green strain tensor) of $\overline{\boldsymbol{F}}$ is given by

$$\overline{\boldsymbol{B}} = \overline{\boldsymbol{F}}.\overline{\boldsymbol{F}}^{T} \tag{5.26}$$

The strain invariants are then defined as

$$\begin{aligned} \bar{I}_1 &= trace(\overline{\boldsymbol{B}}) = \boldsymbol{I}:\overline{\boldsymbol{B}} \\ \bar{I}_2 &= \frac{1}{2}(\bar{I}_1^2 - trace(\overline{\boldsymbol{B}}.\overline{\boldsymbol{B}})) = \frac{1}{2}(\bar{I}_1^2 - \boldsymbol{I}:\overline{\boldsymbol{B}}.\overline{\boldsymbol{B}}) \end{aligned} \tag{5.27}$$

where $\boldsymbol{I}$ is the unit tensor.

For isotropic, compressible materials the strain energy, ψ, is a function of $\bar{I}_1$, $\bar{I}_2$, and J:

$$\psi = \psi(\bar{I}_1, \bar{I}_2, J) \tag{5.28}$$

The stress is decomposed into the equivalent pressure stress,

$$p = -\frac{1}{3}\boldsymbol{I}:\boldsymbol{\sigma} \tag{5.29}$$

and the deviatoric stress,

$$\boldsymbol{S} = \boldsymbol{\sigma} + p\boldsymbol{I} \tag{5.30}$$

where $\boldsymbol{\sigma}$ are the components of the Cauchy (true) stress. Abaqus/Standard allows strain energy potentials to be defined for isotropic materials via user subroutine UHYPER by programming ψ and the first, second, and third derivatives of ψ with respect to $\bar{I}_1$, $\bar{I}_2$, and J in the subroutine. Accordingly, the strain energy density function of interest (Equation 5.4) takes the following form

$$\psi = \alpha_0 \frac{e^{\alpha_1\left(J^{2/3}\bar{I}_1-3\right)+\alpha_2\left(J^{4/3}\bar{I}_2-3\right)}}{J^{2\beta}} \tag{5.31}$$

where the $\bar{I}_1$ and $\bar{I}_2$ are the first and second strain invariants of the deviatoric stretch matrix (the left Cauchy-Green strain tensor) of $\overline{\boldsymbol{F}}$. The following derivatives were programmed in the UHYPER subroutine:

$$\frac{\partial\psi}{\partial\bar{I}_1} = \alpha_1 J^{2/3}\psi$$

$$\frac{\partial\psi}{\partial\bar{I}_2} = \alpha_1 J^{4/3}\psi$$

$$\frac{\partial\psi}{\partial J} = P\psi$$

where $P = \frac{2}{3}\alpha_1 \bar{I}_1 J^{-1/3} + \frac{4}{3}\alpha_2 \bar{I}_2 J^{1/3} - 2\beta J^{-1}$.

$$\frac{\partial^2 \psi}{\partial \bar{I}_1^2} = \alpha_1^2 J^{4/3} \psi$$

$$\frac{\partial^2 \psi}{\partial \bar{I}_2^2} = \alpha_2^2 J^{8/3} \psi$$

$$\frac{\partial^2 \psi}{\partial J^2} = [Q + P^2]\psi$$

where $Q = -\frac{2}{9}\alpha_1 \bar{I}_1 J^{-4/3} + \frac{4}{9}\alpha_2 \bar{I}_2 J^{-2/3} + 2\beta J^{-2}$.

$$\frac{\partial^2 \psi}{\partial \bar{I}_1 \partial \bar{I}_2} = \alpha_1 \alpha_2 J^2 \psi$$

$$\frac{\partial^2 \psi}{\partial \bar{I}_1 \partial J} = \left[\alpha_1 J^{2/3} P + \frac{2}{3}\alpha_1 J^{-1/3}\right]\psi$$

$$\frac{\partial^2 \psi}{\partial \bar{I}_2 \partial J} = \left[\alpha_2 J^{4/3} P + \frac{4}{3}\alpha_2 J^{1/3}\right]\psi$$

$$\frac{\partial^3 \psi}{\partial \bar{I}_1^2 \partial J} = \alpha_1 J^{2/3} \frac{\partial^2 \psi}{\partial \bar{I}_1 \partial J} + \frac{2}{3}\alpha_1^2 J^{1/3}\psi$$

$$\frac{\partial^3 \psi}{\partial \bar{I}_2^2 \partial J} = \alpha_2 J^{4/3} \frac{\partial^2 \psi}{\partial \bar{I}_2 \partial J} + \frac{4}{3}\alpha_2^2 J^{5/3}\psi$$

$$\frac{\partial^3 \psi}{\partial \bar{I}_1 \partial \bar{I}_2 \partial J} = \left[\frac{2}{3}\alpha_1^2 \alpha_2 \bar{I}_1 J^{5/3} + \frac{4}{3}\alpha_1 \alpha_2^2 \bar{I}_2 J^{7/3} - 2\alpha_1 \alpha_2 (\beta - 1) J\right]\psi$$

$$\frac{\partial^3 \psi}{\partial \bar{I}_1 \partial J^2} = \left[-\frac{2}{9}\alpha_1 J^{-4/3} + \alpha_1 J^{2/3}(Q + P^2) + \frac{4}{3}\alpha_1 J^{-1/3} P\right]\psi$$

$$\frac{\partial^3 \psi}{\partial \bar{I}_2 \partial J^2} = \left[\frac{4}{9}\alpha_2 J^{-2/3} + \alpha_2 J^{4/3}(Q + P^2) + \frac{8}{3}\alpha_2 J^{1/3} P\right] \psi$$

$$\frac{\partial^3 \psi}{\partial J^3} = \left[P^3 + 3PQ + \frac{8}{27}\alpha_1 \bar{I}_1 J^{-7/3} - \frac{8}{27}\alpha_2 \bar{I}_2 J^{-5/3} - 4\beta J^{-3}\right] \psi$$

5.2.1 FEM of Confined and Unconfined Compression Experiments

The values of mechanical properties were those obtained as described in the previous section. An axisymmetric model of the confined compression configuration was meshed with 8-noded axisymmetric pore-pressure elements (CAX8P). To represent the porous indenter, free draining condition was prescribed on the top surface by defining a zero pore pressure boundary condition. The rest of the surfaces were modeled as impermeable. Two cases were studied: (1) the solid matrix was assumed linear elastic according to the infinitesimal strain biphasic theory, with including strain-dependent permeability effects (nonlinear biphasic theory), (2) the solid matrix was represented by the user material, while also considering strain-dependent permeability effects.

The same FE model was utilized to simulate an unconfined compression experiment; only the boundary conditions on the top surface and on the perimeter were changed to no-draining and free-draining respectively, as an impermeable platen was used in the experiment and the tissue was unconfined laterally. The loading history of the unconfined compression experiment was prescribed for the pressing platen. Response of the tissue was predicted by the user material, and the slope of the line fitted to its equilibrium stress-strain data was compare with the Young's modulus obtained from line fitting to the experimental data, as described in the previous section of this chapter.

Strain-dependent permeability may be defined in Abaqus as a function of void ratio (e), irrespective of the choice of a standard or user-defined material model. Abaqus takes into account the porosity of the medium through definition of this parameter which is taken as the ratio of fluid volume over solid volume. The permeability equation (Equation 3.12 therefore, has to be reshaped as a function of void ratio. Per definition of the void ratio in Abaqus we have $e = \phi^f/\phi^s = (\lambda - \phi_0)/\phi_0$, and the initial void ratio as $e_0 = (1 - \phi_0)/\phi_0$, leading to $\lambda = (e + 1)/(e_0 + 1)$. Thus:

$$k = k_0 \left(\frac{e}{e_0}\right)^2 \exp\left(\frac{M\left[\left(\frac{e+1}{e_0+1}\right)^2 - 1\right]}{2}\right) \tag{5.32}$$

where ϕ^f and ϕ^s are fluid and solid volume fractions, and ϕ_0 is the dry weight percentage of the tissue. For small strains: $\epsilon = \lambda - 1 = (e - e_0)/(e_0 + 1)$, and Equation 5.32 reduces to $k = k_0\, exp(M\epsilon) = k_0 exp\,[M(e - e_0)/(e_0 + 1)]$. The permeability defined in the biphasic theory must be converted to that of the poroelastic model through $k' = \rho k$, where ρ is the volume weight of the interstitial fluid which was assumed to be equal to that of water ($\rho = 9.81\times10^{-6}$ N/mm^{-3}). The initial void ratio was calculated as 6.7 using the 13.1% value of dry weight found for this tissue.

5.2.2 Whole Tissue Structure Experiment

The finite deformation biphasic theory was formulated for implementation in finite element programs by taking advantage of the soft tissue material parameters obtained from common test geometries used for mechanical characterization of the tissue (e.g.,

indentation, confined and unconfined compression tests). These properties were however obtained using compression tests while the model is expected to be used in the analysis of general stress problems. To evaluate the capability of the developed material model in prediction of the tissue response under general loading conditions, a whole tissue structure of human fetal talus - the same material type from which the samples were excised for mechanical characterization - was tested in a cantilever-like configuration. In order to reconstruct the geometry to be meshed for FE, the tissue was scanned in the micro-CT scanner. As the talus anlage was partly ossified it was scanned twice (at 17.2 μm pixel size): once before the test to obtain scans of the ossific nucleus (the bony region inside the tissue), and once after the experiment by applying a coat of contrast material on the surface of the cartilage to scan the outer surface since cartilage is rather transparent to the X-rays. Three-dimensional reconstruction of the geometries was performed using the scanner software (SkyScan1172), followed by Geomagic Qualify 12 (Geomagic Inc., Research Triangle Park, NC). Before imaging, the area to the left of the plane (Figure 5.6) was embedded in a polymer block using cyanoacrylate and a mixture of contrast agent and dental cement. The tissue was submerged in PBS containing enzyme inhibitors during the experiment. A stress relaxation test was performed by loading the tissue with a thin cylindrical bar (D = 2.85mm) parallel to the Y axis and 10mm from the surface of the embedding block (Figure 5.6). The prescribed displacement history of the bar involved two cycles of loading (2mm displacement) at a rate of 0.1 mm/s followed by stress relaxation periods of 900s. This was assessed enough time to allow full recovery of the tissue.

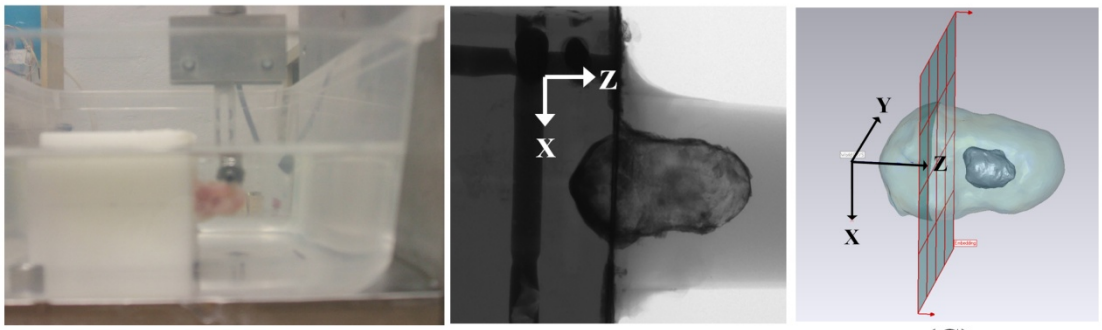

(A) (B) (C)

Figure 5.6. Testing of the whole talus and geometry reconstruction: (A) Cantilever test set-up with talus embedded in a box and submerged in liquid; (B) Micro-CT scan of the cartilage anlage coated with contrast agent displaying the thru holes filled with contrast material to help build a coordinate system for alignment of the two scans; (C) Reconstructed geometries of the cartilage anlage and the ossific nucleus displaying the same set of axes in Geomagic Qualify.

Preprocessing for finite element analysis was done in Patran 2008 r1 (MSC Software Corp., Santa Ana, California). The 10-node modified tetrahedron elements (C3D10M) were used to mesh the ossified region, and 10-node modified pore pressure tetrahedron elements (C3D10MP) were used for the cartilaginous region. Zero-flow boundary conditions were applied on the embedded surface and the area of contact between the bar and the tissue, with free-flow conditions on the rest of the surfaces. The loading bar was modeled as a rigid surface, and finite sliding contact was defined between the bar and the tissue surface. The ramping history of the experiment was prescribed for the loading bar. Taking the density of newly mineralized bone as $\rho = 0.24$ g/cm^3 [113] the material parameters of the ossified region were calculated according to the empirical equations $\nu = 0.2$ and E(MPa)=$2014\rho^{2.5}$ for $\rho \leq 1.2$ g/cm^3 [148]

resulting in $E = 56.83$ MPa. The mechanical properties of cartilage were those presented in the Chapter 6. The initial void ratio was taken to be 6.7 based on the dry weight measurement.

Two studies were conducted for comparison: one employed the user material for modeling the solid matrix, and the other modeled the tissue according to the nonlinear biphasic theory (linear elastic matrix while considering strain-dependent permeability). Properties of the ossified region were the same for both cases. Sum of the contact forces from the two models and the experiment were compared.

5.3 Clubfoot Treatment

5.3.1 Image Acquisition and Processing

MRI scans were obtained during weekly serial manipulation and corrective casting therapy initiated on a total of 7 newborn infants with unilateral right idiopathic congenital clubfoot deformity. The name codes used throughout the text, age, gender, and number of treatment sessions are indicated in Table 5.1. The therapy, using the Ponseti technique, was conducted by Dr. Shafique Pirani. MR imaging was conducted under the supervision of Dr. David Hodges. The testing protocol for a typical patient follows: visits (average number = 5) occurred at intervals decided by the physician for each patient (3-7 days) followed by a last visit after three weeks on average from the fifth visit. Appropriate doses of oral Chloral hydrate (50-75 mg/kg) were used to sedate the child as necessary during the MRI scanning process. Scans were performed with the feet casted to prevent movement. Session 1: the involved foot was casted and scanned in the deformed position. The cast was then removed; the foot was manipulated as per Ponseti Method and re-

Table 5.1. Patient information summary.

Code	Initial age (days)	Number of treatment sessions	Gender
S1	87	5	M
L1	25	5	M
K1	42	4	M
E2	31	5	M
T1	40	7	F
E1	26	4	M
B1	12	5	M

casted in the position obtained after manipulation (stressed) and rescanned. Session 2: the involved foot was scanned before removal of the cast applied in session 1. Cast was removed, the foot was allowed to adapt to the unstressed position and then it was re-casted and scanned. This cast was then removed; the foot was re-manipulated and casted into the position obtained with manipulation, and scanned. Sessions 3, 4 and 5: this sequence of manipulation, casting, and scanning was repeated. As per Ponseti treatment protocol, prior to application of the last cast on the involved foot in session 5, a complete percutaneous tenotomy of the tendoachilles was performed (except on patient K1) under local anesthetic to enhance correction of the equinus deformity. The uninvolved foot was casted and scanned in the neutral position each week. Last visit: only one MRI in the resting unloaded position was performed on the involved foot. The uninvolved foot was again casted and scanned in the neutral position. For some patients/treatment sessions scans of the neutral state were not taken due to patient's agitation.

All image acquisitions were performed using a 1.0 Tesla scanner (Horizon, GE Medical Systems, Milwaukee, WI). A transmit/receive wrist coil was placed over the foot to be scanned to maximize signal-to-noise ratio, yielding a 12cm field-of-view. Scanning covered the distal tibial shaft to the mid-metatarsal bones. The feet were scanned parallel

and perpendicular to the bimalleolar axis, yielding coronal and sagittal images. In these planes a 3D fast gradient echo (FGRE) sequence with inversion pulse was utilized with the following parameters as well as frequency selective fat saturation: TR (relaxation time)/TE (echo time) = 13.6ms/6.3ms; TI (inversion time) = 50ms; flip angle 10 degrees; 2 NEX (number of excitations); bandwidth 15.6 kHz; matrix 256×192, 2.4mm slice thickness with interpolation to 1.2mm and 0mm interslice gap, yielding a voxel dimension of 0.47×0.47 ×1.2mm. The MRI data were in DICOM format.

The MRI scans (in DICOM format) were imported into Analyze 10.0 (AnalyzeDirect, Inc., Overland Park, KS) for processing, including segmentation and volume rendering. The cartilaginous anlagen of talus, calcaneus, cuboid and navicular, as well as their ossific nuclei (where present) and the distal fibula and tibia were segmented and rendered as three-dimensional geometries. Where the scan qualities were poor, scans of the two sagittal and coronal views were first fused prior to segmentation to improve the image quality. The surface files were then exported in STL format (Stereolithography CAD format). All of the subsequent image analysis was performed in Geomagic Studio 12 and Geomagic Qualify 12.

Data of patient E2 was excluded in the subsequent analyses due to the unsatisfactory quality of MRI scans and consequently the resulting segmentation inaccuracies. Patient B1 was included in the analysis of section 4.3.2 but not in 4.3.3.

5.3.2 Growth, Ossification and Adaption Analysis

Volume and Shape Correction Analysis

The changes in positional relationships and shapes of the anlagen corresponding to the correction of the deformities (see 1.3) as a result of adaptation of the cartilaginous anlagen in the cast were studied qualitatively. For this purpose, assemblies were created of the geometries of the four hindfoot and midfoot anlagen under study, their ossific nuclei where present, and the distal tibia and fibula at each treatment session for the normal foot, and before and after cast application in the clubfoot. Figures were created of these assemblies in the three orthogonal anatomical views (sagittal, coronal, axial – see Appendix B) at each treatment session for each patient, portraying the three views side by side to allow comparison, illustrating the progression of correction in each patient during the treatment period. The figures are presented in Chapter 6. The correction in the deformities present in clubfoot patients (varus, adductus, cavus, and equinus) was followed throughout the treatment period.

To qualitatively assess the changes that occurred within the anlagen and the ossific nuclei during the period of treatment, measurements of their volumes at each treatment session were taken and analyzed in the form of the following parameters:

1- Degree of ossification calculated for both healthy and clubfoot sides as the ratio of ossific nucleus (ON) volume over the total anlage (ANL) volume: $DO = \frac{V_{ON}}{V_{ANL}}$.

2- Ratio of the clubfoot ON size to the normal ON size: $V_{ON-clubfoot}/V_{ON-normal}$.

3- Ratio of the clubfoot ANL size to the normal ANL size: $V_{ANL-clubfoot}/V_{ANL-normal}$.

4- Ratio of the degrees of ossification of the clubfoot to the normal side: $DO_{clubfoot}/DO_{normal}$.

Statistical analysis was performed to study the changes with time in several parameters: size of normal and clubfoot ossific nuclei and anlagen, degrees of ossification in normal and clubfoot (number 1 above); and the ratio of each of these parameters on the clubfoot side taken with respect to that on the normal side (numbers 2,3, and 4 above). For this purpose, correlation analysis was performed between time and these parameters for each anlage in each patient individually, with the time variable being the number of days as counted from the first day of treatment. The level at which correlations were considered significant was $p = 0.05$ with a 1-tailed analysis. Simple regression analysis was performed for the same parameters versus time, with time as the independent variable. Output of the correlation (Pearson correlation coefficients and significance levels) and regression analyses are summarized in Table 6.2 through Table 6.5 for all cases where the significance level from the correlation analysis was $p < 0.15$. To compare across patients and between the normal and clubfoot sides, the regression coefficients provided in these tables were calculated based on the dependent variables normalized by their corresponding initial values. Since cuboid did not have an ossific nucleus in B1 in the first visit, the values were normalized by those of the second visit. All the statistical analyses in the present study were performed using PASW Statistics 18.0.0 (IBM Corp., Somers, NY).

As opposed to the previous analysis which was performed for each patient individually, a separate statistical analysis was carried out on the data of each anlage

from all the patients together. The same parameters were studied with the exception that the time variable was equal to the age of the patient in days in this case, i.e., for the global analysis the independent variable (time) from the previous analysis was shifted by different magnitudes for each patient, as treatment was initiated at different ages in different infants. One purpose for this rather different analysis was to obtain general regression models constructed based on the entire population of patients describing growth as a function of age. The level at which an effect was considered significant was considered $p = 0.05$; however, similar to the previous analysis the exact p values are included in Table 6.6. Simple linear regression was carried out taking age as the independent variable. Regression coefficients are presented in Table 6.6 for cases where $p < 0.1$.

To compare the rates of ossification for the two feet for each patient, similar analysis to the previous paragraph was conducted for individual patients. The rate of ossification was defined as the slope of the linear regression model relating the ossific nucleus volume with age. Table 6.7 provides a summary of ossification rates for talus, calcaneus, and cuboid for the normal and clubfoot sides. In this part of the analysis, all regression models were included irrespective of the significance levels in the correlation analyses.

Finally, to assess whether or not these rates correlated with the age of patients, correlation analyses were performed between the slopes and the patient's age at the start of treatment. This was done for both normal and clubfoot groups for the talus, calcaneus,

and cuboid. The same analysis was conducted on the rate of change with time in the volume of cartilage anlage of all four anlagen.

FE Analysis of Relationships Between Treatment-Induced Mechanical Quantities and Ossification

The purpose of this part of the study was to delineate any relationships present between the amount of ossification obtained, and the mechanical quantities that were induced by the manipulation of the feet by the physician. The deformations that were introduced in the anlagen by treatment (described shortly) were inputted into a finite element model to determine the resulting distribution of various mechanical quantities throughout the anlagen and more specifically near the surface of the ossific nucleus.

All of the geometries were first repaired and smoothed upon importing into Geomagic Studio to get a closed surface that could provide a good mesh for FE analysis. The treatment-induced deformations were obtained in Geomagic Qualify by creating a full deviation map between the surface of the anlage before applying the new cast, and after the foot were put in a new cast upon being manipulated into a more corrected shape. Before this task could be done, the two objects needed to be aligned. This is because the position of the foot with respect to the coordinate system of the MRI scanner is different each time and the two objects have to be brought to a common point in the space and aligned based on their common features. It is assumed that since the ossific nuclei constitute of bone tissue, they remain relatively undeformed under the manipulative forces. Therefore, a local coordinate system was set up for each ossific nucleus based on its geometric centroid and principal axes of inertia, and both the post-cast ossific nucleus

and its associated anlage were registered to the corresponding pre-cast geometries by aligning the coordinate systems of the two ossific nuclei. After this alignment, the deviation between the surfaces of the anlagen was obtained (Figure 5.7).

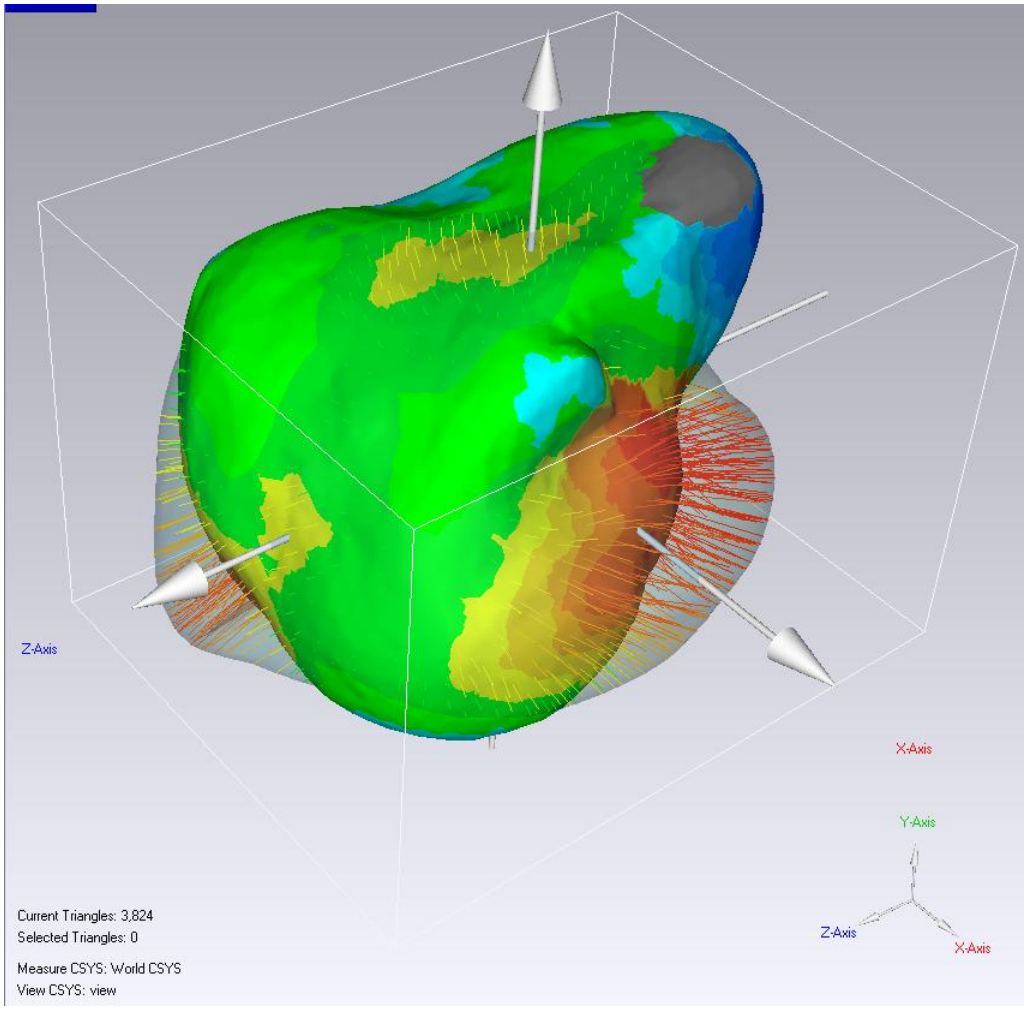

Figure 5.7. Calculation of the deformation caused in the talus due to manipulation and casting. Whiskers show connections between points on the pre-cast surface (transparent) to the post-cast surface (colored solid).

To determine the growth in the ossific nucleus from each week to the following week, the same type of analysis was performed with the difference that to align the objects of the *n*th to the *n-1*th week, the coordinate systems of the ossific nuclei could no longer be used. The centroid and principal axes of inertia of the cartilage anlagen were used to register the two sets together in this case. The changes in the surface of the ossific nucleus were computed in the same manner as described above for cartilage. The deviation table populated in Geomagic Qualify was exported for the location set containing the nodes on the surface of the ossific nucleus (the comparison of geometries can only be performed between two surfaces and not throughout the entire object). Custom codes written in MATLAB were used for translating and transferring of the data between Patran and Geomagic Qualify. This made possible for the deviation information to be outputted for the mid-side nodes as well by including them in the location set, although the original STL files used for 3D comparison analysis in Geomagic Qualify contained only the three vertices of each triangle.

The enhanced and aligned objects were then imported into Patran for FE pre-processing. As the geometrical information in an STL file format is based on the coordinates of the vertices of the triangles that the surface is broken down into, building a solid mesh based on these vertices creates four-node tetrahedron elements. For better accuracy, mid-side nodes were added to the surface elements prior to building a solid mesh. The resulting elements were ten-node tetrahedra. The material properties assigned to the cartilage and bone were as described in section 4.1.5.

The soils consolidation capability in Abaqus was used for modeling the cartilage tissue as biphasic. The ossific nucleus was modeled as linear elastic, thus automatically imposing a no-flow boundary condition on the interface of the ossified and unossified regions. All of the analyses were carried out twice. In the first study, the extracellular matrix of the cartilage anlage was represented with the UMAT formulation, whereas in the second study, the linear elastic formulation available in the Abaqus material library was used. The deformation applied on the surface of the anlagen by treatment forces was included in the FE analysis as ramping boundary conditions for the nodes of the cartilage anlage surface. Results of the analysis were written to .fil files for the cartilage elements neighboring the ossific nucleus. A custom written Fortran code was then used to read the output using the output keys, and to write to a text file. The quantities in the output request were von Mises stress, pressure stress, strain energy density, fluid volume ratio, magnitude of fluid velocity, and the pore pressure (of the fluid phase). FE analyses were conducted for all patients for every treatment session using the corresponding deformation field and geometries for that session. The material properties were assumed to remain constant from the beginning until the end of treatment period.

Two measures of growth were used for correlation analyses. The first was based on the change in the volume of ossific nucleus from each treatment session to the next, normalized by the initial size of the ossific nucleus to enable comparison across patients. The second was the amount of added tissue (in mm) in the direction normal to the surface of the ossific nucleus as obtained from Geomagic Qualify. This value was averaged for all the nodes on the surface of the ossific nucleus. Correlation analysis was performed between each measure of bone deposition as the dependent variable, and the mechanical

quantities listed in the previous paragraph as independent variables. The Pearson correlation coefficients and the significance levels were calculated using a 2-tailed analysis. Simple linear regression analysis was performed where a significant effect was detected ($p = 0.05$, 2-tailed). The analysis was carried out for both the linear elastic and UMAT material models.

CHAPTER 6. RESULTS

6.1 Mechanical Properties of Fetal Talus

The mean and standard deviation for the material coefficients, as obtained from the stress relaxation results of confined compression experiment, were: $H_{A0} = 0.11 \pm 0.04$ MPa, $\beta = 1.94 \pm 1.70$, $k_0 = 3.64 \pm 2.58 \times 10^{-14}$ $m^4N^{-1}s^{-1}$ and $M = 6.73 \pm 2.71$. The curve-fits of response showed very good agreement between theory and experiment for all specimens. A typical transient stress-relaxation response is shown in Figure 6.1, and the corresponding equilibrium stress-stretch curve for the same sample is shown in Figure 6.2. The goodness of fit was $r^2 = 0.989 \pm 0.022$ and $r^2 = 0.963 \pm 0.017$ for nonlinear curve fitting to the equilibrium stress-stretch data, and the transient stress-time data respectively. The specimens recovered $97.1\% \pm 2.6\%$ of their initial thickness after the confined compression experiment, prior to the unconfined compression experiment.

The mean and standard deviation for the Young's modulus, as obtained from the unconfined compression experiment, were: $E_s = 0.06 \pm 0.03$MPa, with a goodness of fit $r^2 = 0.958 \pm 0.038$ (Figure 6.3). The Poisson's ratio using the results of the two tests was $\nu_s = 0.37 \pm 0.09$, as obtained from Equation 4.2 by combining the value of H_{A0} and the Young's modulus.

6.2 Assessment of Fetal Anlage UMAT

The stress, strain, and displacement results of the five test cases examined to verify the general set up of the user material provided very good agreement among the three analyses: FE analysis with the linear elastic model of Abaqus material library, (2) FE

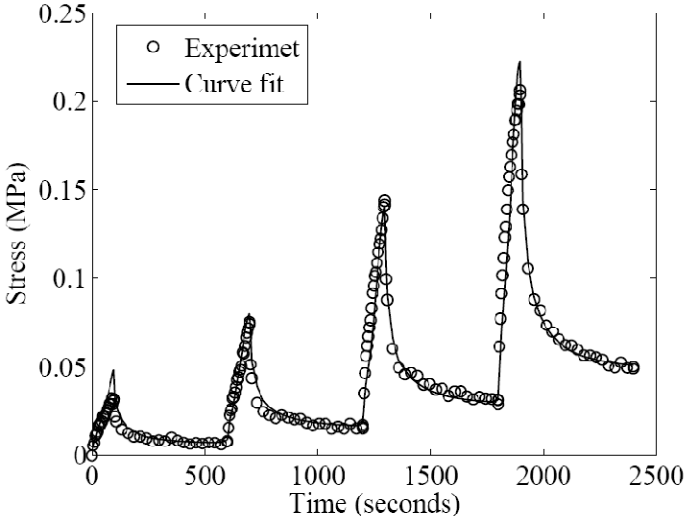

Figure 6.1. Stress relaxation results of confined compression experiment. The curve provides a close fit to the experimental data.

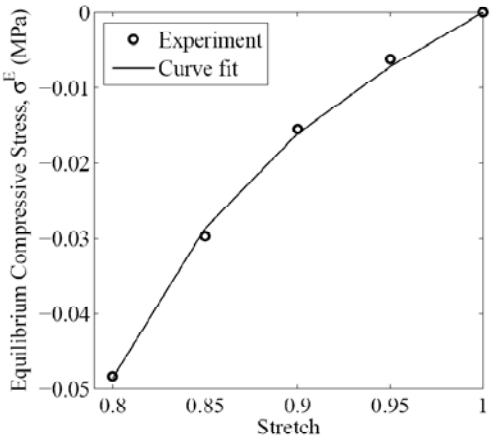

Figure 6.2. Equilibrium stress-stretch data of stress relaxation in confined compression, with a nonlinear curve fit. Compressive stiffening of the tissue can be noted by the departure of the response from a straight line.

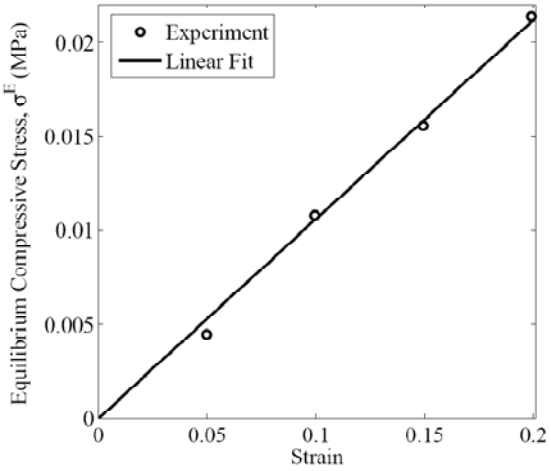

Figure 6.3. Data of stress relaxation experiment in unconfined compression. Linear response of the tissue in this testing configuration can be noted by the good agreement between a linear fir and the experimental data.

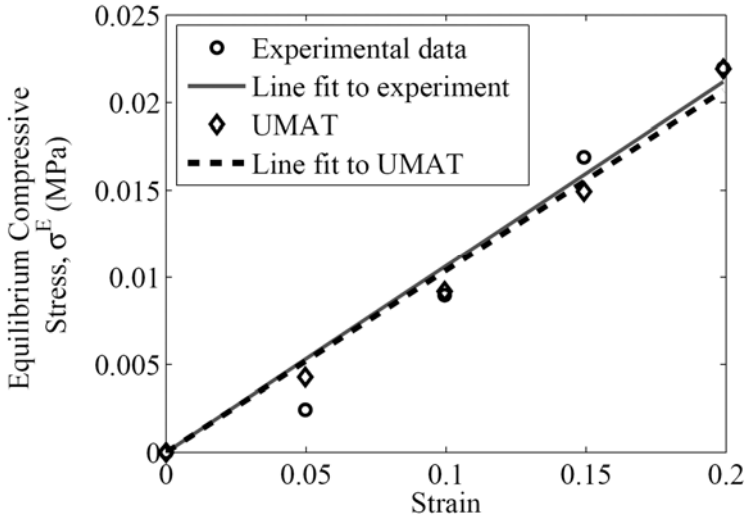

Figure 6.4. Equilibrium stress- strain data of an unconfined compression experiment, showing the experimental data, FE results using UMAT, and the linear fits to both. The Young's modulus obtained from UMAT is less than 2% different from that obtained from line fitting to the experimental data.

analysis using the UMAT with linear elastic formulation, and (3) hand calculations using the isoparametric formulation of the 4-node quadrilateral element.

Comparison of UHYPER and UMAT in simulation of the confined compression experiment resulted in identical stress-time curves. The line fit to the equilibrium stress-strain data of the FE simulation of unconfined compression, as obtained by applying the UMAT, yielded Young's moduli less than 2% different from those obtained from line fitting to the experimental data (Figure 6.4).

Results of the confined compression experiment simulation using the UMAT versus the nonlinear biphasic model are plotted in Figure 6.5 and overlaid on the experimental data. The nonlinear biphasic model underestimated the peak stress at large

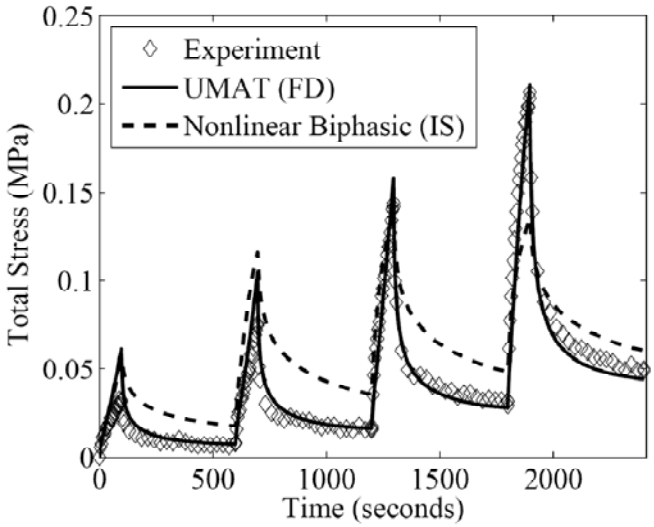

Figure 6.5. Confined compression experiment simulation with UMAT and nonlinear biphasic model overlaid on the stress - time test data (IS: Infinitesimal strain, FD: Finite deformation). The nonlinear biphasic overestimated the relaxation curve stress values.

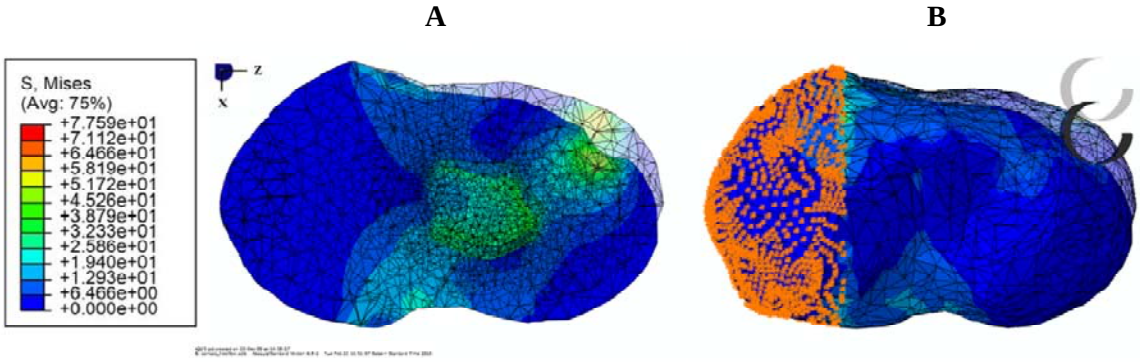

Figure 6.6. FE model of the whole tissue in cantilever loading with the deformed and undeformed shapes, (A) a sagittal section through the tissue displaying the von Mises stress contour in the cartilage and bone, (B) with loading bar on the right and the pinned nodes on the left representing the embedding block.

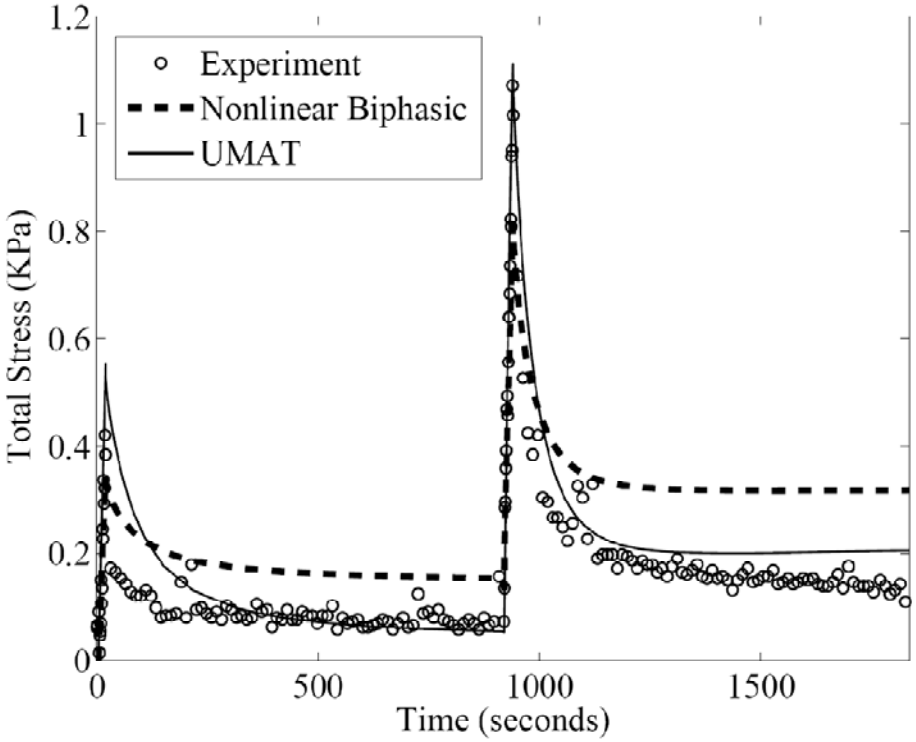

Figure 6.7. Total stress on the loading bar as sensed by the load cell in loading of the whole talus anlage in a stress relaxation test. Result of the simulation with the UMAT demonstrates closer resemblance than the nonlinear biphasic theory to the experiment.

strains (33% in the last cycle). The equilibrium stress values were off by 50%, 77%, 75%, and 33% in the first through the last cycle respectively. The relaxation rate predicted by this model was slower than the experiment. The peak stresses predicted by the UMAT at low strains were higher than the experimental values - twice as large in the first cycle, and larger by 38% in the second cycle; however, they were close to the fitted curve which was the source of the material parameters for the user material. The peak stresses at high strains (third and fourth cycles) and all of the equilibrium stress values corresponded closely with the experiment. The relaxation rate was similar to the experiment.

The total stress applied on the loading bar by the tissue under cantilever loading in the whole tissue structure experiment is plotted versus time in Figure 6.7. The output of simulations of this experiment in Abaqus using the developed UMAT as well as the nonlinear biphasic model is also demonstrated in the same figure. The nonlinear biphasic model yielded equilibrium stress values that were nearly twice as large as those of the experiment in both cycles. The peak stress predicted by the UMAT was 32% larger than that of the experiment in the first cycle, while the peak stress of the second cycle matched the experiment perfectly. The equilibrium stress of the first cycle had good agreement with the experiment; however, this value for the second cycle exceeded the experimental stress by 53%. Both models showed a slower relaxation rate than the experiment. At both low and high strains, the UMAT model showed slower relaxation rate than the experiment during the early relaxation period, and higher rate in the late relaxation period. Figure 6.6 portrays a section made through an overlay of deformed and undeformed meshes of the cartilaginous tissue with the ossified region showing in the center as one of the two higher stress areas.

6.3 Growth, Ossification, and Adaptation

6.3.1 Shape Correction Analysis

Manipulation and corrective casting immediately changed anlagen shape and relative positions toward normal. Most obvious were the abnormalities of the relative positions of the anlagen. Prior to corrective cast application the talus was plantarflexed; the navicular was medially and inferiorly displaced (most severe in T1, E2, L1 – Figure 6.8) relative to the talus and pressed against the medial malleolus (in S1 and L1 – Fig 6.8); the distal end

of the calcaneus was located immediately beneath the head of the talus; and the cuboid was displaced medially and plantarflexed relative to the calcaneus. Plantarflexion was most severe in three of the patients (L1, E2, and T1) where two (L1, T1) also displayed severe equinus deformity (Figure 6.9).

Application of the cast immediately improved the deformed configuration. The navicular moved away from the medial malleolus and was more centrally positioned on the head of the talus. The distal end of the calcaneus was no longer beneath the talus but displaced more laterally (everted). The cuboid moved laterally into a more central position relative to the calcaneus.

All patients except E2 and K1 underwent tenotomy which completed the correction by elimination of the remaining equinus deformity (Figure 6.9). Varus was the most severe in E2 and next in T1 (Figure 6.10). Parallelism of talus and calcaneus was corrected gradually as the lateral shift of the calcaneus and cuboid (Figure 6.10) and plantarflexion and equinus are corrected (Figure 6.9). The least degree of deformity was observed in K1.

6.3.2 Volume Analysis

Volume of ossific nuclei and anlagen averaged over the treatment period is tabulated in Table 6.1 for each patient.

The correlation analysis, as performed for individual patients, between the volumetric parameters and the number of days counted from the start of treatment (Tables 6.2 through 6.5) showed the most consistency across patients in the size of the clubfoot ossific nuclei in all of the anlagen except navicular (note that the ossification in

navicular normally does not occur in the clubfoot patients until the age of 3 or 4 [149]). Five of six patients showed significant positive correlations between the clubfoot ossific nucleus size and time in the talus, and five out of five in the cuboid (data of cuboid of T1 was not available). The same correlation was observed in the ossific nucleus of calcaneus in four of six patients. The next most consistent variation with age among patients corresponded with the change with time in the degrees of ossification: 4/6 in tali, 3/6 in calcanei, and 3/6 in cuboids. Next was the change with time in the size of normal anlagen: 4/6 in calcaneus anlagen, 3/6 in talus anlagen, 2/6 in navicular, and 1/6 in cuboid. Next, the ratio of degree of ossification in the clubfoot over the normal varied with time in the talus in 3/6 patients, in calcaneus in 2/6 patients, and in the cuboid in 2/5 patients. The degree of ossification increased with time in the talus, calcanei, and cuboids of one, two, and three of the patients respectively. Variation of the rest of the measures with age was different from patient to patient. Size of the normal ossific nucleus changed with time in the tali of 3/6 patients, calcanei of 2/6 patients, and cuboids of 2/6 patients. The clubfoot anlagen did not show much variation with time (1/6 talus, 2/6 calcaneus, 1/6 navicular, and 1/6 cuboid). The size ratio of the clubfoot to normal cartilage anlage increased with time in the navicular, cuboid, and calcaneus of one of the patients (K1), and also increased in the cuboid of L1. In the rest of the cases where effects were detected, the correlation coefficients were negative: talus of T1 and navicular of S1 and T1, i.e., 66% and 43% of the naviculars and of all the anlagen, respectively, that showed any significant correlation. Similar effects were present for the same parameter in the navicular of two more patients (E2 and B1) at lower levels of significance ($p = 0.101$ and $p = 0.126$ respectively). The size ratio of clubfoot to normal ossific nucleus showed a

positive correlation with time in the talus of one patient, and the cuboids of 2/5 patients. This value did not change significantly in the calcaneus. Effects were considered significant when $p < 0.05$; however, the results of correlation analyses and the coefficients of linear regression are summarized in Table 6.2 through Table 6.5 for all cases where $p < 0.15$.

The correlative analysis between the volumetric parameters and patients' age (in days) when data was grouped for all patients together (Table 6.6) revealed a significant correlation for the size of ossific nuclei and anlagen, and degrees of ossification for both clubfoot and normal sides in the talus, calcaneus, and the cuboid. The navicular had not developed an ossification center, thus, for this anlage only the size of normal and clubfoot anlagen, and the ratio of the latter to former were studied. Only the former two showed a significant correlation with the age of the patients during the period of treatment. The size ratio of clubfoot to normal anlagen did not produce a significant correlation with age for any of the anlagen. The ratios of clubfoot to normal ossific nucleus volume, and clubfoot to normal degree of ossification yielded a significant correlation with age in the talus, but not in the other two anlagen with ossification. All the correlation coefficients were positive, and are given in Table 6.6 along with the corresponding significance levels. Coefficients of the simple linear regression analyses are presented in Table 6.6 and plots are presented in Figure 6.11 and 6.12.

The rates of ossification appearing in Table 6.7 show that during the period of treatment the clubfoot ossific nucleus grew faster than the normal side indicating that the difference between the two sides decreases with time. Exceptions were the calcanei of

patients E2 and T1. Data of cuboid ossific nucleus of T1 were not available. Interestingly, the cuboid grew the fastest of all the four anlagen during this period on both sides, and also faster on the clubfoot side. Values of ossific nucleus sizes normalized to first session are plotted in Figure 6.13 for three of the anlagen from different patients.

Correlation analysis of ossification rates (values in Table 6.7) with time (age) showed a decrease with time for both the ossific nucleus and anlage of the clubfoot and normal foot (e.g., Figure 6.14). These correlations were at significant levels for the anlage ($r = -0.770$, $p = 0.037$) and ossific nucleus ($r = -0.778$, $p = 0.034$) of normal talus, indicating a decrease in growth rate with age. The other correlations with $p < 0.1$ corresponded to the talus clubfoot anlage ($r = -0.677$, $p = 0.070$), calcaneus normal anlage ($r = -0.650$, $p = 0.081$), and cuboid clubfoot ossific nucleus ($r = -0.742$, $p = 0.076$). Figure 6.14 shows the decline in the rate of ossification in normal talus in all patients plotted against age of patient at the time treatment was initiated.

Table 6.1. Mean (± std. dev.) of the volume of ossific nuclei and anlagen in mm^3 and percentage of ossification. Average taken over the period of treatment.

Navicular	Anlage	
Patient	**Normal**	**Clubfoot**
S1	697.36±68.51	739.37±95.83
L1	558.25±100.04	295.21±36.07
K1	447.86±102.62	321.78±68.76
E2	595.79±88.44	332.70±51.29
T1	434.08±87.86	350.42±96.29
B1	458.01±118.93	316.68±44.43

Table 6.1 (Continued)

Talus	Ossific Nucleus		Anlage		% Ossification	
Patient	Normal	Clubfoot	Normal	Clubfoot	Normal	Clubfoot
S1	833.45±61.87	457.18±32.03	3792.05±225.43	2994.83±153.41	22.97±0.66	15.33±1.69
L1	286.89±16.65	94.76±17.42	2292.18±223.69	1451.62±1.07	12.62±1.07	6.58±1.13
K1	607.54±54.50	344.92±78.32	2708.87±89.65	2119.30±118.71	22.41±1.67	16.17±2.87
E2	538.53±96.32	197.34±67.18	3109.51±307.46	1760.51±252.38	17.22±1.44	11.13±3.28
T1	416.91±64.13	162.61±23.45	2360.30±251.58	1605.08±233.95	17.87±3.56	10.34±2.35
B1	406.65±83.51	168.41±41.51	2557.51±385.50	1751.48±257.00	15.89±2.08	9.62±0.87

Calcaneus	Ossific Nucleus		Anlage		% Ossification	
Patient	Normal	Clubfoot	Normal	Clubfoot	Normal	Clubfoot
S1	1498.05±82.34	1370.56±178.16	4607.76±289.58	3962.96±295.5	32.53±0.49	34.60±3.74
L1	736.53±38.58	607.04±59.08	2812.76±288.74	2175.34±182.31	26.31±1.77	27.88±1.21
K1	958.61±53.97	845.93±91.48	2776.8763±237.97	2436.08±249.15	34.76±4.21	34.78±2.75
E2	716.82±67.25	630.67±101.68	3043.83±261.44	2446.05±326.59	23.58±1.81	25.85±2.85
T1	663.38±152.81	612.53±104.39	2390.68±227.59	1937.29±151.76	27.50±4.61	31.50±3.64
B1	691.26±144.66	574.16±150.85	2826.71±467.73	2231.67±295.43	24.57±3.91	24.65±3.88

Table 6.1 (continued).

Cuboid	Ossific Nucleus		Anlage		% Ossification	
Patient	**Normal**	**Clubfoot**	**Normal**	**Clubfoot**	**Normal**	**Clubfoot**
S1	254.9198±11.50	145.8670±26.33	1334.9568±101.53	979.5488±92.67	19.20±1.96	14.91±2.37
L1	27.2372±22.45	24.4998±21.62	689.0530±19.98	529.1676±114.61	4.02±3.35	4.32±3.09
K1	105.77±26.43	59.70±22.40	742.20±153.47	524.14±59.86	15.11±6.53	11.19±3.32
E2	147.18±40.10	49.74±56.14	969.72±114.86	673.07±169.64	15.09±3.17	6.40±6.85
T1	106.99±25.96	-	605.10±140.66	515.34±159.02	17.79±2.90	106.99±25.96
B1	50.46±45.04	22.50±26.82	813.07±141.76	635.83±87.14	5.61±4.89	3.23±3.50

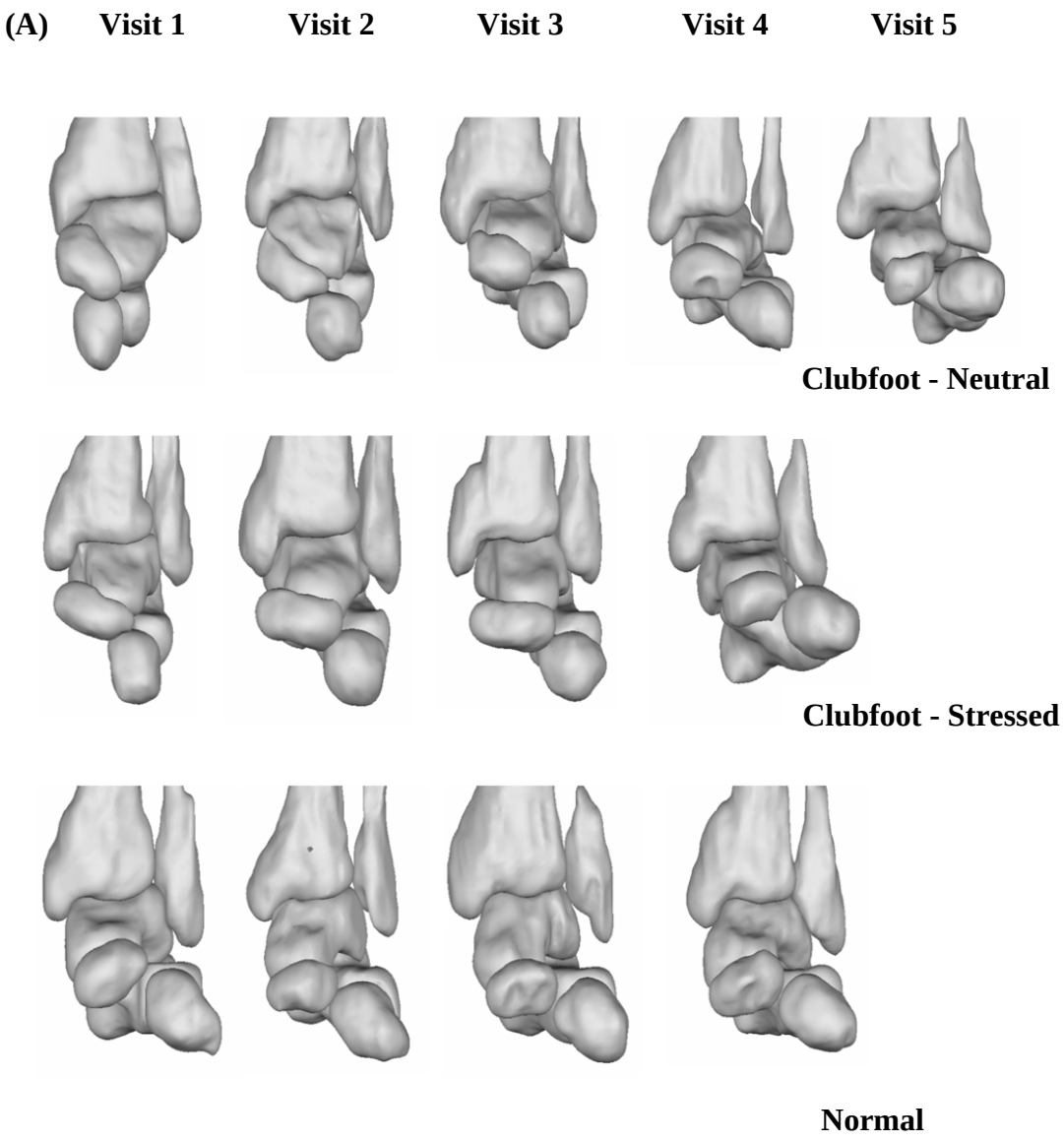

Figure 6.8. Sagittal views of patients' reconstructed bone geometries: (A) S1, (B) L1, (C) K1, (D) E2, (E) T1.

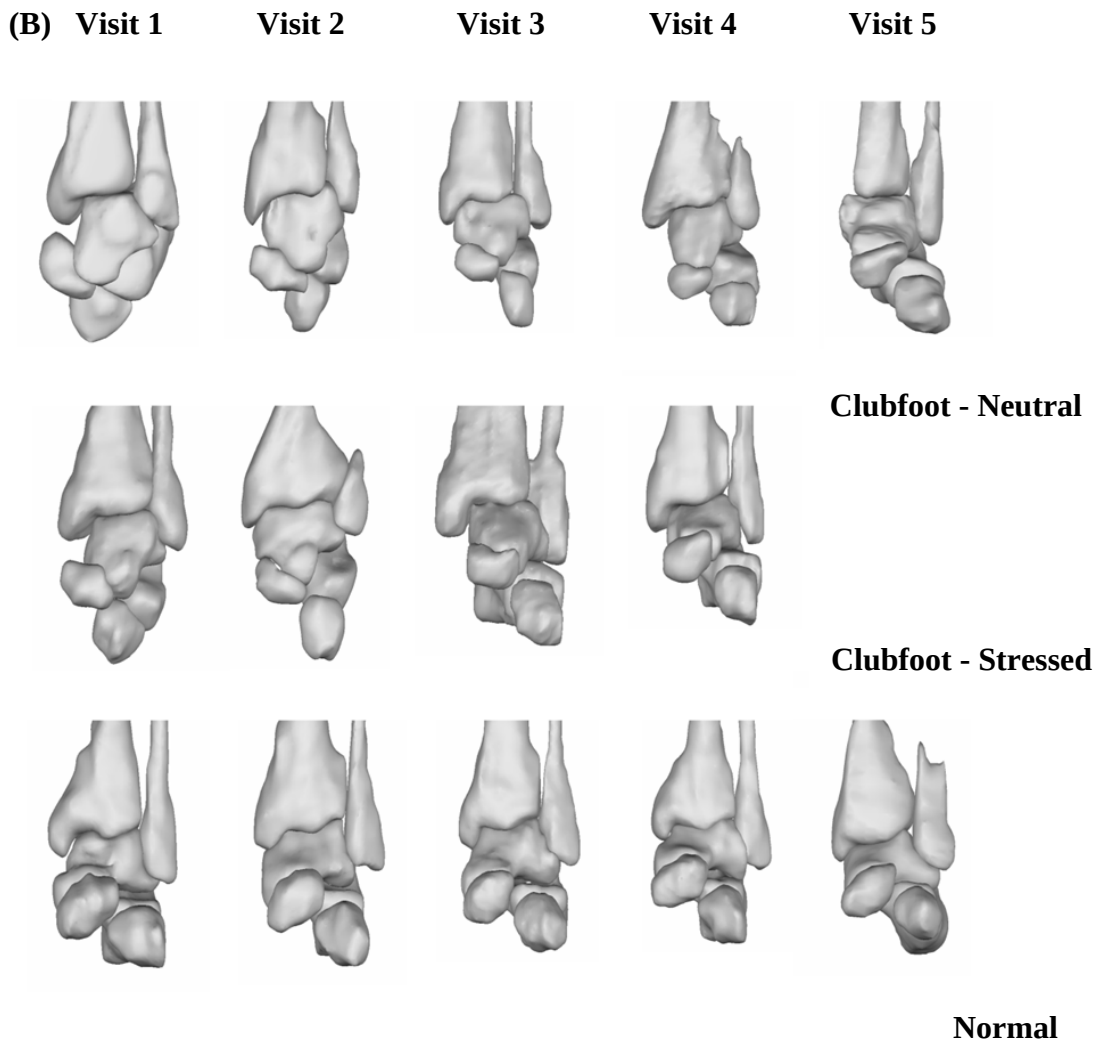

Figure 6.8 (continued).

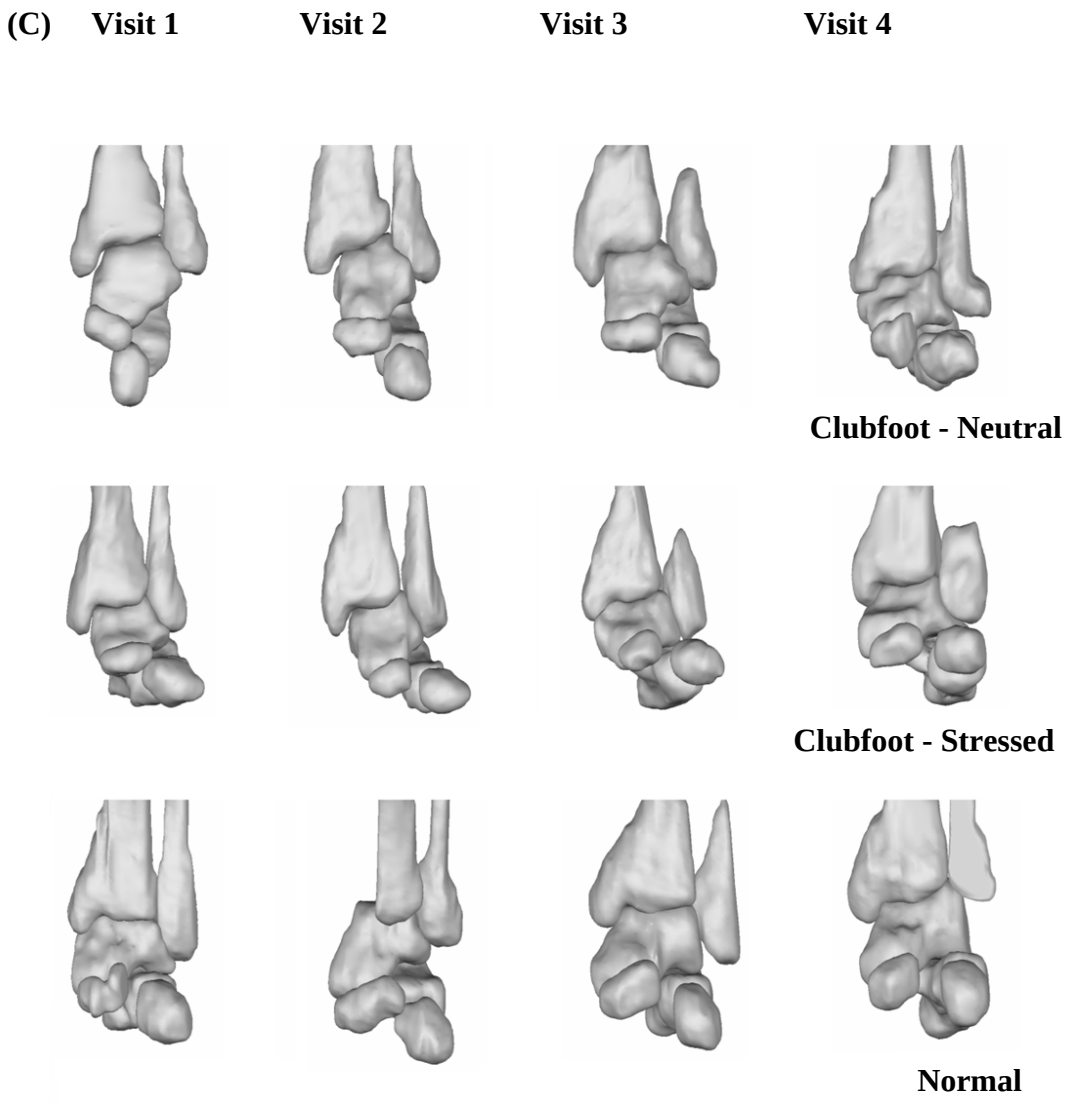

Figure 6.8 (continued).

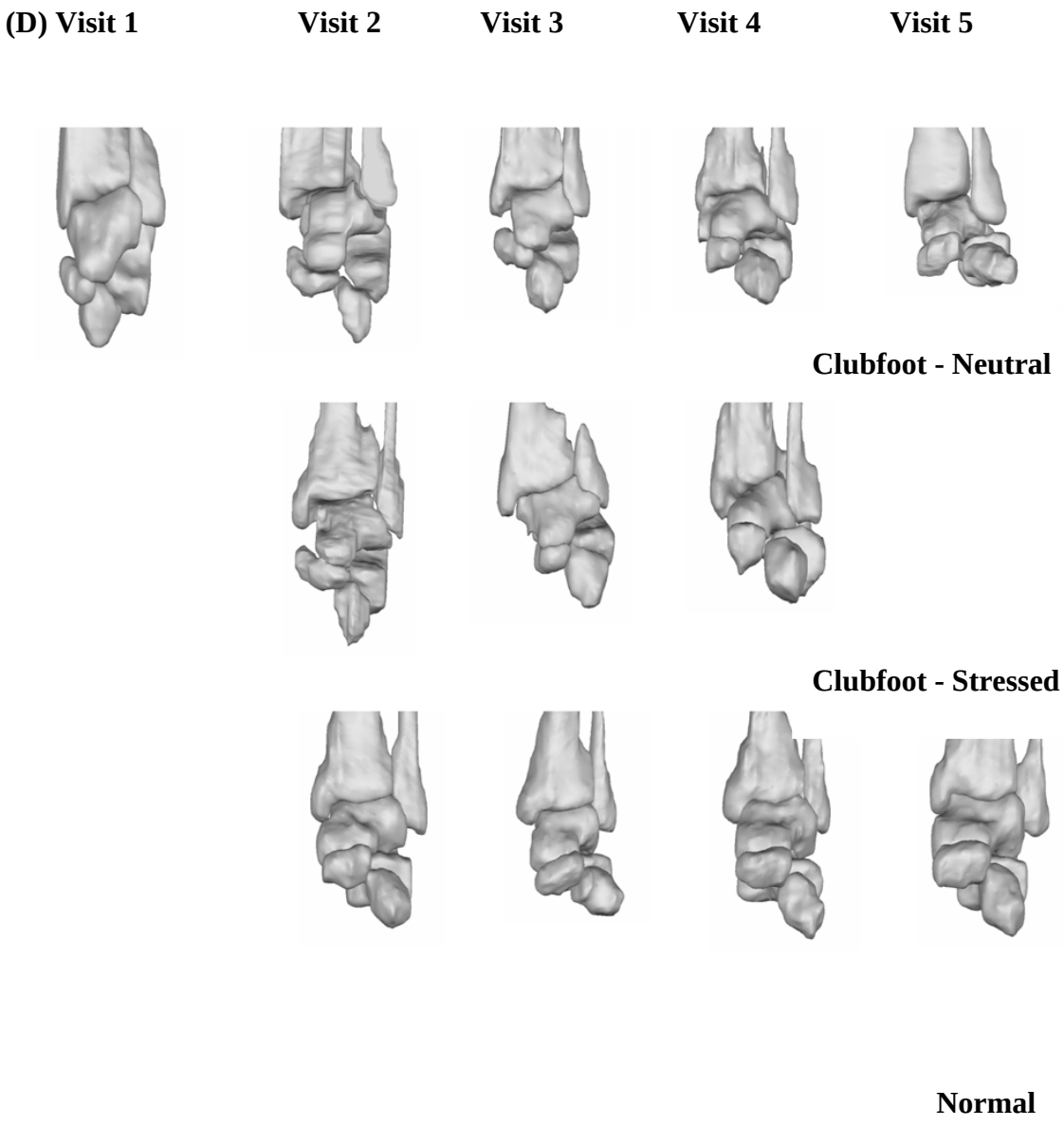

Figure 6.8 (continued).

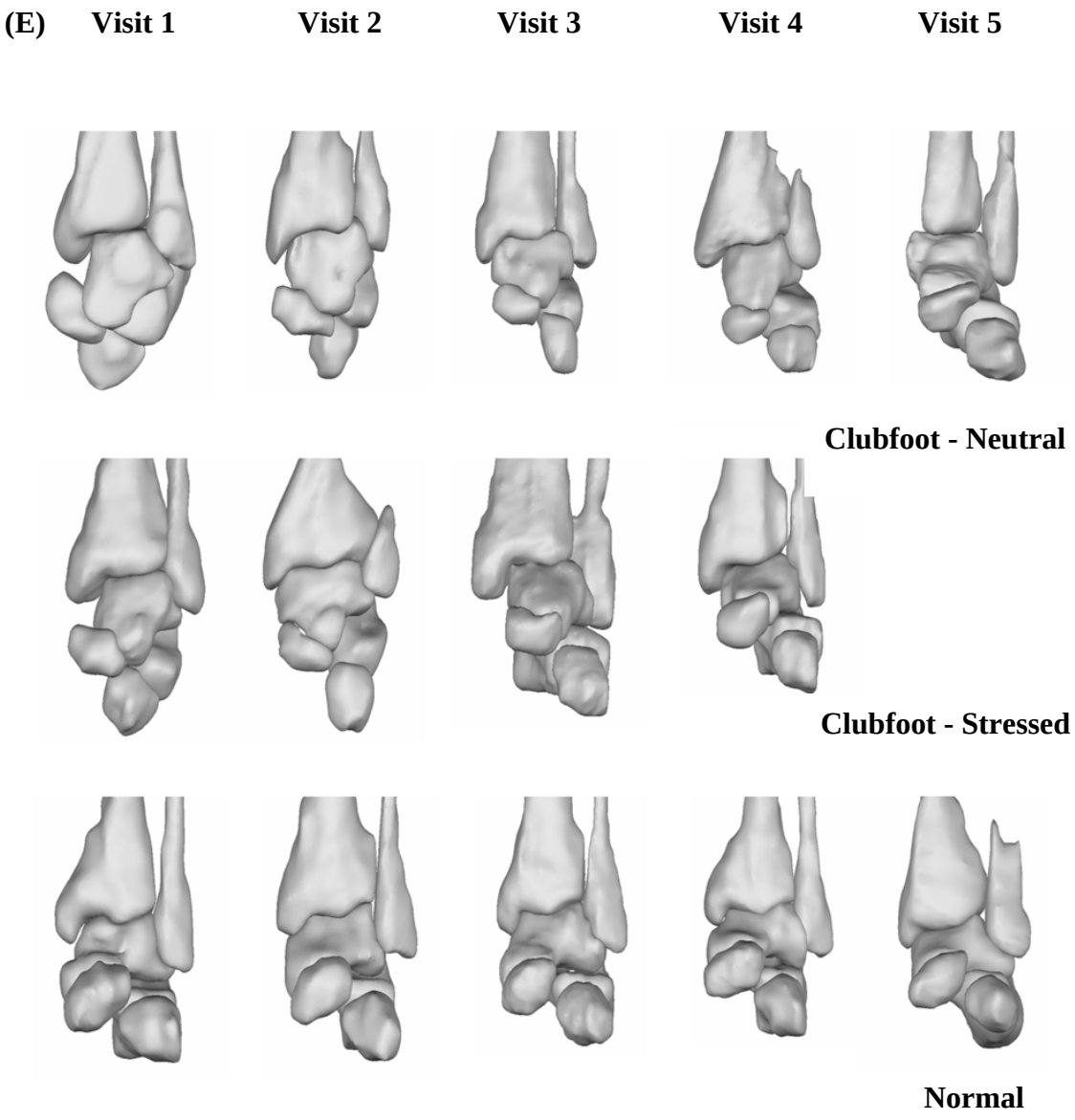

Figure 6.8 (continued).

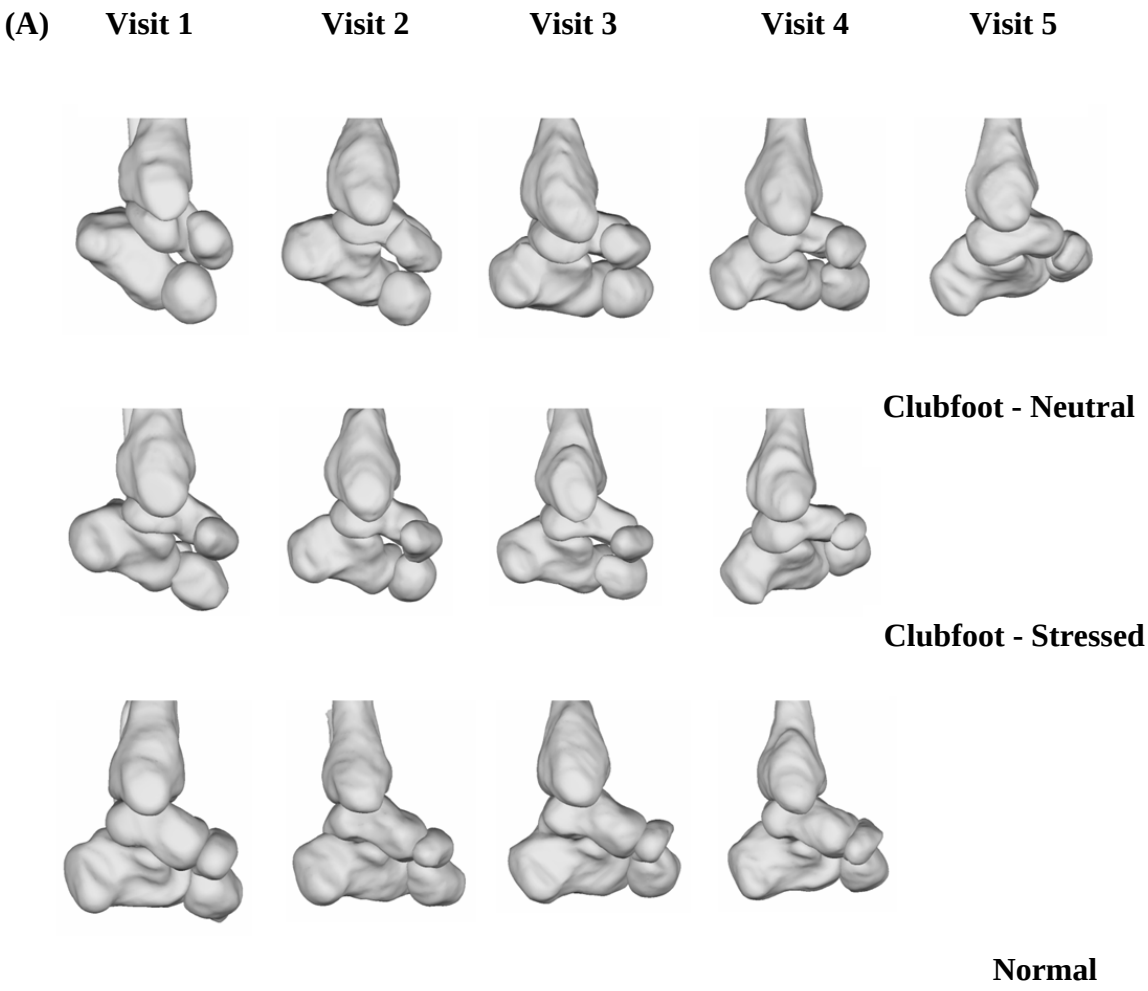

Figure 6.9. Sagittal views of patients' reconstructed bone geometries: (A) S1, (B) L1, (C) K1, (D) E2, (E) T1.

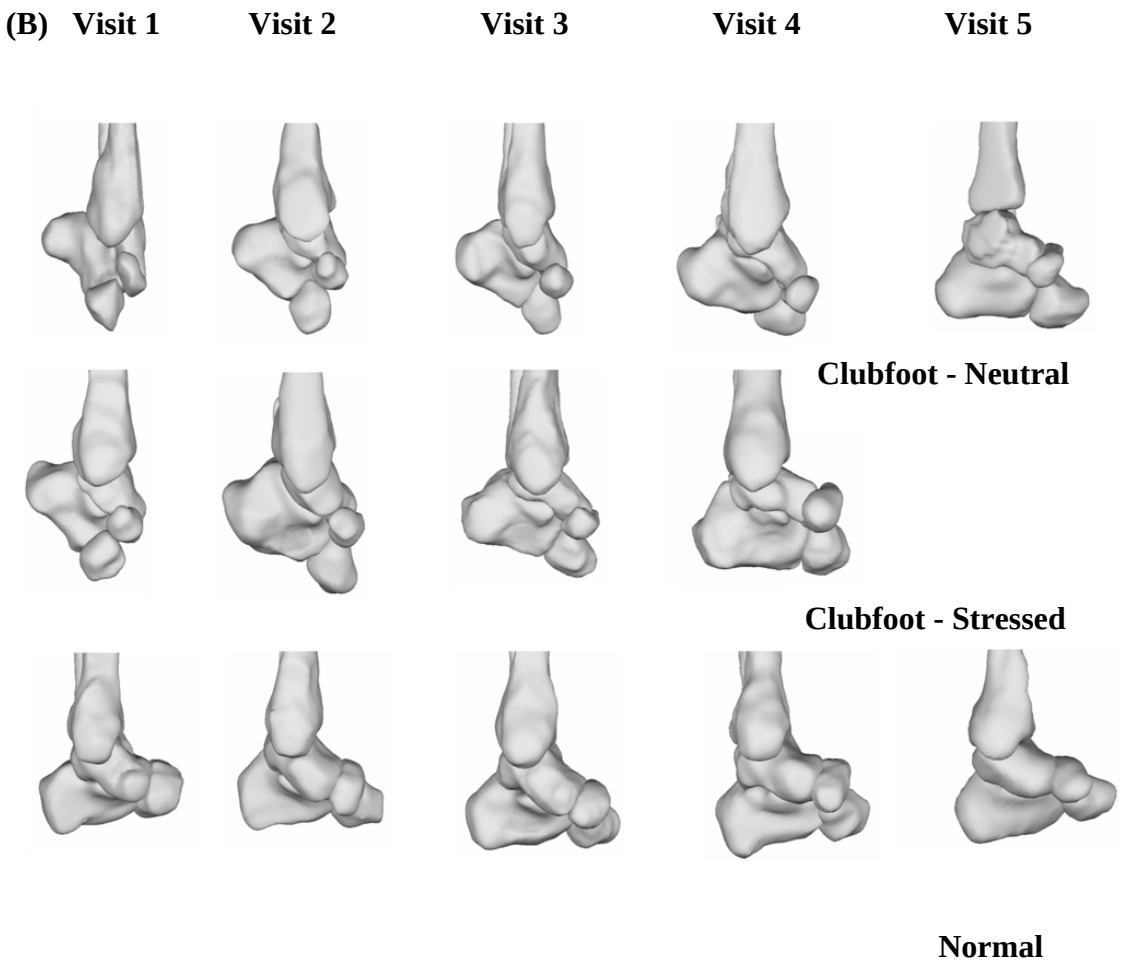

Figure 6.9 (continued).

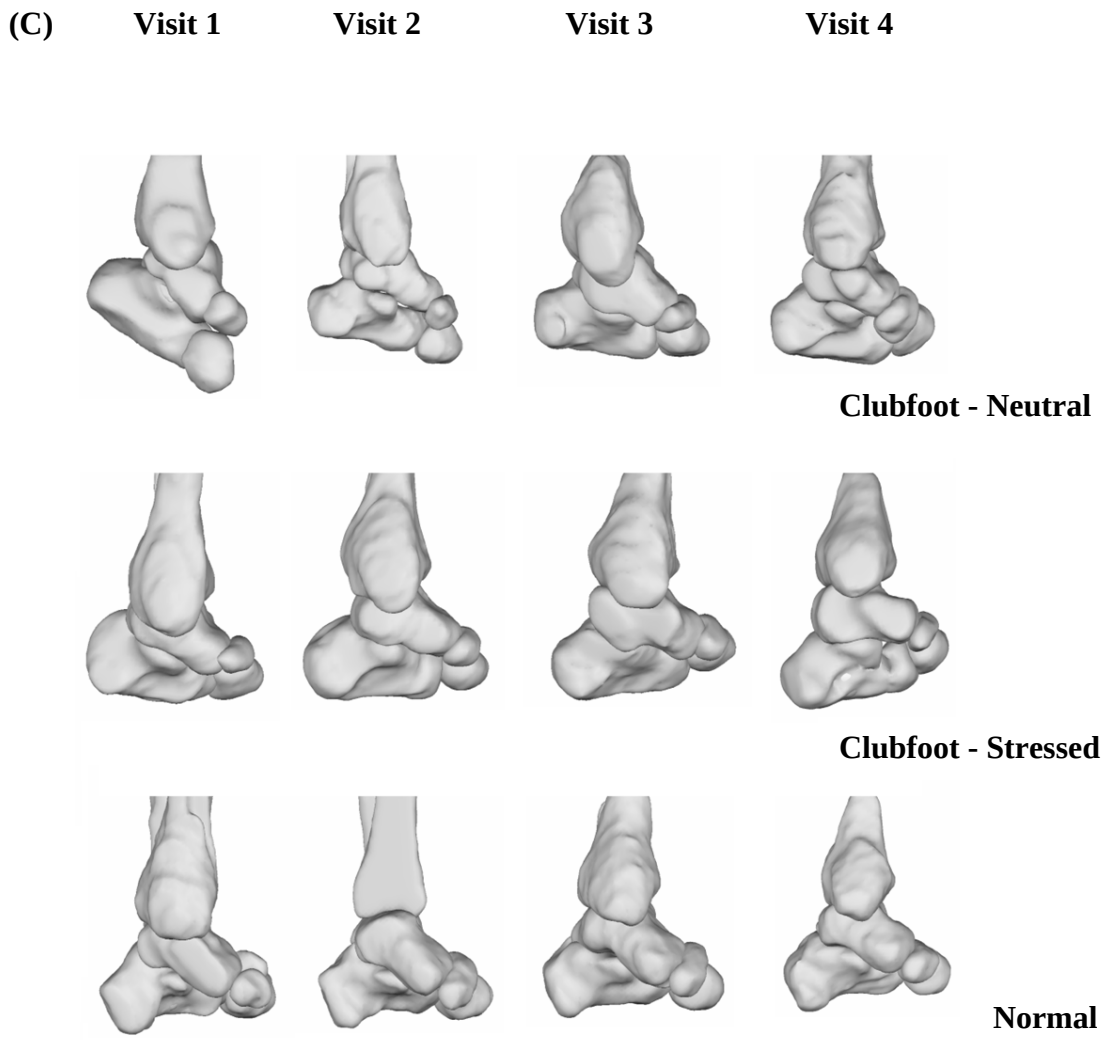

Figure 6.9 (continued).

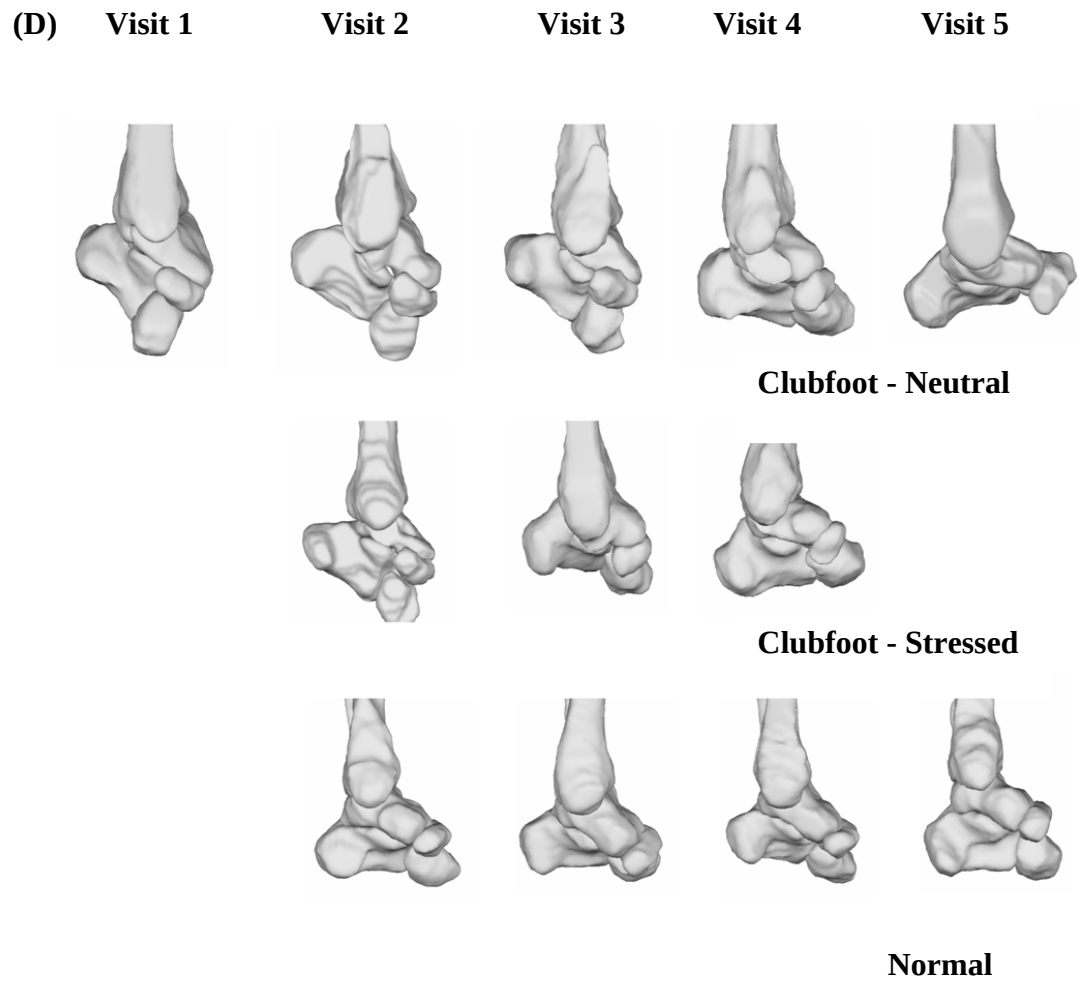

Figure 6.9 (continued).

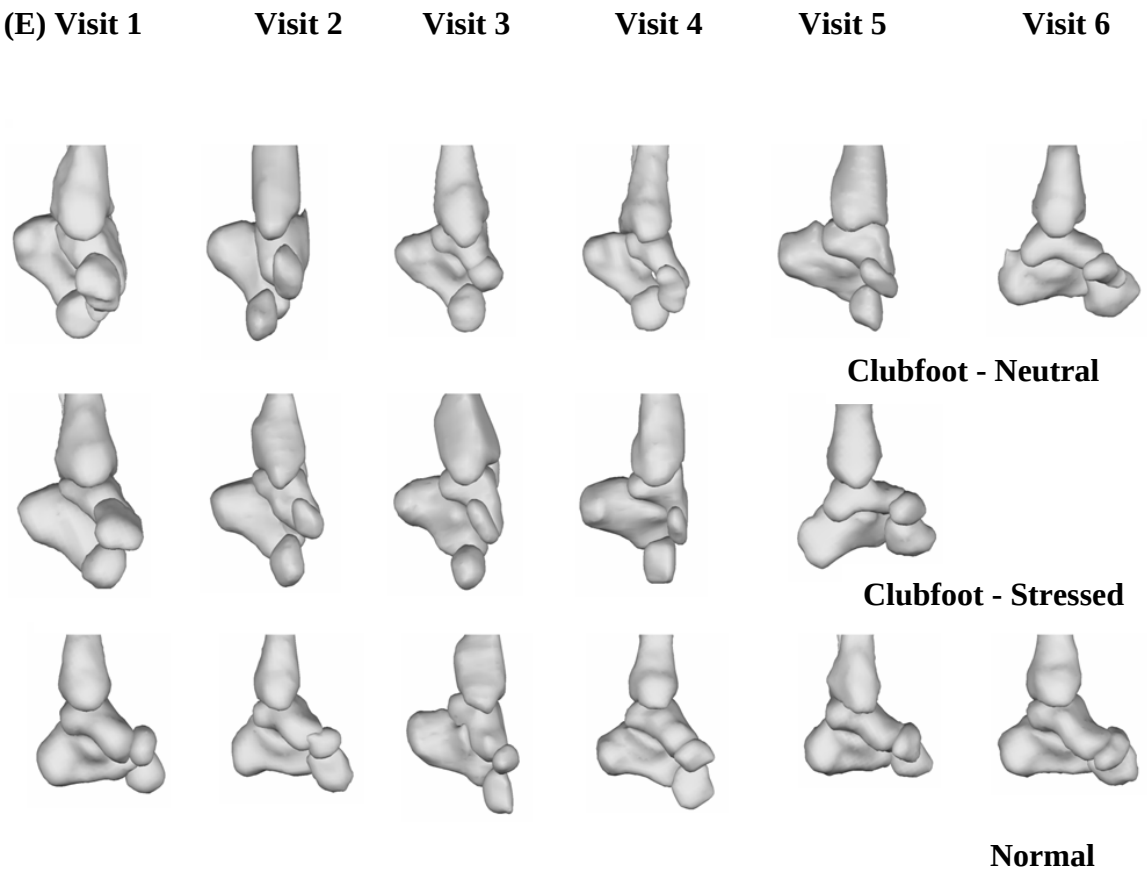

Figure 6.9 (continued).

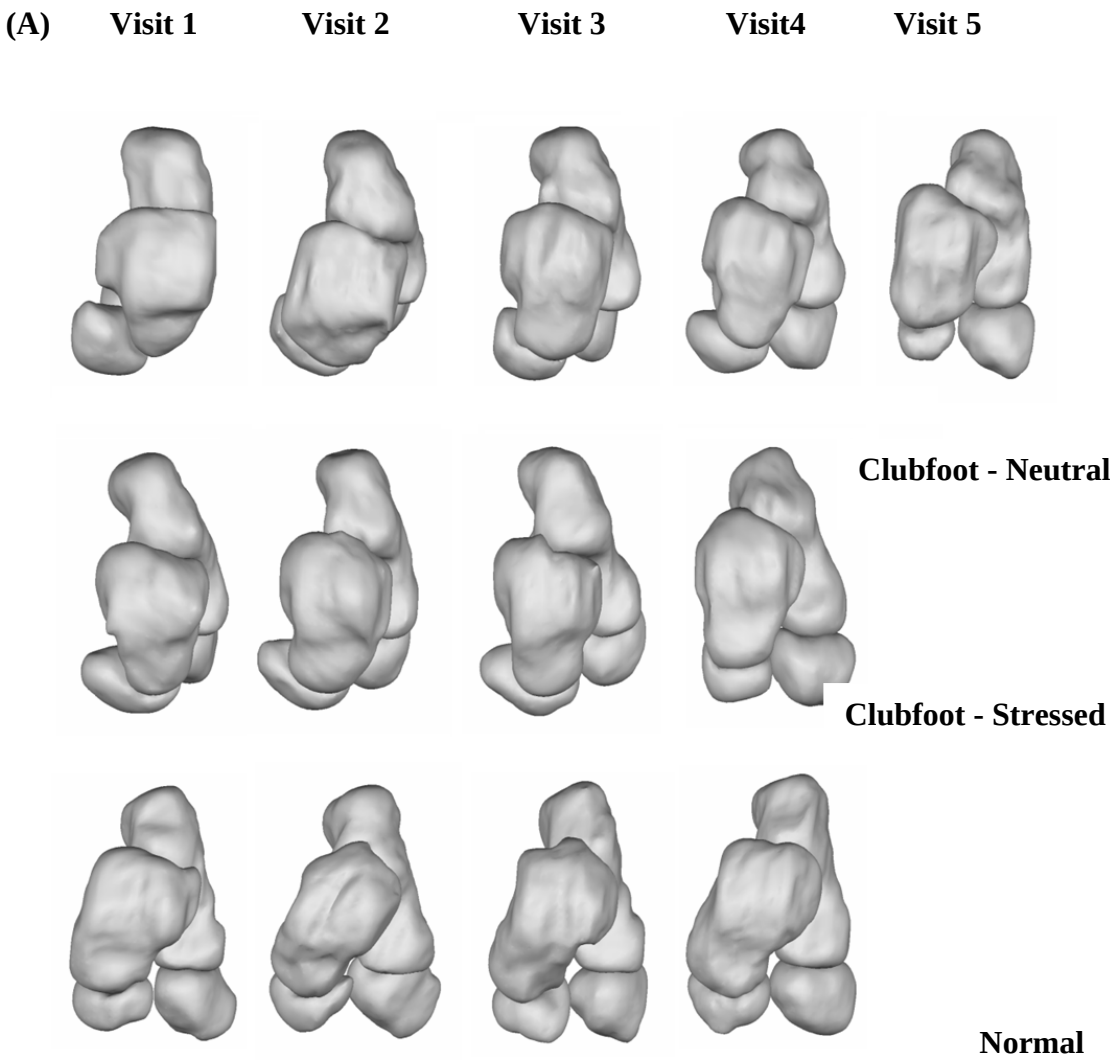

Figure 6.10. Axial views of patients' reconstructed bone geometries: (A) S1, (B) L1, (C) K1, (D) E2, (E) T1.

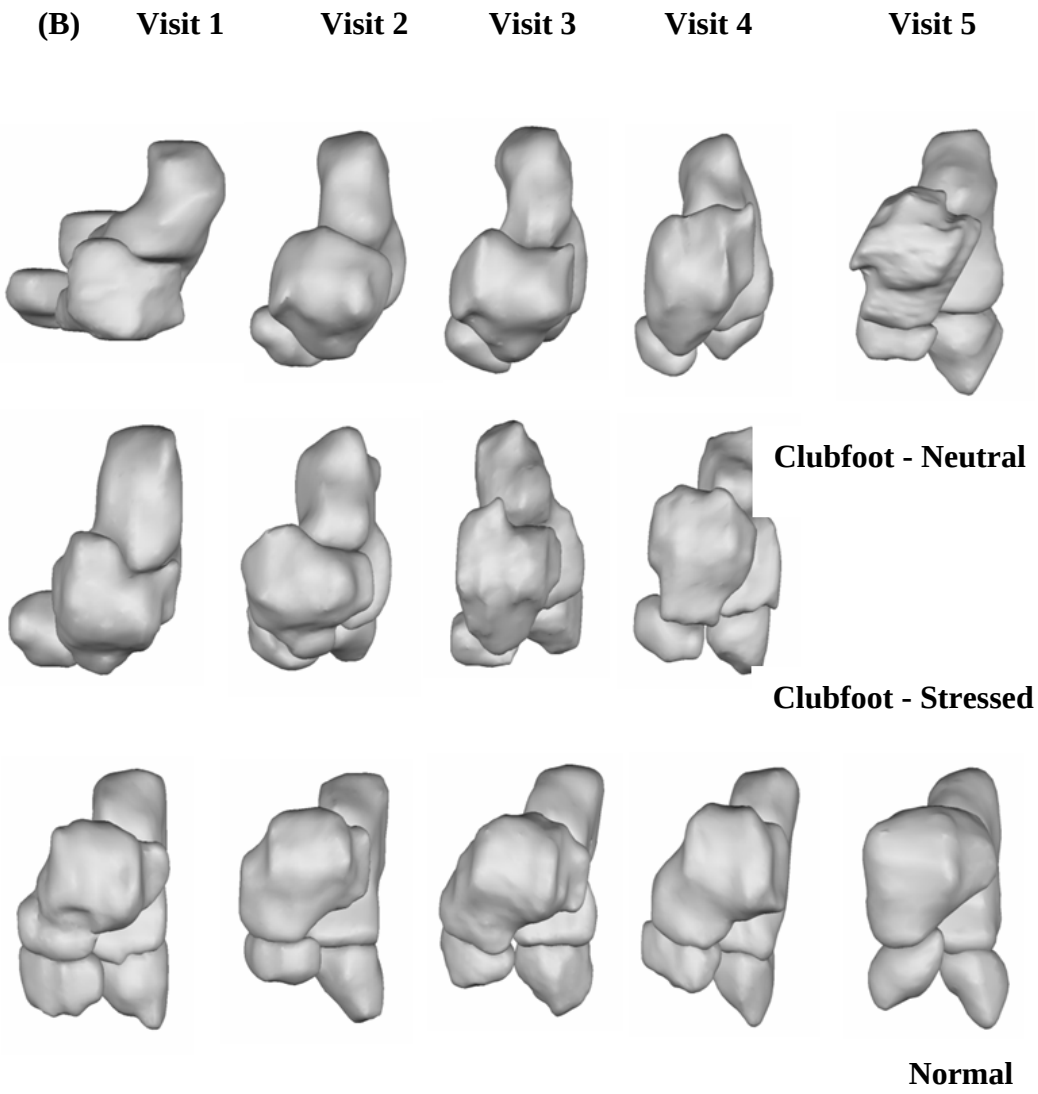

Figure 6.10. (continued).

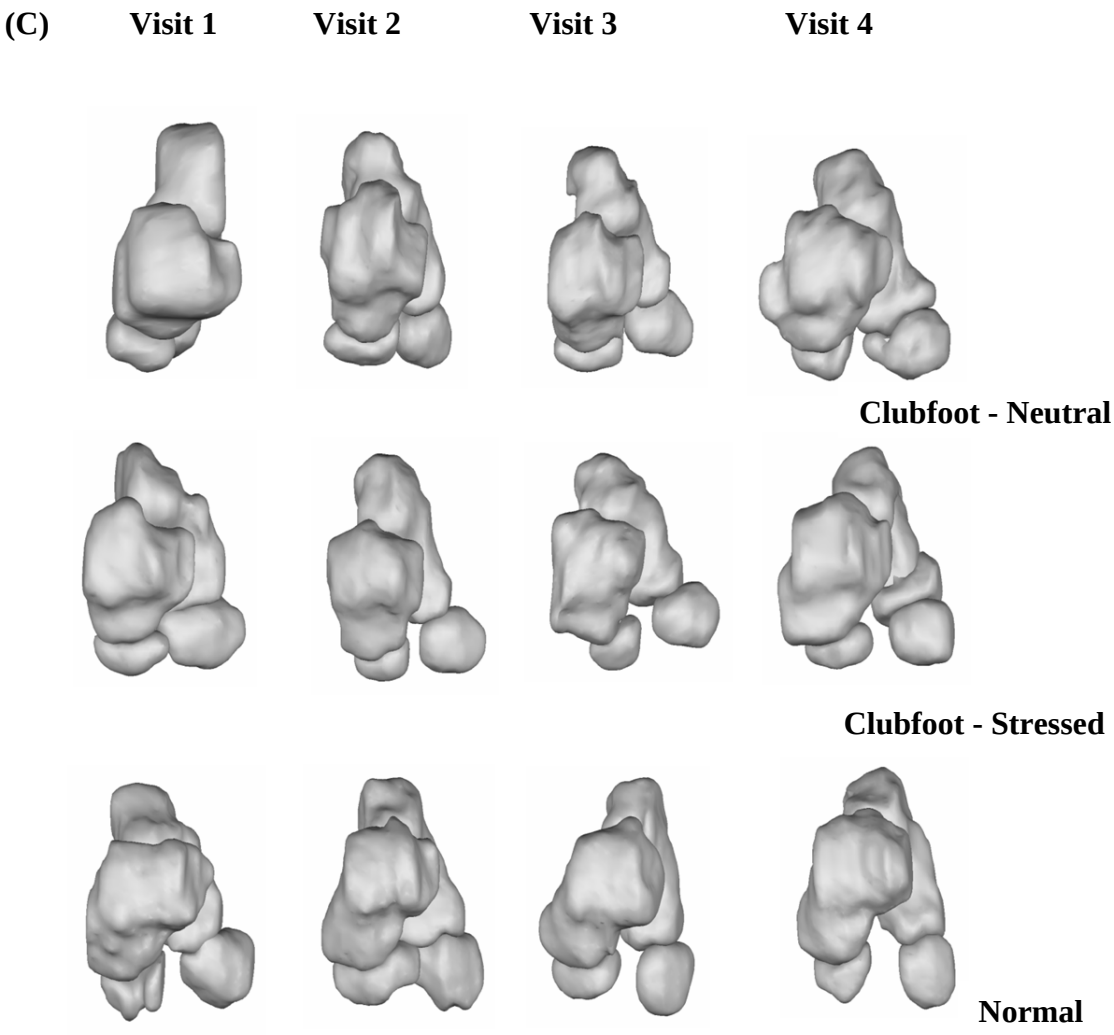

Figure 6.10 (continued).

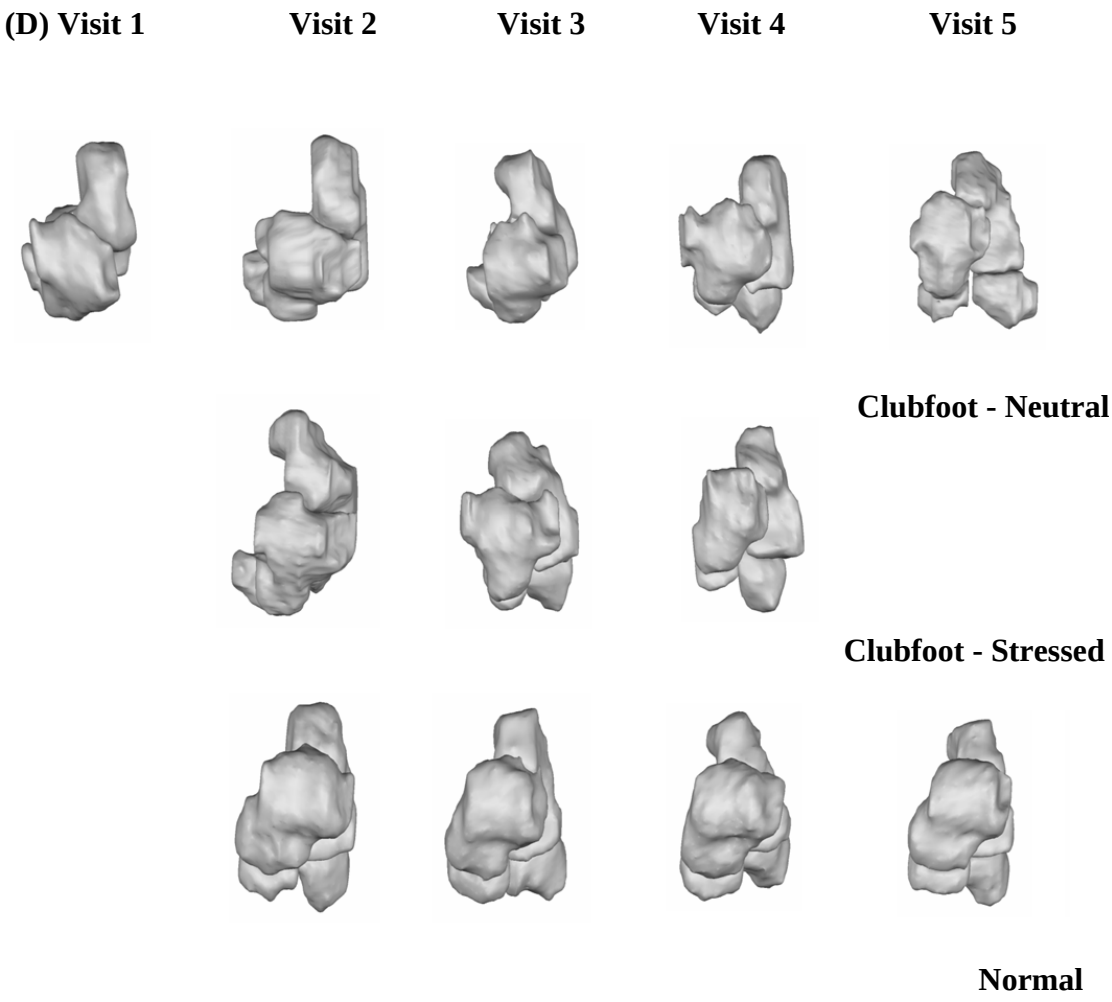

Figure 6.10 (continued).

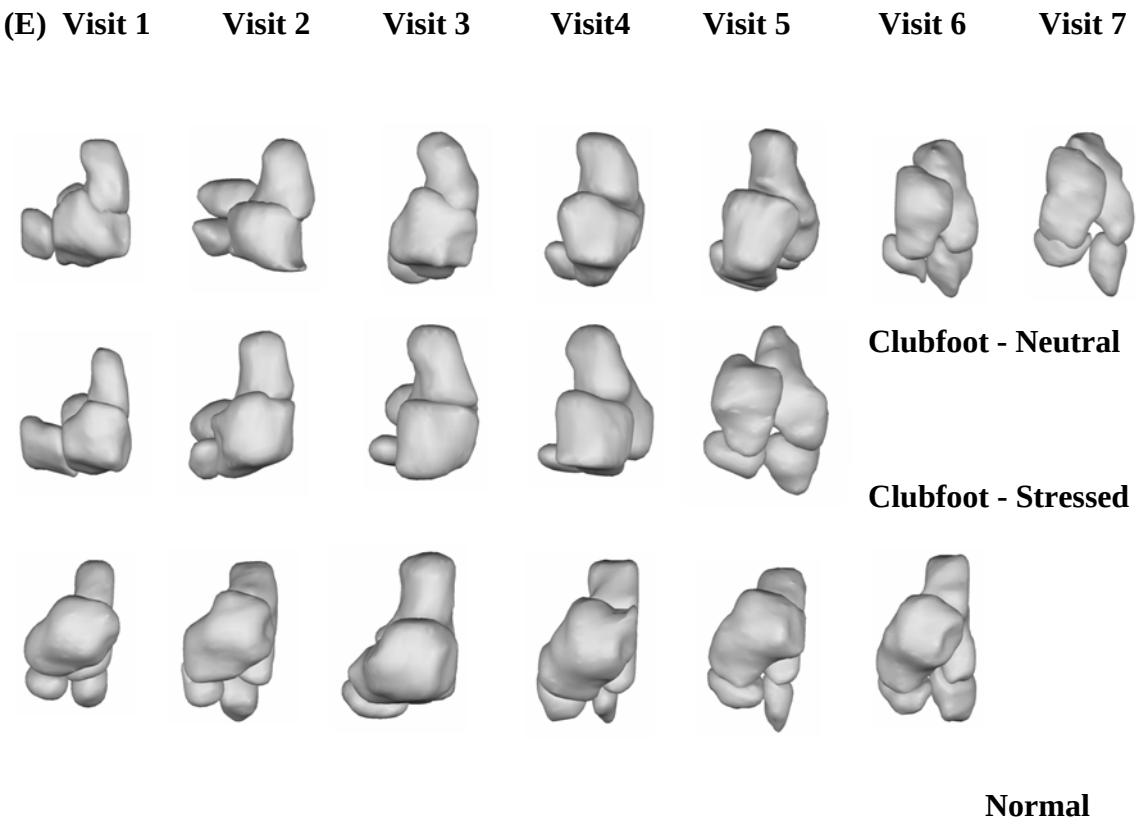

Figure 6.10 (continued).

Table 6.2. Correlation and regression analysis of variation of talus volumetric variables with the number of days counted from the first treatment session (β_0: intercept, β_1: slope; r: Pearson correlation coefficient).

Patient: S1	$\boldsymbol{\beta_0}$	$\boldsymbol{\beta_1}$	$\boldsymbol{R^2}$	r	p (1-tailed)
Clubfoot ON	1.017	0.004	0.920	.959	0.005
Clubfoot DO	1.0440	0.006	0.913	.955	0.006
Clubfoot/Normal DO	0.607	0.003	0.978	.989	0.005

Patient: L1	$\boldsymbol{\beta_0}$	$\boldsymbol{\beta_1}$	$\boldsymbol{R^2}$	r	p (1-tailed)
Normal ON	0.992	0.005	0.928	.963	.004
Clubfoot ANL	1.132	0.014	.742	.862	.030
Normal ANL	1.048	0.011	.772	.878	.025

Patient: K1	$\boldsymbol{\beta_0}$	$\boldsymbol{\beta_1}$	$\boldsymbol{R^2}$	r	p (1-tailed)
Clubfoot ON	1.013	0.05	0.943	.971	.014
Clubfoot ANL	1.024	0.008	0.656	.810	.095
Clubfoot DO	0.996	0.036	0.977	.988	.006
Clubfoot/Normal ON	0.455	0.016	0.664	.815	.092
Clubfoot/Normal DO	0.614	0.015	0.788	.888	.056

Patient: E2	$\boldsymbol{\beta_0}$	$\boldsymbol{\beta_1}$	$\boldsymbol{R^2}$	r	p (1-tailed)
Clubfoot ON	1.162	0.026	0.744	.862	.030
Normal ON	1.063	0.012	0.994	.997	.002
Normal ANL	1.030	0.006	0.982	.991	.005
Clubfoot DO	1.199	0.023	0.801	.895	.020
Normal DO	1.039	0.005	0.890	.944	.028
Clubfoot/Normal DO	0.636	0.003	0.562	.750	.125

Patient: T1	$\boldsymbol{\beta_0}$	$\boldsymbol{\beta_1}$	$\boldsymbol{R^2}$	r	p (1-tailed)
Clubfoot ON	0.873	0.007	0.637	.798	.029
Normal ANL	0.965	0.004	0.344	.587	.110
Clubfoot DO	0.863	0.012	0.649	.805	.027
Clubfoot/Normal ANL	0.787	-0.004	0.522	-.722	.052
Clubfoot/Normal DO	0.450	0.006	0.689	.830	.020

Table 6.2 (continued).

Patient: B1	$\boldsymbol{\beta_0}$	$\boldsymbol{\beta_1}$	$\boldsymbol{R^2}$	r	p (1-tailed)
Clubfoot ON	0.911	0.018	0.963	.981	.009
Normal ON	0.920	0.014	0.976	.976	.002
Clubfoot ANL	1.101	0.007	0.470	.686	.101
Normal ANL	1.074	0.009	0.667	.817	.046
Clubfoot DO	0.935	0.004	0.645	.803	.099
Clubfoot/Normal ON	0.390	0.003	0.990	.995	.002
Clubfoot/Normal DO	0.570	0.003	0.564	.751	.124

* ON, ANL, and DO stand for ossific nucleus, anlage, and degree of ossification respectively and are normalized by the corresponding values at session 1.

Table 6.3. Correlation and regression analysis of variation of calcaneus volumetric variables with the number of days counted from the first treatment session (β_0: intercept, β_1: slope; r: Pearson correlation coefficient).

Patient: S1	$\boldsymbol{\beta_0}$	$\boldsymbol{\beta_1}$	$\boldsymbol{R^2}$	r	p (1-tailed)
Clubfoot ON	0.987	0.008	0.962	.981	.002
Clubfoot DO	0.903	0.005	0.653	.808	.049

Patient: L1	$\boldsymbol{\beta_0}$	$\boldsymbol{\beta_1}$	$\boldsymbol{R^2}$	r	p (1-tailed)
Clubfoot ON	0.942	0.007	0.640	.800	.052
Clubfoot ANL	0.999	0.006	0.593	.770	.064
Normal ANL	0.952	0.009	0.911	.954	.006
Normal DO	0.980	-0.005	0.769	-.877	.025
Clubfoot/Normal ON	0.788	0.003	0.600	.775	.062
Clubfoot/Normal DO	0.986	0.007	0.840	.916	.014

Patient: K1	$\boldsymbol{\beta_0}$	$\boldsymbol{\beta_1}$	$\boldsymbol{R^2}$	r	p (1-tailed)
Clubfoot ON	1.009	0.020	0.930	.964	.018
Normal ON	0.961	0.007	0.542	.736	.132
Clubfoot ANL	0.946	0.016	0.794	0.891	.054
Clubfoot/Normal ON	0.819	0.009	0.574	.757	.121
Clubfoot/Normal ANL	0.751	0.019	0.951	.975	.012

Patient: E2	$\boldsymbol{\beta_0}$	$\boldsymbol{\beta_1}$	$\boldsymbol{R^2}$	r	p (1-tailed)
Normal ON	1.023	0.005	0.684	.827	.087
Normal ANL	1.023	0.005	0.813	.902	.049

Patient: T1	$\boldsymbol{\beta_0}$	$\boldsymbol{\beta_1}$	$\boldsymbol{R^2}$	r	p (1-tailed)
Clubfoot ON	0.942	0.011	0.972	.986	.000
Normal ON	1.239	0.018	0.728	.853	.015
Clubfoot ANL	0.921	0.003	0.602	.776	.035
Normal ANL	1.025	0.004	0.561	.749	.043
Clubfoot DO	1.039	0.007	0.804	.897	.008
Normal DO	1.215	0.011	0.594	.771	.036

Table 6.3 (continued).

Patient: B1	$\boldsymbol{\beta_0}$	$\boldsymbol{\beta_1}$	$\boldsymbol{R^2}$	r	p (1-tailed)
Clubfoot ON	0.905	0.020	0.977	.989	.001
Normal ON	0.908	0.013	0.899	.899	.019
Clubfoot ANL	0.944	0.007	0.676	.822	.022
Normal ANL	1.150	0.010	0.649	.805	.050
Clubfoot DO	0.948	0.010	0.931	.965	.004

* ON, ANL, and DO stand for ossific nucleus, anlage, and degree of ossification respectively and are normalized by the corresponding values at session 1.

Table 6.4. Correlation and regression analysis of variation of navicular volumetric variables with the number of days counted from the first treatment session (β_0: intercept, β_1: slope; r: Pearson correlation coefficient).

Patient: S1	$\boldsymbol{\beta_0}$	$\boldsymbol{\beta_1}$	$\boldsymbol{R^2}$	r	p (1-tailed)
Clubfoot/Normal ANL	1.135	-0.004	0.939	-.969	.016

Patient: K1	$\boldsymbol{\beta_0}$	$\boldsymbol{\beta_1}$	$\boldsymbol{R^2}$	r	p (1-tailed)
Clubfoot ANL	0.930	0.043	0.968	.984	.008
Clubfoot/Normal ANL	0.438	0.046	0.833	.913	.044

Patient: E2	$\boldsymbol{\beta_0}$	$\boldsymbol{\beta_1}$	$\boldsymbol{R^2}$	r	p (1-tailed)
Normal ANL	1.039	0.008	0.664	.815	.092
Clubfoot/Normal ANL	0.633	-0.004	0.637	-.798	.101

Patient: T1	$\boldsymbol{\beta_0}$	$\boldsymbol{\beta_1}$	$\boldsymbol{R^2}$	r	p (1-tailed)
Normal ANL	0.794	0.008	0.538	.734	.048
Clubfoot/Normal ANL	1.163	-0.013	0.825	-.908	.016

Patient: B1	$\boldsymbol{\beta_0}$	$\boldsymbol{\beta_1}$	$\boldsymbol{R^2}$	r	p (1-tailed)
Clubfoot/Normal ANL	0.850	-0.007	0.400	-.632	.126

* ON, ANL, and DO stand for ossific nucleus, anlage, and degree of ossification respectively and are normalized by the corresponding values at session 1.

Table 6.5. Correlation and regression analysis of variation of cuboid volumetric variables with the number of days counted from the first treatment session (β_0: intercept, β_1: slope; r: Pearson correlation coefficient).

Patient: S1	$\boldsymbol{\beta_0}$	$\boldsymbol{\beta_1}$	$\boldsymbol{R^2}$	r	p (1-tailed)
Clubfoot ON	1.036	0.012	0.964	.982	.001
Clubfoot DO	1.100	0.009	0.662	.814	.047
Clubfoot/Normal ON	0.476	0.003	0.849	.922	.039

Patient: L1	$\boldsymbol{\beta_0}$	$\boldsymbol{\beta_1}$	$\boldsymbol{R^2}$	r	p (1-tailed)
Clubfoot ON	0.120	0.896	0.937	.968	.003
Normal ON	7.260	0.679	0.433	.658	.114
Clubfoot ANL	0.814	0.014	0.638	.799	.053
Clubfoot DO	5.566	0.583	0.637	.798	.101
Normal DO	7.620	0.727	0.431	.657	.114
Clubfoot/Normal ANL	0.626	0.012	0.728	.853	.033

Patient: K1	$\boldsymbol{\beta_0}$	$\boldsymbol{\beta_1}$	$\boldsymbol{R^2}$	r	p (1-tailed)
Clubfoot ON	1.024	0.098	0.851	.923	.039
Normal ON	0.801	0.036	0.689	.830	.085
Clubfoot ANL	0.959	0.021	0.973	.987	.007
Clubfoot DO	1.102	0.060	0.645	.803	.098
Normal DO	0.718	0.095	0.921	.960	.020
Clubfoot/Normal ANL	0.476	0.038	0.981	.991	.005

Patient: E2	$\boldsymbol{\beta_0}$	$\boldsymbol{\beta_1}$	$\boldsymbol{R^2}$	r	p (1-tailed)
Clubfoot ON	-1.330	0.500	0.905	.951	.006
Normal ON	0.985	0.020	0.993	.997	.002
Clubfoot ANL	0.842	0.008	0.391	.625	.130
Clubfoot DO	-0.770	0.410	0.920	.959	.005
Normal DO	0.997	0.013	0.898	.948	.026
Clubfoot/Normal ON	0.063	0.014	0.785	.886	.057
Clubfoot/Normal ANL	0.568	0.006	0.541	.736	.132
Clubfoot/Normal DO	0.099	0.018	0.843	.918	.041

Patient: T1	$\boldsymbol{\beta_0}$	$\boldsymbol{\beta_1}$	$\boldsymbol{R^2}$	r	p (1-tailed)
Clubfoot ANL	0.754	0.012	0.481	.694	.063
Normal ANL	0.897	0.007	0.288	.537	.136

Table 6.5 (continued).

Patient: B1	β_0	β_1	R^2	r	p (1-tailed)
Clubfoot ON	-1.077	0.445	0.942	.965	.004
Normal ON	0.491	0.167	0.994	.991	.001
Clubfoot ANL	0.881	0.006	0.523	.723	.084
Normal ANL	0.970	0.007	0.400	.633	.089
Clubfoot DO	-0.072	0.297	0.972	.984	.001
Normal DO	0.430	0.132	0.976	.982	.001
Clubfoot/Normal ON	0.085	0.011	0.795	.891	.021
Clubfoot/Normal DO	0.155	0.013	0.692	.832	.040

* ON, ANL, and DO stand for ossific nucleus, anlage, and degree of ossification respectively and are normalized by the corresponding values at session 1. B1 did not have an ossific nucleus in the first session and data was normalized to the

Table 6.6. Growth regression models. Results of correlation analysis between volumetric parameters and age as conducted for all patients simultaneously (Right; r: Pearson correlation coefficient), and linear regression coefficients relating the former to the latter (Left; β_0: intercept, β_1: slope).

TALUS	β_0	β_1	R^2	r	p (1-tailed)
Clubfoot ON	55.718	3.345	0.472	.760	.000
Normal ON	224.571	4.855	0.584	.764	.000
Clubfoot ANL	1161.929	13.738	0.504	.710	.000
Normal ANL	1904.894	15.022	0.580	.762	.000
Clubfoot DO	0.075	0.001	0.224	.653	.004
Normal DO	0.138	0.001	0.269	.519	.002
Clubfoot/Normal ON	0.353	0.002	0.174	.417	.015
Clubfoot/Normal DO	0.540	0.002	0.176	.419	.015

CALCANEUS	β_0	β_1	R^2	r	p (1-tailed)
Clubfoot ON	248.933	9.244	0.749	.866	.000
Normal ON	408.660	7.902	0.573	.757	.000
Clubfoot ANL	1446.396	18.950	0.588	.767	.000
Normal ANL	1990.280	18.224	0.491	.700	.000
Clubfoot DO	0.231	0.001	0.484	.696	.000
Normal DO	0.236	0.001	0.202	.450	.008

NAVICULAR	β_0	β_1	R^2	r	p (1-tailed)
Clubfoot ANL	169.701	3.772	0.466	.683	.000
Normal ANL	387.746	2.423	0.296	.544	.001
Clubfoot/Normal ANL	0.598	0.003	0.097	.312	.057

Table 6.6 (continued).

CUBOID	β_0	β_1	R^2	r	p (1-tailed)
Clubfoot ON	-43.394	1.886	0.923	.960	.000
Normal ON	-21.917	2.348	0.762	.873	.000
Clubfoot ANL	357.283	5.103	0.541	.736	.000
Normal ANL	536.615	5.292	0.348	.590	.001
Clubfoot DO	-0.018	0.002	0.731	.855	.000
Normal DO	0.026	0.002	0.531	.729	.000
Clubfoot/Normal ON	0.302	0.003	0.101	.318	.080

* ON, ANL, and DO stand for ossific nucleus, anlage, and degree of ossification respectively, and are absolute values (not normalized).

Table 6.7. Comparison, between normal and clubfoot sides, of rates of change in the ossific nucleus size for individual patients. Results represent second coefficients (slopes) of the regression models.

		Talus		Calcaneus		Cuboid	
Patient	**Age**	**Normal**	**Clubfoot**	**Normal**	**Clubfoot**	**Normal**	**Clubfoot**
S1	88	0.000	0.004	0.000	0.008	0.001	0.012
L1	26	0.005	0.009	0.003	0.007	0.679	0.896
K1	43	0.008	0.050	0.007	0.02	0.036	0.098
E2	32	0.012	0.026	0.005	0.004	0.020	0.500
T1	41	0.003	0.007	0.018	0.011	0.002	-
B1	12	0.018	0.024	0.017	0.025	0.208	0.525

* ON, ANL values are normalized over the corresponding values at session 1.

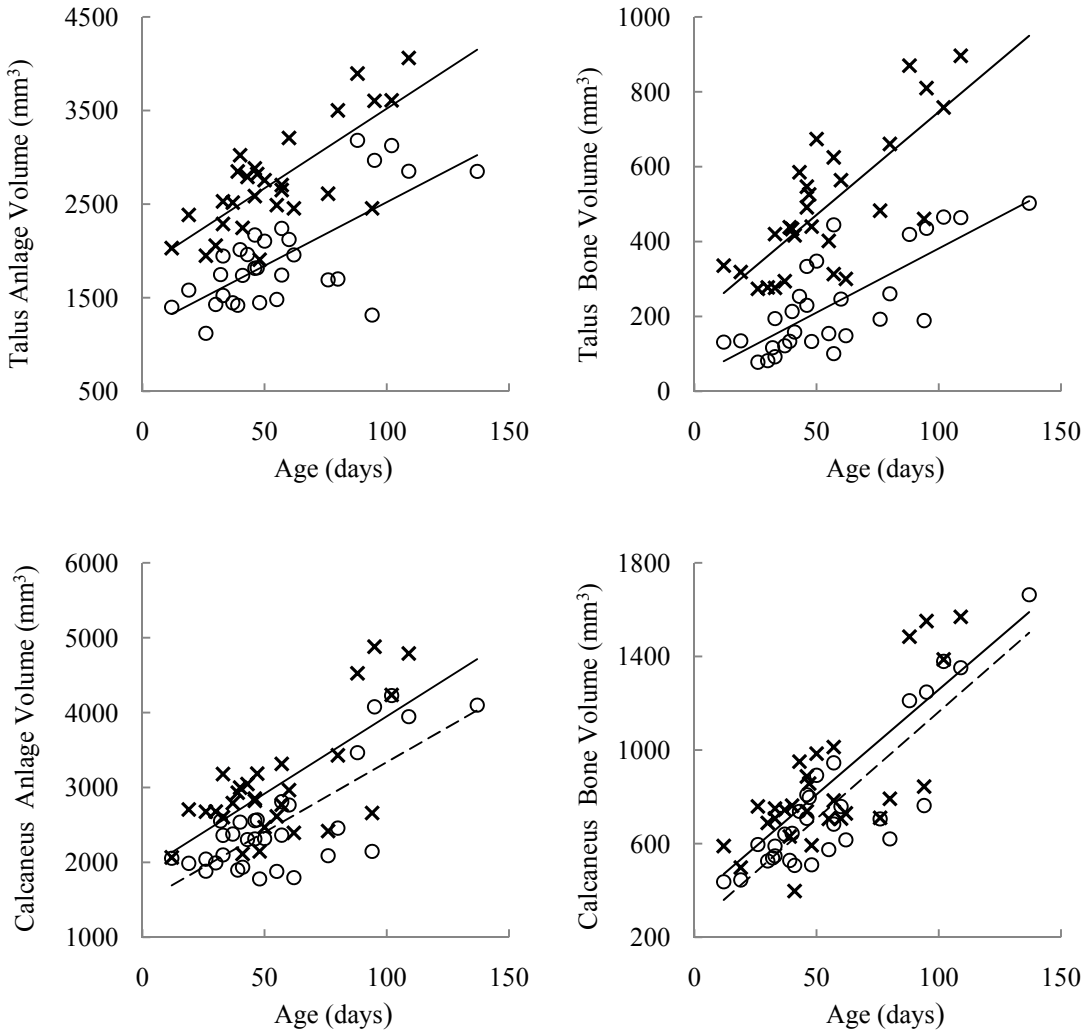

Figure 6.11. Volume data of all patients. Regression coefficients are given in Table 6.6. In all graphs hollow circles/dash line and cross markers/solid line represent clubfoot and normal values respectively.

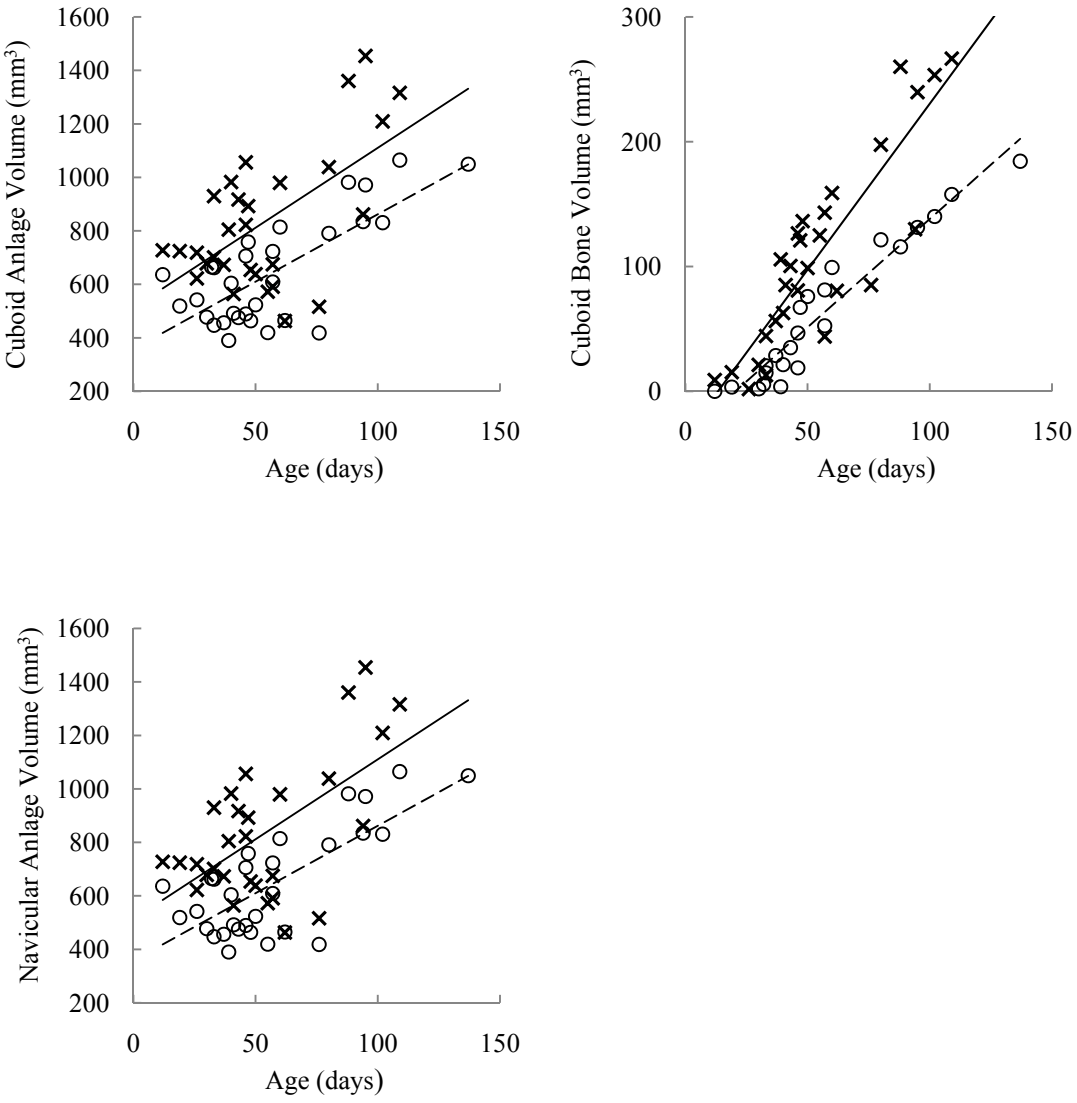

Figure 6.11 (continued).

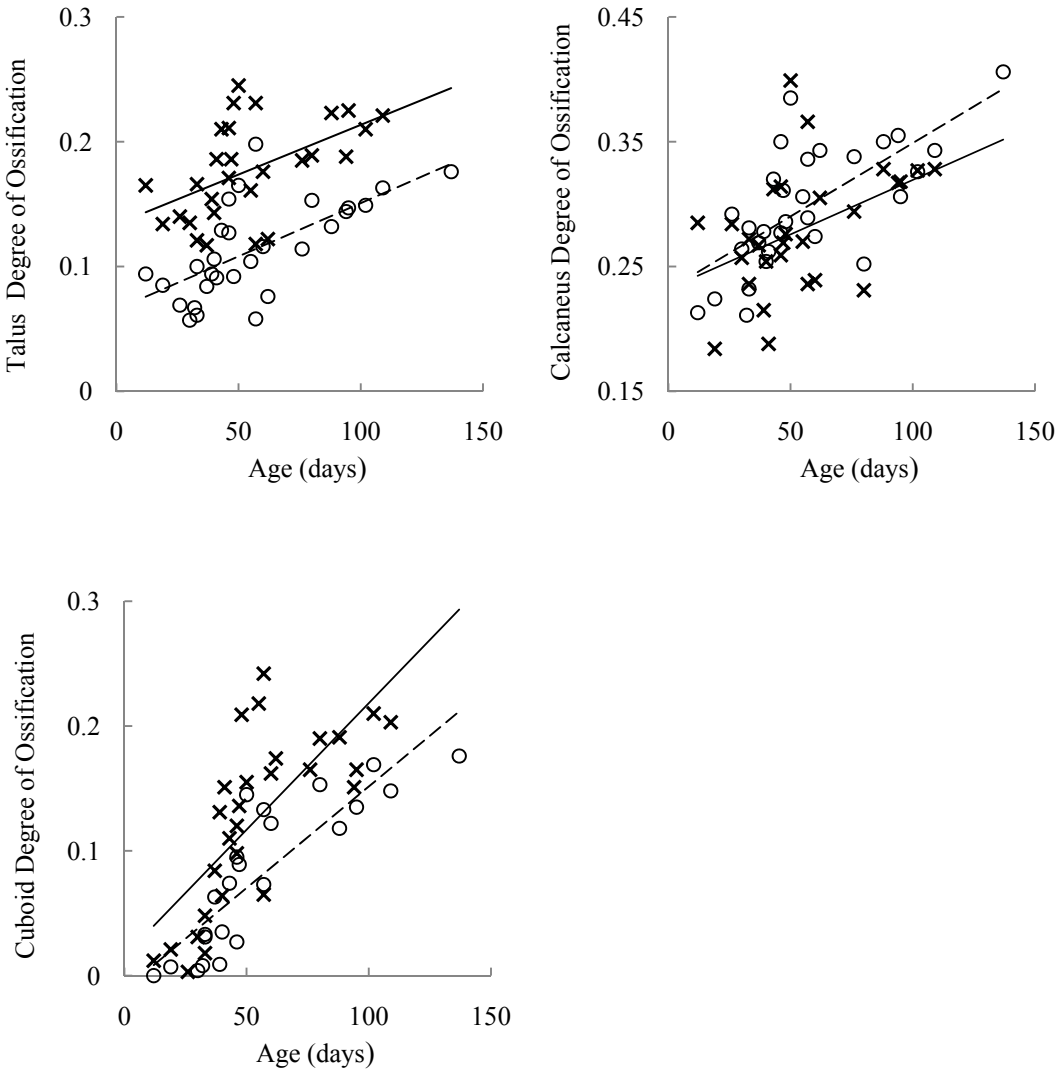

Figure 6.12. Values of degrees of ossification for all patients in three anlagen showing ossification. In all graphs hollow circles/dash line and cross markers/solid line represent clubfoot and normal values respectively.

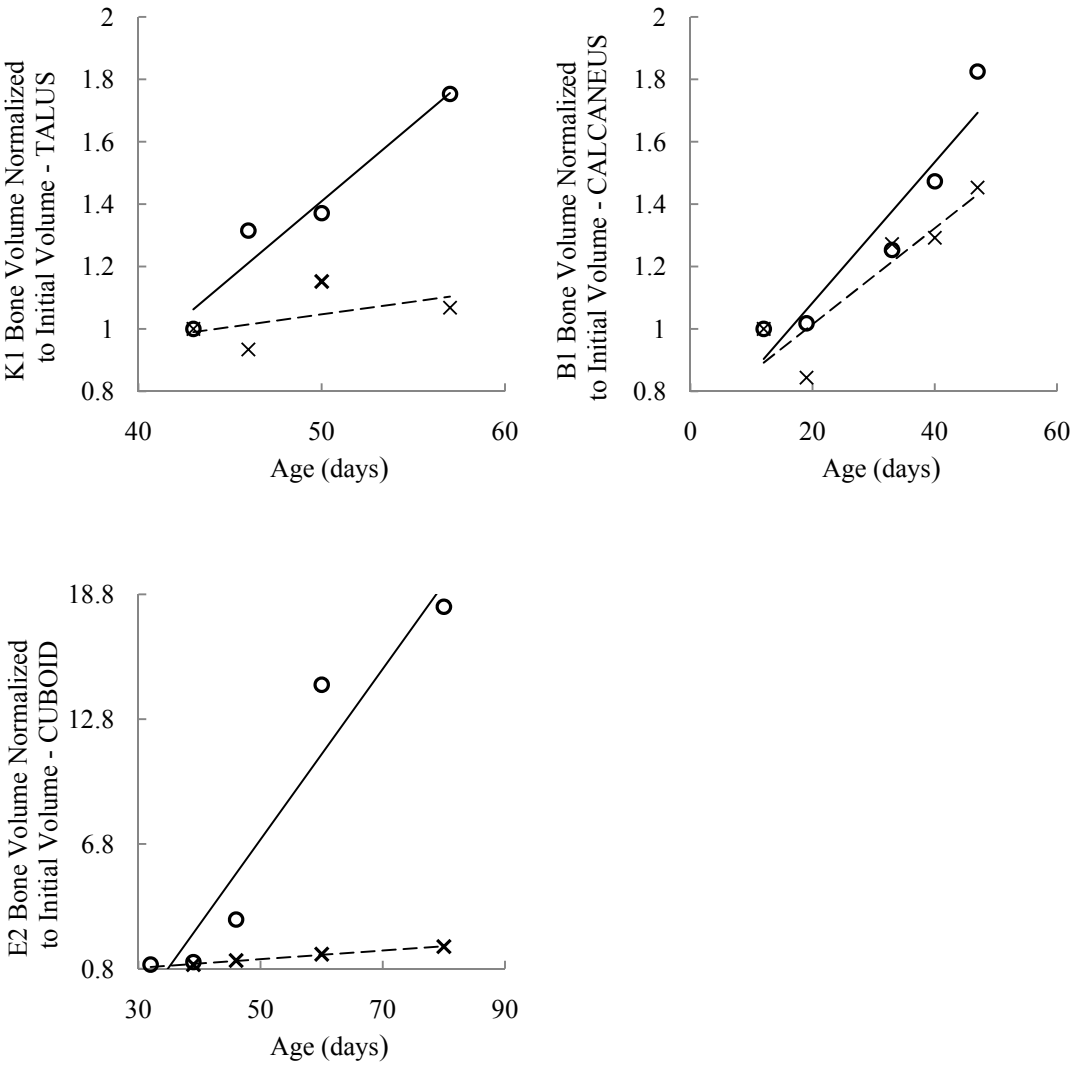

Figure 6.13. Normalized volumes of talus, calcaneus and cuboid ossific nuclei by the corresponding values at the beginning of treatment plotted against age for patients separately. In all graphs hollow circles/dash line and cross markers/solid line represent clubfoot and normal values respectively. The rate of ossification is clearly higher on the clubfoot side than the normal.

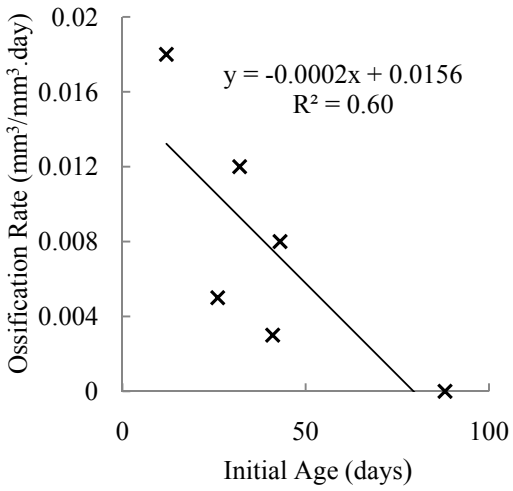

Figure 6.14. Rate of ossification in normal talus in all patients plotted against age of patient at the time treatment was initiated. A sharp decline is observed as age increases suggesting beginning treatment immediately upon diagnosis.

6.3.3 FE Analysis of Relationships Between Treatment-Induced Mechanical Quantities and Ossification

The correlation analysis performed on the data of all patients with the outliers removed, revealed an effect between the volumetric measure of bone deposition (volume of bone added on the surface) between each two sessions, and the strain energy density ($r = 0.749$, $p = 0.013$), fluid volume ratio ($r = 0.750$, $p = 0.013$), and the magnitude of the fluid velocity ($r = 0.752$, $p = 0.013$) when the UMAT model was utilized. When the linear elastic assumption was used for the extracellular matrix, significant correlations were found between the volumetric measure of bone deposition and the fluid velocity magnitude only ($r = 0.627$, $p = 0.05$). No significant correlations were observed for the rest of the mechanical quantities. Tables 6.8, 6.9, and 6.10 summarize the results of this

section. Figure 6.15 shows the pressure stress distribution in the talus as a result of manipulation and casting. The Pearson correlation coefficient and the significance levels calculated between the two measures of bone deposition, as described in Chapter 5, were r = 0.874 and p = 0.001 respectively.

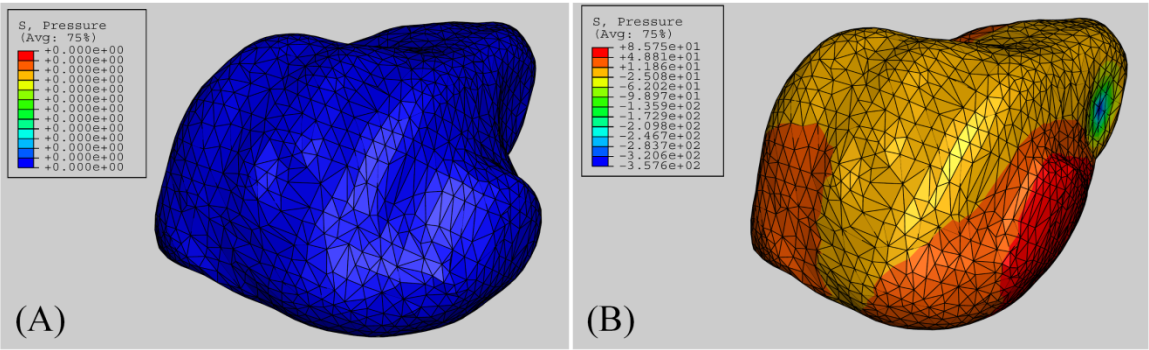

Figure 6.15. Pressure stress distribution (kPa) in the talus as a result of manipulation and casting.

Table 6.8. Regression analysis of normalized volumetric bone deposition versus mechanical quantities – matrix represented with UMAT (β_0: intercept, β_1: slope).

	Strain Energy Density GJ/m^3	Fluid Volume Ratio	Fluid Velocity Magnitude (mm/s)
β_0	-0.236	-0.223	-0.136
β_1	0.003	0.021	95.275
R^2	0.561	0.562	0.565

Table 6.9. Regression analysis of normalized volumetric bone deposition versus mechanical quantities –matrix represented as linear elastic (β_0: intercept, β_1: slope).

	Fluid Velocity Magnitude (mm/s)
β_0	-0.103
β_1	93.746
R^2	0.393

Table 6.10. Regression analysis of bone deposition in the normal direction (mm) versus normalized volumetric bone deposition (mm^3/mm^3); β_0: intercept, β_1: slope.

β_0	-0.144
β_1	1.038
R^2	0.764

CHAPTER 7. DISCUSSION

7.1 Discussion

7.1.1 Mechanical Properties of Fetal Talus

The stress relaxation behavior of fetal human talar cartilage anlage was investigated in this study in the confined and unconfined compression configurations. The extracted mechanical properties were different from adult articular cartilage properties and similar to those reported in a few studies of fetal and newborn articular cartilage [150-151]. The literature suggests large variability among the mechanical properties of articular cartilage, which may be in part due to different testing geometries, varying test sites, and different species. Similarities and differences between the biology and biochemistry of various species cartilages, regardless of the anatomic similarity between their sources, are important factors in explaining the differences in mechanical properties.

The biochemical composition and the ultrastructure of the extracellular matrix (see Chapter 3) together determine the resulting biomechanical properties of cartilage [152]. These properties have been mainly associated with the collagen network and glycosaminoglycan constituents (negatively charged chains attached to the core protein of PGs) of the extracellular matrix [153-154] which vary over time with development and also across anatomic sites and various species. The differences between our results for fetal developing cartilage and the literature values for adult or fetal articular cartilage of various species may be attributed to the same sources [11].

The increase in the collagen content with development has been reported in the literature [11, 150-151]. Although collagen network has been commonly believed to primarily contribute to the tensile properties of cartilage, its role in defining the compressive behavior has been highlighted more in recent studies [151, 155-163]. Paralleled with this growth in the collagen network, the equilibrium aggregate and Young's moduli (0.11 ± 0.04 and 0.06 ± 0.03 MPa) we found in the present study were an order of magnitude smaller than the literature values for adult articular cartilage.

There is a large variation in the literature in the values of Poisson's ratio from compression tests (0.0-0.48) [164] stemming from - to name a few - the use of non-standardized methods, specimen sources, and varying test configurations. The Poisson's ratio we observed is at the high range of reported values, among a few other studies [165-171]. One reason is that the Poisson's ratio obtained here is the intrinsic value. As fluid drains from the lateral surfaces, the total volume reduces and therefore the apparent Poisson's ratio is lower than the intrinsic Poisson's ratio of the matrix. Second, the collagen network primarily controls the Poisson's ratio [155]. The tested fetal cartilage anlage (mostly precursor to bone, not articular cartilage) is soft and its collagen network lacks the organized fibril arrangement and high cross-linking (governing the tensile behavior) present in adult articular cartilage, and thus has greater tendency for lateral expansion (e.g., in unconfined compression) which gives rise to higher Poisson's ratios. Supporting this notion is the inverse relationship between stiffness and Poisson's ratio [155].

The dry weight measurements (13.1 ± 1.8%) indicate the tissue is highly hydrated. Considering the cartilage matrix gets softer and more permeable as the water content increases [172-173], the low dry weight is consistent with the low stiffness and high permeability values found. The strain-dependent exponential representation of permeability yielded good model fits ($r^2 = 0.963 \pm 0.017$) to the experimental data. The results indicated lower permeability in the fetal tissue we tested as compared to adult talus permeability. Noting that hydraulic permeability is related to the matrix pore structure, and the pore size and connectivity, the effect of age on this parameter can be explained by augmentation of the collagen network size as development progresses. A more permeable matrix facilitates the fluid flow in the tissue.

In-depth studies are required to understand the reasons for differing properties between mature and developing cartilage. In brief, the relatively high Poisson's ratio, high permeability, low dry weight, and low stiffness moduli found herein are consistent with and confirm previous work on developing cartilage.

7.1.2 User Material Subroutine (UMAT)

An approach was presented for implementing the finite deformation biphasic theory for application in commercial FE codes by formulating a strain energy function [122] the corresponding material constants of which were obtained from the mechanical properties extracted using test configurations common for characterizing soft tissues. To determine the constants α_1 and α_2 of the strain energy function (α_0 is readily found in terms of H_{A0} and β), the constitutive equations were simplified independently to two different

narrower scenarios. First, the general stress equation was simplified to a 1-D compression configuration to represent the confined compression test while allowing for finite deformations. The second equation was obtained by reducing the problem to the scope of infinitesimal strains without constraining dimensionality. The results were then substituted into the general nonlinear elasticity equations.

The linear biphasic model assumes a constant stiffness and permeability, however, the permeability is dependent on the strain. The decrease in pore size with added deformation leads to an increase in the drag forces, and thus a decrease in permeability. The nonlinear biphasic model incorporates the strain-dependent permeability while the solid matrix behavior is assumed strain-independent. Local deformation under compression reduces the permeability causing a larger drag force on the fluid, which by itself increases the local deformation. Consequently, the nonlinear permeability effect can have an exaggerated effect unless the nonlinear elastic response of the solid phase is also accounted for [174]. The finite deformation accounts for both the nonlinear elasticity of the solid phase and the strain-dependent permeability.

In the confined compression simulation the UAMT showed more rapid relaxation in the early stages of the relaxation relative to the nonlinear biphasic model. This is similar to the results of Suh and Spilker on indentation analysis of articular cartilage under finite deformations [175] . The relaxation rate was similar for both models in the later relaxation periods. The equilibrium stresses predicted by the nonlinear biphasic model were larger than those given by the UMAT. To check if more relaxation would have occurred if given longer time, the same simulation was performed with 1000s and

2000s relaxation times rather than the 500s period used in the experiment (results not shown). The added amount of relaxation was not considerable. The UMAT had a larger peak-to-equilibrium stress similar to a previous study of an indentation test [175]. The confined compression simulation highlights the importance of a proper choice of material model for the tissue matrix. It is observed that at high strains (encountered physiologically), the nonlinear biphasic model fails to predict the peak stresses; neither does it provide a close fit to the stress relaxation phenomenon as observed in the experiment (Figure 6.5).

In the simulation of the unconfined compression configuration, the model exhibited a linear response. In the whole tissue structure experiment, the peak stress estimated by the nonlinear biphasic theory at the higher strain cycle was smaller than that of the experiment. Figure 6.7 demonstrates the total stress sensed by the load cell from the tissue under cantilever testing along with the results of simulation. The UMAT output agrees well with short and long term response of the tissue.

There are several approximations present in our model development. One is that the material model uses compressive properties of the tissue and is applied to predict the tissue response under general loading conditions. Generally, more attention has been paid in the literature to characterizing hyaline cartilage in compression than in tension, and the reports on compressive properties are more abundant. The assumption of isotropy is inherent in the biphasic theory; however, it has been shown that cartilage in fact exhibits an anisotropic response since the collagen fibrils cannot withstand compression as well as they resist tension. It seems a helpful next step to further develop the subroutine to

incorporate two sets of properties for tension and compression. This can create a discontinuity in the material stiffness matrix which is likely to cause convergence issues and thus requires special treatment. For the purposes of the current study, assumptions of homogeneity and isotropy are viable choices as the cartilage of interest is in a highly immature state lacking the structural organization that is present in the articular cartilage for instance.

Another approximation is the linearization of the Cauchy stress tensor to attain an additional equation to solve for the three constants of the strain energy function, and applying the resulting constants to a finite deformation problem. This is however a reasonable approximation since the results of the unconfined compression experiment were used to formulate this equation and it can be seen from our results that the stress-strain data were fitted very well with a straight line.

Similarity between the experiment and model prediction was satisfactory in both the cantilever testing of the whole tissue structure and reproduction of the confined and unconfined compression experiments on a tissue sample. Due to limitations in obtaining the fetal cadaveric materials, we were able to carry out one whole tissue test to verify the UMAT prediction against experiment.

The importance of coding the finite deformation biphasic theory in UMAT is manifested in FE studies of mechanobiology for instance: while the subroutine UHYPER can be sued to identify a strain energy density function for a hyperelastic material, it does not allow inclusion of adaptive phenomena. One such example is the study of endochondral ossification under the influence of mechanical stimulation. Such model will

involve two distinct areas of bone and cartilage, with the bone density increasing over time, with more and more turnover of cartilage areas to new bone which in turn gets more compact over time and changes its physical properties. Simultaneously, the cartilage region expands in size adding more cartilage that will ossify subsequently. Additionally, all of these processes are presumably dependent on the mechanical environment, which is a phenomenon that can be formulated as a growth and adaptation law in the UMAT into the framework of the finite deformation biphasic theory, once again highlighting the importance of inclusion of finite deformations.

In summary, the presented method provides a straightforward means to formulate the finite deformation biphasic theory for finite element analyses of soft tissue. The user material model developed accordingly was capable of predicting the instantaneous and long-term behavior of the cartilage anlage, and may be used to model soft tissues according to the finite deformation biphasic theory, and also to further incorporate other effects and details such as growth and adaptation.

7.1.3 The Clubfoot "Experiment"

The human infant clubfoot offers a unique human model to explore the relationship between external loading and anlagen adaptation. The clubfoot is normally small and the hindfoot bones are retarded in development. We have observed an increased rate in the growth of the ossific nuclei when clubfoot is treated by manipulation and casting. Thus, when unilateral, clubfoot treatment is a naturally occurring "experiment" which offers the opportunity to explore the normal development, the retarded development before treatment, and the acceleration of development with treatment. It requires none of the

sorts of internal perturbations associated with many animal experiments that might alter the biological responses independent of the manipulation and casting.

Our unique observations regarding shape changes of anlagen suggest that the forces produced during manipulation and casting create immediate shape changes of the soft anlagen. With the constant but gentle pressure on the anlagen and stretch on the ligaments inside the cast, the two tissues adapt over the period of casting. That is, the anlagen assume the new "deformed" but more "normal" shape, and the ligaments assume the new "stretched" but more "normal" length. During the next manipulation and casting, these phenomena repeat themselves until the cartilage has a more normal shape and the ligaments have a more normal length ultimately allowing for more normal positional relationships.

Ponseti advocated sequential correction of the cavus, adductus, and varus through manipulation and casting, and treating the equinus using a heel cord tenotomy [176]. Following this protocol, tenotomy was performed in the last visits in this study on all patients but two where a tenotomy was not assessed necessary. The persistent equinus is observed in the images before the heel cord release (Figure 6.9) followed by the improvement in the equinus deformity illustrated in the last image on the far right.

Assessment of the deformities of the skeletal system has been mostly done using measurements on plain radiographs, in the form of length measurements. More recently computed tomography (CT), magnetic resonance imaging (MRI) combined with image processing programs have been used for three-dimensional computer modeling and studying the clubfoot condition. Because the tarsal bones of infants are not completely

ossified and are mostly cartilaginous, it has been difficult to assess the morphology and alignment of individual tarsal bones during infancy. Since the advent of MRI quantitative image analysis of the cartilage anlagen has become feasible and several studies have reported volumetric measurements of these anlagen [30, 37-38, 177-178].

Traditionally, the projections of talocalcaneal angle (angle formed between the long axes of talus and calcaneus) on the lateral and axial planes have been the most accepted *radiographic* measurements for evaluation of clubfoot [46, 53, 179-180]. An increased AP (anteroposterior) talocalcaneal angle indicates valgus of the hindfoot whereas a decreased angle is an indication of varus condition where the talus and calcaneus are parallel as seen in clubfoot (Figure 6.10). The lateral talocalcaneal angle is decreased with varus or equinus and is increased with valgus or calcaneus deformities (Figure 6.9). The reported ranges in normal feet for these angles are 10-56^{o} and 15-55^{o} for the AP and lateral talocalcaneal angles respectively [179, 181-183]. For clubfeet Ponseti et al. found the AP and lateral talocalcaneal angles to be 4-25^{o} and 10-34^{o} respectively. The parallelism of talus and calcaneus in the clubfoot as opposed to the normal side is observed in Figure 6.9, and the increase in this angle can be appreciated as the treatment continues.

Correction of the medial rotation of calcaneus can also be observed in Figure 6.10. The angle between the long axis of calcaneus and the bimalleolar axis (imaginary line connecting the two lower outer points on the tibia and fibula) in the AP view has been used as a measure of the degree of medial rotation of calcaneus. As illustrated in Figure 6.10, under treatment the calcaneus departs from a severely adducted state

(medially shifted underneath the talar head) to a position nearly normal to the bimalleolar axis. An average value of 87.8^{o} has been reported for this parameter [32] for normal feet of children between 4-2 months of age.

The adaptive mechanism during manipulation and corrective casting consists of immediate cartilage anlage shape changes as the casts are applied followed by a slower adaptation during the periods the casts are maintained. In a resting (unstressed) position the hindfoot anlagen were deformed and compressed against one another by the thickened and contracted soft tissues, so when these loads are removed by the corrective cast the cartilage anlage immediately acquired a more normal shape. After a period of one week on average in the corrective cast, there were no drastic changes in the shapes or relative positions of the anlagen from just prior to after cast removal. This suggests that during the period of casting, the anlagen matrix adapted to their new shapes and positions so they did not revert to the original shape when the loads induced by the cast were removed, but rather maintained the more normal shape imposed immediately after casting. This phenomenon raises interesting speculations: How quickly do these adaptive changes occur? If they occur much quicker than one week, then cast frequency could be increased, perhaps decreasing the time of treatment and even resulting in more normal shapes.

It is evident from the results of the present study that the rate of bone formation is significantly higher in clubfoot undergoing Ponseti treatment than the normal side. It is widely believed that the ossification of the cartilage rudiments is mechanically regulated beginning from early stages of endochondral ossification and continuing throughout life.

Observations of skeletal development in human embryos with muscular defects, and experiments on avian embryos lend support to this view. Based on the idea of Pauwels [184] concerning the relative influence of hydrostatic and shear stress, Carter proposed the bone maintenance theory [108] which describes the tendency of formation of fibrous connective tissue, cartilage, or bone by an osteogenic index

$$I = \sum_{i=1}^{c} n_i (S_i + kD_i)$$

where n_i is the number of loading cycles of a particular loading condition, c is the number of such different loading conditions, S and D denote the cyclic octahedral shear stress and hydrostatic stress respectively, and k is a constant weight factor. Carter and colleagues [3, 185] have proposed that endochondral ossification is accelerated by cyclic shear stress and slowed down by cyclic compressive dilatational stress. Dilatational (or hydrostatic) stresses produce volume changes if the material is compressible, but no distortion, whereas deviatoric (distortional or shear) stresses cause material distortion but no volume change. The stored strain energy is the sum of the deviatoric and dilatational energy.

Experimentally, the effects of different biophysical stimuli on the process of endochondral ossification have been studied in *in vitro* organ culture models of fetal murine metatarsal bones [73-75], where hydrostatic compression was found to stimulate chondrocyte hypertrophy and the extracellular matrix mineralization. In one of these studies [73] for instance, effect of intermittent and constant compressive force (ICF and CCF) on ossifying long bones and calvarial rudiments was investigated, and it was

reported that ICF did not accelerate the onset of cartilage hypertrophy, but once a hypertrophic zone had developed, ICF accelerated mineralization in this zone. This effect was ascribed to the development of shear stresses at the interface of mineralized and non-mineralized tissue under the influence of hydrostatic pressure.

Studies concerning the effect of immobilization on cartilage maintenance and cartilage turnover to bone showed that cartilage formation was induced in the chick embryonic tissue under intermittent mechanical stimulation; however, on the contrary to the commonly accepted views, immobilization of the cell cultures caused transformation of this cartilage into a bone-like structure [186-187]. Similarly, in a study using a rat model for bone repair, the fate of mechanically induced cartilage after unloading was investigated [188]. The mainly hydrostatic stresses in their experiment induced both cartilage formation and bone resorption in agreement with Carter's theory, but when the mechanically induced cartilage was maintained in unloaded conditions, unloading was found likely to facilitate endochondral ossification rather than cartilage metabolism.

From the mechanics stand point, our findings could be explained by Carter's theory and the above experiments. The tendons and ligaments are shortened in clubfoot, and the foot is in supination and plantarflexion. In addition, the navicular is eminently shifted medially and presses tightly against the medial aspect of the talar head. This malpositioning of the anlagen creates compressive stresses in the head and neck area. With the Ponseti technique, the first cast corrects the cavus deformity (lifts the first metatarsal), the second cast starts to externally rotate the supinated and plantarflexed foot around lateral head of talus, and the process of gradual correction is continued in the

following casts until all components of deformity are corrected simultaneously (as previously stated, the equinus deformity may persist until the end in which case a heel chord tenotomy will be performed). It may be postulated that without treatment, intermittent compression on the anlagen is maintained by muscle contractions in the foot in supination, plantarflexion, and cavus deformities thereby inhibiting bone formation in the talus. As the deformities are corrected with manipulation therapy and immobilization in the cast, the pressure on the anlagen is released and the ossification is much improved. During the cast period, intermittent muscle contractions are present through wiggling of the foot but with much lower magnitudes and possibly lower frequency than when mobile. The accelerated ossification in the talus while immobilized in the cast is consistent with the experiments cited above. Such magnitude and frequencies are unknown to our knowledge, but it is possible that they are similar to those in the late fetal periods. These muscles probably apply small amounts of stress on the anlagen that are positioned in a more corrected form thus inducing ossification in a more normal template. The progressively stiffening caused by more bone formation will in turn prevent the foot from reverting to its pre-correction form after cast removal.

The interpretation of our results based on previous research should be taken tentatively, due to lack of sufficient knowledge on the loading environment in the foot such as ligament and tendon forces, pressure magnitudes applied among the anlagen, muscle contractile forces, and the frequency of occurrence of these quantities in normal foot, in untreated clubfoot, and clubfoot undergoing manipulation and immobilization therapy. These become especially important since Carter emphasizes the importance of intermittent stimulation, and its difference with static loading.

Consistent with previous observations, our MRI scans show that the ossification center in the neck of the talus is situated in a more lateral position as compared to normal. Due to the varus of the forefoot and compression of the navicular against the head of the talus on its medial aspect, the medial side of talus must be in compression whereas the lateral side is under tension, thus more bone formation occurs near the lateral side. Similarly, Fritsch and Eggers speculated based on the view of Pauwels, that their findings indicating formation of perichondral bone on the inferomedial surface of the clubfoot calcaneus as compared to its lateral position in normal calcaneus could be explained by possibly higher bending stresses at the inferomedial surface cause by the deformities and a short and uncoiled Achilles tendon. It must be noted that Pauwels's view of 'endochondral' ossification and the genesis of the secondary ossific nucleus is in conflict with the theory of Carter and co-workers, as he believed that the secondary ossific nucleus forms in the areas of "pure and high hydrostatic pressure".

Our finite elements analysis results revealed no correlation between the amount of bone deposition between each two visits and either the equivalent von Mises stress or the hydrostatic pressure. Our findings, however, suggest a significant positive correlation between the strain energy density stored in the areas of cartilage around the surface of the ossific nucleus, and the increase in the size of the ossific nucleus when the hyperelastic UMAT model was used to represent the solid matrix. Stress is a tensor quantity and in a three dimensional analysis it must be defined by either six stress components or three principal strains and their orientation angles, whereas the strain energy density is a scalar quantity that has no directional preference and is an invariant of the amount of distortion, thus providing a direct measure of it. The energy drives the biochemical reactions

involved with the ossification of the cartilage anlage, and is stored in the solid matrix. When the material is nearly incompressible such as cartilage (here $\nu_s = 0.37$), the strain energy density arises mostly from the deviatoric stresses. Our study showed a significant correlation between the volume added to the ossific nucleus with one (strain energy density), but not the other (von Mises stress). This might be due to the departure from incompressibility. The computed strain energy density is the true energy density (that of the solid matrix) and not an apparent level quantity.

Inclusion of the fluid phase in finite element analyses of cartilage is important as the fluid flow can significantly alter the deformation of the solid due to the frictional drag forces resulting from the movement of one phase relative to the other. Carter's theory [108] has been used in finite element models to analyze tissue morphogenesis with the tissue represented as an elastic isotropic solid. Prendergast and Huskies [189] studied the peri-prosthetic tissue formation observed in an animal experiment using finite element analyses with both elastic and biphasic models. Their results yielded different osteogenic indices for the two, and showed that the osteogenic index works best when the tissue is modeled as a biphasic material. Similarly, discrepancies were observed between the results of the two approaches and the consequent interpretations in a study of mineralization of fetal cartilaginous metatarsals [88]. In our study, both the solid and fluid phases were included. As a result, we were able to study two parameters as stimulus candidates: magnitude of the pore fluid effective velocity, and the total fluid volume ratio.

Mechanical loading not only deforms the tissue, but also causes movement of extracellular fluid through the matrix. There is growing body of evidence that fluid flow within the canaliculae and lacunae of bone is primarily responsible for mechano-chemical signal transduction in bone cells [80]. Theoretical models have also been developed describing the excitation of osteocytes by fluid shear stress induced by mechanical loading [84]. Such fluid flow may stimulate bone cells via wall shear stress, streaming potentials, or chemo-transport related effects [77-79]. The dominant determinant of the bone cell's response to this fluid flow is hypothesized to be due to fluid shear stresses that stimulate cell wall processes [84-87], causing cell deformation and subsequent metabolic activity via integrins and the cytoskeleton [81].

In our study, when the hyperelastic UMAT was used to represent the solid matrix, we found statistically significant positive correlations between both of these parameters and the change in the volume of the ossific nucleus, but when the matrix was regarded as linear elastic, a significant correlation was found between the added volume and the magnitude of fluid velocity only (see Tables 6.8 and 6.9). It can be argued that the fluid flow around the ossific nucleus stimulates the hypertrophied chondrocytes leading to ossification.

We calculated the fluid velocity at the interface of the cartilage and bone, where the ossified region was considered solid. The effect of porosity of the bony tissue was taken into account when using the empirical law between in its density and the Young's modulus (equation #); however, the bone geometry itself was not regarded as porous in the FE model. The stress and velocity profiles at the cartilage/bone interface will change

by adapting more realistic boundary conditions; nonetheless, our results clearly show that the choice of material model for the solid matrix lead to different results regarding the volume ratio of the present fluid. Different models of solid matrix lead to different deformations and subsequently different flow patterns.

In studies of the ossifying femoral anlage and osteoarthritic adult hip joint [185, 190], the vascular blood supply to the femoral head correlated with regions not subjected to high magnitudes of intermittent hydrostatic compression. This is consistent with disrupted vascularization in the neck and head region of the talus under high compressive forces in the presence of clubfoot deformities.

The talus is the first tarsal to show cartilage canals [191]. The cartilage anlage of the talus is well vascularized throughout by cartilage canals containing blood vessels and connective tissue before the appearance of the primary ossification center [191-192]. Because the primary ossification center of the irregular bones (and the epiphyses of the long bones) occur in very late fetal periods or postnatally, the cartilage mass is large beyond the diffusion of the perichondral vessels and the cartilage canals develop to supply the large cartilage structures. They nourish the cartilage and supply osteogenic tissue to develop the ossification center of the talus.

The normal adult arterial blood supply to the ankle and foot is generally provided by three arteries: posterior tibial, anterior tibial, and peroneal. However, alteration of this normal arterial pattern has been documented to occur at a high frequency in patients with clubfoot [193-199]. The cartilage anlage of the talus is the first among the tarsals to show vascular invasion in early fetal life, but its ossification does not start until late fetal life

[21]. The normal adult talus is well vascularized from four sides [200-201]. The body of the talus is mostly supplied by the anastomotic artery in the tarsal canal, and by the deltoid branches as the second most important source [201]. These vessels derive from the posterior tibial artery which is the major vessel supplying the foot [195]. The head of the talus is supplied from two sources: branches from the anterior tibial artery or the dorsalis pedis artery supplying the medial superior half, and the artery of the tarsal sinus supplying the lateral and inferior half of the head [201]. Fritsch et al. [36] found similar blood supply to the adult in the talar ossification center in new born. As compared to adult, it was shown that the main blood supply in the newborn derived from the vessels of the sinus tarsi [36, 192], and also from the dorsal neck vessels [36]. The superior surface of the talar neck is invaded by superior neck vessels [36]. They derive from the dorsalis pedis artery, enter the talar head and branch within the ventral tip of the ossification center [36] (the manner in which the branches of these vessels reach the ossification center through cartilage canals have been described [191]). Arteriographic studies of clubfoot have found moderate to severe circulatory deficiency involving the dorsalis pedis artery [193, 195], and the posterior tibial artery [194, 196-197, 199]. The anterior tibial artery has also been reported hypoplastic in clubfoot patients [195, 199].

Vascular disruption in the anterior part of talus could possibly be in part due to the malpositioning of the foot anlagen imposing high magnitudes of compression on those regions when untreated. The patient will walk on the outside of the foot (supinated foot) if treatment is not performed, leading to further disruption of vascular supply. With treatment performed, in addition to mechanical stimulation of chondrocytes and osteocytes, it is possible that rechanneling of the blood supply occurs with lifting of the

hydrostatic compression from the anterior region of the talus. This will bring in supplies of osteogenic tissue to the ossification center leading to further development of bone.

We stress that these postulated mechanisms are unique, since the emphasis has always been on stretching of tendons and ligaments leading to correction of relative positions of the anlagen, and not on correction of the anlagen shapes and their ossification centers (Ponseti, however, commented on the correction of the angle of the talar neck [202]). There were only two patients with treatment intervals of 3 and 4 days, and the other patients had an average of 7 days elapsed between treatments. The number of cases was not large enough to delineate a difference between the means of ossification rates of these two groups. However, based on our observations, this rate is clearly higher in the clubfoot undergoing treatment than in the normal side, and additionally, it declines over time. Altogether, this suggests the outstanding possibility of improvement in the outcome if treatment is initiated immediately after birth: faster bone formation will occur in the treated clubfoot side which will continue to deposit on a cartilaginous template that is also continuously adopting a more correct form even more rapidly due to reshaping under manipulation and casting. Shorter periods between treatments can therefore possibly enhance the treatment outcome, but such a conclusion requires study of a large number of patients. If we knew that the cartilage anlagen did not revert to their previous shapes and positions, undoubtedly more treatments with shorter wait in between would be the ideal solution. The question then becomes: how long between each two visits is long enough for the cartilage anlagen and the tendons to completely adapt to their corrected forms and maintain the corrections upon cast removal at each session and finally after the last treatment session. The importance of this mechanism is that it opens

the possibility of a new way to guide the initial nonoperative treatment of clubfoot: the frequency and number of manipulations and corrective castings might be gauged by the degree of shape and positional changes of the anlagen, and the timing of cessation of treatment might be based upon appropriate shape and position corrections achieved.

7.2 Limitations and Future Work

There are several limitations in the present study. First and foremost, there is a limitation in the number of patients in a human study of this nature. Cost as well as obtaining consent of parents for examination of their child according to the protocol is not trivial: the protocol included mild sedation and three sets of scans per each treatment session for the clubfoot side and one set for the normal side. Access to a higher number of patients if possible would provide better assessment of the deformities and the mechanisms of correction. Similar limitation existed regarding access to human cadaveric material. We used full-term fetal tissue for mechanical characterization as an approximation to the new-born as the average age of the clubfoot patients was 40 days. Characterization of the involved tissue at ages closer to the patients' is likely to provide more accurate results and such is the case with testing of a higher number of samples if available.

Although useful results have been produced using our UMAT, the developed model has not been tested exhaustively. This is due to the general limitation of the study regarding limited supply of cadaveric material. A larger number of examples have to be run, and compared with experimental/clinical data for a reliable validation. The model is better applicable for isotropic homogeneous materials such as the immature tissue under study here. In the general context of soft tissues, depending on the site, these assumptions

may not bear close proximity to reality. Thus, it seems reasonable to consider models which can account for inhomogeneity, anisotropy and deformation nonlinearities simultaneously (Huang et al. [128], Wilson et al. [203]) when the tissue mechanics itself is the central focus. However, when mechanobiological studies are the scope of interest, it is important to realize the involved compromise on the computational cost. It is possible to use an extremely detailed model that can factor for many features of the tissue structure and composition; however, if implementing another class of intricacies other than tissue mechanics - such as growth and adaptation - is the purpose, it might be more reasonable to suffice to a model that produces reasonably good results allowing to explore such mechanisms without too heavy computational cost.

In the models of morphogenesis, the direct effects of mechanical environment on cell metabolism and tissue adaptation are considered but the indirect influence of mechanical stimulation on development through mechanisms such as changes in patterns of vascularization require attention. One such example is the hindrance and progression of endochondral ossification in birth defects such as clubfoot, where vascular disruption (vascular hypoplasia) is considered one of the possible origins of this deformity. The here used interpretation of our data related to the vascular abnormalities is not unique but one of many reasonable possibilities; nonetheless, creating models of cartilage anlagen that incorporate tissue vascularization along with mechanobiological models including such events seems a helpful strategy in casting light on the present subject. With a deformity so diverse in its possible causes, one can only speculate based on such limited data. Among other theories of etiology of clubfoot, the intrauterine molding defect, blastemic defect of the tarsal cartilage, and abnormal tendon insertions are a few readily

investigable mechanically by building on the available body of work that has researched various mechanisms of development.

We studied the stresses caused by changes in shape of the talus and assumed the other sources of stress to remain unchanged under manipulation so that they would serve as a baseline upon which the additional stresses created by anlagen shape changes were added; however, one of the correction mechanisms in clubfoot treatment is the stretching of the tendons to a more normal length, and inclusion of the sites of tendon insertion and the forces they produce under treatment can create more accuracy. Additionally, research on adaptation of tendons and ligaments and the time scale of these events may be an important consideration. The change in articulation surfaces was taken into account in the sense that the shape changes are accompanied by a relative shift of the neighboring anlagen following the contour of the manipulated anlage, therefore, the deformation field calculated based on the difference of the two geometries provided some information on the stresses imposed by the newly achieved congruity. More definitive results are likely to be obtained however, by incorporating details on the interactions among the various anlagen.

There is a lack of certainty in the segmentation of the scans as well as the manner in which the anlagen of different visits are aligned. This is possibly one reason why the geometrical comparison data at bone surface points obtained from mapping of the old bone surface to the new bone surface did not correspond to the spatial distribution of mechanical quantities. It was only when these quantities were averaged over the region surrounding the bone surface and correlated with the added bone volume that significant

correlations were present between the two. It is not expected that mechanical stimulation did not affect this process and an effect did not exist, but rather insufficiency of the tools to detect this effect seems to be the most probable cause. The anlagen, especially the talus which was the focus of the current study, have highly irregular shapes. The ossification of talus does not occur symmetrically and equally in all directions, i.e., the ossific nucleus of the talus is not a miniature representation of the talar anlage itself. It is for this reason that it is invaluable to this type of studies to identify methods which can enable exploring the directionality of bone deposition in response to mechanical modulation, in addition to an average sense. Additionally, our results indicate the stimulation of the cartilage leading to bone formation, but not the bone itself directly. Information on the internal development of the ossification center, with the aid of tools such as high resolution CT for instance, and pairing it up with theories of bone remodeling and adaptation can provide a window of opportunity for studying stimulation and internal development of the bone as well.

Finally, to target the question raised in the last paragraph of the discussion regarding the possibility of improvement by shortening the amount of time between treatment sessions, it is important to study a larger population of patients that had treatment performed at different intervals to allow for analysis of variance.

In summary, characterizing the spatial and temporal sequences of development of the human hindfoot anlagen, and identifying the mechanisms by which they occur might well serve as paradigms for tissue engineering and regenerative medicine approaches, as well as study of human musculoskeletal diseases.

LIST OF REFERENCES

[1] Weinstein, S. L., and Buckwalter, J. A., 2005, Turek's Orthopaedics: Principles and Their Application, Lippincott Williams and Wilkins, Philadelphia.

[2] Smith, J. W., 1962, "The relationship of epiphyseal plates to stress in some bones of the lower limb," Journal of Anatomy, 96, pp. 58-78.

[3] Carter, D. R., and Wong, M., 1988, "The role of mechanical loading histories in the development of diarthrodial joints," Journal of Orthopaedic Research, 6(6), pp. 804-816.

[4] Mow, V. C., Kuei, S. C., Lai, W. M., and Armstrong, C. G., 1980, "Biphasic creep and stress relaxation of articular cartilage in compression: Theory and experiments.," Journal of Biomechanical Engineering, 102(1), pp. 73-84.

[5] Cohen, B., Lai, W. M., and Mow, V. C., 1998, "A transversely isotropic biphasic model for unconfined compression of growth plate and chondroepiphysis," Journal of Biomechanical Engineering, 120(4), pp. 491-496.

[6] Mak, A. F., 1986, "The apparent viscoelastic behavior of articular cartilage - the contributions from the intrinsic matrix viscoelasticity and interstitial fluid flows," Journal of Biomechanical Engineering, 108(2), pp. 123-130.

[7] Soulhat, J., Buschmann, M. D., and Shirazi-Adl, A., 1999, "A fibril-network-reinforced biphasic model of cartilage in unconfined compression," Journal of Biomechanical Engineering, 121(3), pp. 340-347.

[8] Soltz, M. A., and Ateshian, G. A., 2000, "A Conewise Linear Elasticity mixture model for the analysis of tension-compression nonlinearity in articular cartilage," Journal of Biomechanical Engineering, 122(6), pp. 576-586.

[9] Lai, W. M., Hou, J. S., and Mow, W. C., 1991, "A triphasic theory for the swelling and deformation behaviors of articular cartilage," Journal of Biomechanical Engineering, 113(3), pp. 245-258.

[10] Huyghe, J. M., and Janssen, J. D., 1997, "Quadriphasic mechanics of swelling incompressible porous media," International Journal of Engineering Science, 35(8), pp. 793-802.

[11] Mahmoodian, R., Leasure, J., Philip, P., Pleshko, N., Brand, R., Capaldi, F., and Siegler, S., 2011, "Changes in the mechanics and composition of human talar cartilage anlage during fetal development," Osteoarthritis and Cartilage, Accepted.

[12] Spilker, R. L., Suh, J. K., Vermilyea, M. E., and Maxian, T. A., 1990, "Alternate hybrid, mixed, and penalty finite element formulations for biphasic model of soft hydrated tissues," Biomechanics of diarthrodial joints, V. C. Mow, A. Ratcliffe, and S. L.-Y. Woo, eds., Springer, New York, pp. 400-435.

[13] Suh, J. K., Spilker, R. L., Holmes, M. H., and Mow, V. C., 1989, "A nonlinear biphasic finite element formulation for soft hydrated tissues under finite deformation," 1989 advances in bioengineering, B. Rubinsky, ed., ASME, New York, pp. 99-100.

[14] Almeida, E. S., and Spilker, R. L., 1998, "Finite element formulations for hyperelastic transversely isotropic biphasic soft tissues," Computer Methods in Applied Mechanics and Engineering, 151, pp. 513-538.

[15] Mahmoodian, R., Siegler, S., and Capaldi, F., 2011, "A finite element implementation of the finite deformation biphasic theory," In preparation.

[16] Holmes, M. H., and Mow, V. C., 1990, "The nonlinear characteristics of soft gels and hydrated connective tissues in ultrafiltration," Journal of Biomechanics, 23(11), pp. 1145-1156.

[17] Caroll, N., 1990, Clubfoot, J.B.Lippincott, Philadelphia.

[18] Mosca, V. S., 2001, The Foot, Lippincott Williams & Wilkins, Philadelphia.

[19] Zlatko, A., and Dietz, F., 2004, "Ponseti Method of Idiopathic Clubfoot Treatment," http://www.uihealthcare.com/news/currents/vol1issue1/clubfoot.html.

[20] Brand, R. A., Siegler, S., Pirani, S., Morrison, W. B., and Udupa, J. K., 2006, "Cartilage anlagen adapt in response to static deformation," Medical Hypotheses, 66, pp. 653-659.

[21] Gardner, E., Gray, D. J., and O'Rahilly, R., 1959, "The prenatal development of the skeleton and joints of the human foot " The Journal of Bone and Joint Surgery, 41(5), pp. 847-876.

[22] Sarrafian, S. K., 1993, Anatomy of the foot and ankle, J. B. Lippincott Co., Philadelphia.

[23] Atlas, S., Menacho, L. C., and Ures, S., 1980, "Some new aspects in the pathology of clubfoot," Clinical Orthopaedics and Related Research, pp. 224-228.

[24] Cahuzac, J. P., Baunin, C., Luu, S., Estivalezes, E., and Gauzy, J. S. d., 1999, "Assessment of hindfoot deformity by three dimensional MRI in infant club foot," The Journal of Bone and Joint Surgery (British), 81(1), pp. 97-101.

[25] Howard, C. B., and Benson, M. K., 1992, "The ossific nuclei and the cartilage anlage of the talus and calcaneum," The Journal of Bone and Joint Surgery (British), 74, pp. 620-623.

[26] Ippolito, E., 2004, "Validity of the anteroposterior talocalcaneal angle to assess congenital clubfoot correction," American Journal of Roentgenology, 182, pp. 1279-1282.

[27] Joseph, B., Bhatia, M., and Nair, N. S., 2001, "Talo-calcaneal relationship in clubfoot," Journal of Pediatric Orthopaedics, 21, pp. 60-64.

[28] Pirani, S., Zeznik, L., and Hodges, D., 2001, "Magnetic resonance imaging study of the congenital clubfoot treated with the Ponseti method," Journal of Pediatric Orthopaedics, 21, pp. 719-726.

[29] Ponseti, I. V., 1996, Congenital Clubfoot: Fundamentals of Treatment, Oxford University Press, Oxford.

[30] Itohara, T., Sugamoto, K., Shimizu, N., Ohno, I., Tanak, H., Nakajima, Y., Sato, Y., and Yoshikawa, H., 2005, "Assessment of talus deformity by three-dimensional MRI in congenital clubfoot," European Journal of Radiology, 53, pp. 78-83.

[31] Kalenderer, O., Reisoglu, A., Turgut, A., and Agus, H., 2008, "Evaluation of clinical and radiographic outcomes of complete subtalar release in clubfoot treatment," Journal of the American Podiatric Medical Association, 98(6), pp. 451-456.

[32] Kamayega, M., Shinohara, Y., Kokuji, Y., and Moriya, H., 2000, "Evaluation of pathologic abnormalities of clubfoot by magentic resonance imaging," Clinical Orthopaedics and Related Research, 379, pp. 218-223.

[33] Hart, R. G., Rittenberry, T. J., and Uehara, D. T., 1999, Handbook of orthopaedic emergencies Lippincott-Raven, Philadelphia.

[34] Shapiro, F., and Glimcher, M. J., 1979, "Gross and histological abnormalities of the talus in congenital club foot," The Journal of Bone and Joint Surgery (American), 61(4), pp. 522-530.

[35] Cheng, X., Wang, Y., Qu, H., and Jiang, Y., 1995, "Ossification processes and perichondral ossification groove of Ranvier: a morphological study in developing human calcaneus and talus," Foot & Ankle International, 16(1), pp. 7-10.

[36] Fritsch, H., Schmitt, O., and Eggers, R., 1996, "The ossification centre of the talus," Annals of Anatomy, 178(5), pp. 455-459.

[37] Fritsch, H., and Eggers, R., 1999, "Ossification of the calcaneus in the normal fetal foot and in clubfoot," Journal of Pediatric Orthopaedics, 19(1), pp. 22-26.

[38] Cahuzac, J. P., Navascues, J., Baunin, C., Gauzy, J. S. d., Estivalezes, E., and Swider, P., 2002, "Assessment of the position of the navicular by three dimensioanl magnetic resonance imaging in infant foot deformities," Journal of Pediatric Orthopaedics, B11, pp. 134-138.

[39] Irani, R. N., and Sherman, M. S., 1972, "The pathological anatomy of idiopathic clubfoot," Clinical Orthopaedics and Related Research, 84, pp. 14-20.

[40] Ponseti, I. V., and Campos, J., 1972, "Observations on pathogenesis and treatment of congenital clubfoot," Clinical Orthopaedics and Related Research, 84(50-60).

[41] Brick, E., 1968, Source book of orthopaedics, Hafner Publishing Company, New York.

[42] Lay, D. D., 1990, The history of orthopaedics: an account of the study and practice of orthopaedics from the earliest times to the modern era, The Parthenon Publishing Group, Park Bridge, NJ.

[43] Whitman, R., 1907, Treatise on Orthopaedic Surgery, Lea Brothers & Co, Philadelphia.

[44] Little, W. J., 1839, A Treatise on the Nature of Club-foot, and Analogous Distortions; Including Their Treatment Both With and Without Surgical Operation1839., Longmans.

[45] Stroymeyer, G. F., 1838, Beitrag zur operative Orthopaedie oder Erfahrungen über die subkutane Durchschneidung verkürtzter Muskeln, Verlage der Helwig'schen Hofbuchhandlung, Hanover.

[46] Kite, J. H., 1939, "Principles Involved in the treatment of Congenital Clubfoot," The Journal of Bone and Joint Surgery (American), 21, p. 595.

[47] McKay, D. W., 1988, "Surgical correction of clubfoot," Instructional Course Lectures, 37, pp. 87-92.

[48] Kausch, T., Rutt, J., Hackenbrotch, M. H., and Funfgeld, B., 1995, "Treatment results of Imhauser's method of treating neonatal clubfeet," Z Orthop Ihre Grenzgeb, 133, pp. 524-529.

[49] Weinstein, S. L., 1994, Chapter 18, The Pediatric Foot, Lippincott Williams & Wilkins, Philadelphia.

[50] Dobbs, M. B., Morcuende, J. A., Gurnett, C. A., and Ponseti, I. V., 2000, "Treatment of idiopathic clubfoot: an historical review," The Iowa Orthopaedic Journal, 20, pp. 59-64.

[51] Dobbs, M., 2004, "Factors predictive of outcome after use of the Ponseti method for the treatment of idiopathic clubfeet," J Bone Joint Surg Am, 86-A, pp. 22-27.

[52] Goksan, S. B., 2002, "Treatment of congenital clubfoot with the Ponseti method," Acta Orthopaedica et Traumatologica Turcica, 36, pp. 281-287.

[53] Herzenberg, J. E., Radler, C., and Bor, N., 2002, "Ponseti versus traditional methods of casting for idiopathic clubfoot," Journal of Pediatric Orthopaedics, 22, pp. 517-521.

[54] Ippolito, E., and Ponseti, I. V., 1980, "Congenital club foot in the human fetus. A histological study," The Journal of Bone and Joint Surgery (American), 62, pp. 8-22.

[55] Scher, D. M., Feldman, D. S., Bosse, H. J. v., Sala, D. A., and Lehman, W. B., 2004, "Predicting the need for tenotomy in the Ponseti method for correction of clubfeet," Journal of Pediatric Orthopaedics, 24, pp. 349-352.

[56] Ponseti, I. V., and Becker, R., 1966, "Congenital metatarsus adductus: the results of treatment," The Journal of Bone and Joint Surgery (American), 48(4), pp. 702-711.

[57] Turner, C. H., and Pavalko, F. M., 1998, "Mechanotransduction and functional response of the skeleton to physical stress: The mechanisms and mechanics of bone adaptation," Journal of Orthopaedic Science, 3, pp. 346-355.

[58] Lane Smith, R.,, Rusk, S. F., Ellison, B. E., Wessels, P., Tsuchiya, K., Carter, D. R., Caler, W. E., Sandell, L. J., and Schurman, D. J., 1996, "In vitro stimulation of articular chondrocyte mRNA and extracellular matrix synthesis by hydrostatic pressure," Journal of Orthopaedic Research, 14(1), pp. 53–60.

[59] Lane Smith, R., Trindade, M. C., Ikenoue, T., Mohta, M., Das, P., Carter, D. R., Goodman, S. B., and Schurman, D. J., 2000, "Effects of shear stress on articular chondrocyte metabolism," Journal of Biorheology, 37(1-2), pp. 95-107.

[60] Lane Smith, R., Carter, D. R., and Schurman, D. J., 2004, "Pressure and shear differentially alter human articular chondrocyte metabolism: a review," Clinical Orthopaedics and Related Research, 427 Suppl, pp. S89-95.

[61] Grodzinsky, A. J., Levenston, M. E., M, M. J., and Frank, E. H., 2000, "Cartilage tissue remodeling in response to mechanical forces," Annual Review of Biomedical Engineering, 2, pp. 691-713.

[62] Grodzinsky, A. J., 1983, "Electromechanical and physicochemical properties of connective tissue," Critical Reviews in Biomedical Engineering, 9(2), pp. 133-199.

[63] Lee, M. S., Trindade, M. C., Ikenoue, T., Schurman, D. J., Goodman, S. B., and Smith, R. L., 2003, "Intermittent hydrostatic pressure inhibits shear stress-induced nitric oxide release in human osteoarthritic chondrocytes in vitro," Journal of Rheumatology, 30(2), pp. 326-328.

[64] Guilak, F., Donahue, H. J., Zell, R. A., Grande, D., McLeod, K. J., and Rubin, C. T., 1994, "Deformation-induced calcium signaling in articular chondrocytes," Cell mechanics and cellular engineering, V. C. Mow, F. Guilak, R. Transon-Tay, and R. M. Hochmuth, eds., Springer-Verlag, New York, pp. 380-397.

[65] Lee, D. A., and Bader, D. L., 1997, "Compressive strains at physiological frequencies influence the metabolism of chondrocytes seeded in agarose," Journal of Orthopaedic Research, 15(2), pp. 181-188.

[66] Sah, R. L., Kim, Y. J., Doong, J. Y., Grodzinsky, A. J., Plaas, A. H., and Sandy, J. D., 1989, "Biosynthetic response of cartilage explants to dynamic compression," Journal of Orthopaedic Research, 7(5), pp. 619-636.

[67] Urban, J. P., 1994, "The chondrocyte: a cell under pressure," British Journal of Rheumatology, 33(10), pp. 901-908.

[68] Kim, Y. J., Sah, R. L., Gordinsky, A. J., Plaas, A. H., and Sandy, J. D., 1994, "Mechanical regulation of cartilage biosynthetic behavior: physical stimuli," Archives of Biochemistry and Biophysics, 311(1), pp. 1-12.

[69] Kim, Y. J., Bonassar, L. J., and Grodzinsky, A. J., 1995, "The role of cartilage streaming potential, fluid flow and pressure in the stimulation of chondrocyte biosynthesis during dynamic compression," Journal of Biomechanics, 28(9), pp. 1055-1066.

[70] Suh, J. K., Baek, G. H., Arøen, A., Malin, C. M., Niyibizi, C., Evans, C. H., and Westerhausen-Larson, A., 1999, "Intermittent sub-ambient interstitial hydrostatic pressure as a potential mechanical stimulator for chondrocyte metabolism," Osteoarthritis and Cartilage, 7(1), pp. 71–80.

[71] Wright, M., Jobanputra, P., Bavington, C., Salter, D. M., and Nuki, G., 1996, "Effects of intermittent pressure-induced strain on the electrophysiology of cultured human chondrocytes: evidence for the presence of stretch-activated membrane ion channels," Clinical science (London), 90(1), pp. 61-71.

[72] Tanck, E., Blankevoort, L., Haaijman, A., Burger, E. H., and Huiskes, R., 2000, "Influence of muscular activity on local mineralization patterns in metatarsals of the embryonic mouse," Journal of Orthopaedic Research, 18(4), pp. 613-619.

[73] Burger, E. H., Klein-Nulend, J., and Veldhuijzen, J. P., 1992, "Mechanical stress and osteogenesis in vitro," Journal of Bone and Mineral Research, 7(Suppl 2), pp. S397-S401.

[74] Klein-Nulend, J., Veldhuijzen, J. P., van de Stadt, R. J., van Kampen, G. P., Kuijer, R., and Burger, E. H., 1987, "Influence of intermittent compressive force on proteoglycan content in calcifying growth plate cartilage in vitro," The Journal of Biological Chemistry, 262(32), pp. 15490-15495.

[75] van't Veen, S. J., Hagen, J. W., van Ginkel, F. C., Prahl-Andersen, B., and Burger, E. H., 1995, "Intermittent compression stimulates cartilage mineralization," Bone, 17(5), pp. 461-465.

[76] Klein-Nulend, J., Veldhuijzen, J. P., and Burger, E. H., 1986, "Increased calcification of growth plate cartilage as a result of compressive force in vitro," Arthritis & Rheumatism, 29(8), pp. 1002-1009.

[77] Jacobs, C. R., Yellowley, C. E., Davis, B. R., Zhou, Z., Cimbala, J. M., and Donahue, H. J., 1998, "Differential effect of steady versus oscillating flow on bone cells," Journal of Biomechanics, 31(11), pp. 969-976.

[78] Pienkowski, D., and Pollack, S. R., 1983, "The origin of stress-generated potentials in fluid-saturated bone," Journal of Orthopaedic Research, 1(1), pp. 30-41.

[79] Reich, K. M., Gay, C. V., and Frangos, J. A., 1990, "Fluid shear stress as a mediator of osteoblast cyclic adenosine monophosphate production," Journal of Cell Physiology, 143(1), pp. 100-104.

[80] Duncan, R. L., and Turner, C. H., 1995, "Mechanotransduction and the functional response of bone to mechanical strain," Calcified tissue international, 57(5), pp. 344-358.

[81] Ehrlich, P. J., and Lanyon, L. E., 2002, "Mechanical strain and bone cell function: a review," Osteoporosis International, 13(9), pp. 688-700.

[82] Glucksmann, A., 1939, "Studies on bone mechanics in vitro. II. The role of tension and pressure in chondrogenesis," The Anatomical Record, 73(1), pp. 39-56.

[83] Brown, T. D., 2000, "Techniques for mechanical stimulation of cells in vitro: a review " Journal of Biomechanics, 33(1), pp. 3-14.

[84] Weinbaum, S., Cowin, S. C., and Zeng, Y., 1994, "A model for the excitation of osteocytes by mechanical loading-induced bone fluid shear stresses," Journal of Biomechanics, 27(3), pp. 339-360.

[85] Smalt, R., Mitchell, F. T., Howard, R. L., and Chambers, T. J., 1997, "Induction of NO and prostaglandin E2 in osteoblasts by wall-shear stress but not mechanical strain," American Journal of Physiology - Endocrinology and Metabolism, 273(4), pp. E751-E758.

[86] Burger, E. H., and Klein-Nulend, J., 1999, "Mechanotransduction in bone—role of the lacunocanalicular network," FASEB J, 13(8 Suppl), pp. S101-S112.

[87] Bakker, A. D., Soejima, K., Klein-Nulend, J., and Burger, E. H., 2002, "The production of nitric oxide and prostaglandin E2 by primary bone cells is shear stress dependent," Journal of Biochemistry 34, 34(5), pp. 671–677.

[88] Tanck, E., Driel, W. D. v., Hagen, J. W., Burger, E. H., Blankevoort, L., and Huiskes, R., 1999, "Why does intermittent hydrostatic pressure enhance the mineralization process in fetal cartilage?," Journal of Biomechanics, 32(2), pp. 153-161.

[89] Burger, E. H., Klein-Nulend, J., Plas, A. V. D., and Nijweide, P. J., 1995, "Function of osteocytes in bone—Their role in mechanotransduction," The Journal of Nutrition, 125(7 Suppl), pp. S2020-S2023.

[90] Humphrey, J. D., 1995, "Mechanics of the arterial wall: review and directions," Critical Reviews in Biomed Engineering, 23(1-2), pp. 1-162.

[91] Taber, L. A., 1995, "Biomechanics of growth, remodeling, and morphogenesis," Applied Mechanics Reviews, 48(8), pp. 487-545.

[92] Hsu, F. H., 1968, "The influences of mechanical loads on the form of a growing elastic body," Journal of Biomechanics, 1, pp. 303-311.

[93] Cowin, S. C., and Hegedus, D. H., 1976, "Bone remodeling I: Theory of adaptive elasticity," Journal of Elasticity, 6, pp. 313-326.

[94] Skalak, R., 1981, "Growth as a finite displacement field," IUTAM Symposium on Finite Elasticity, D. E. Carlson, and R. T. Shield, eds., Martinus Nijhoff Publishers, The Hague, pp. 347-355.

[95] Skalak, R., Dasgupta, G., Moss, M., Otten, E., Dullemeijer, P., and Vilmann, H., 1982, "Analytical description of growth," Journal of Theoretical Biology, 94, pp. 555-577.

[96] Cowin, S. C., 2006, "On the modeling of growth and adaptation," Mechanics of biological tissue, G. A. Holzapfel, and R. W. Ogden, eds., Springer-Verlag, Heidelberg, pp. 29-46.

[97] Fung, Y. C., 1990, Biomechanics: motion, flow, stress, and growth, Springer, New York.

[98] Fung, Y. C., 1991, "What are the residual stresses doing in our blood vessels?," Annals of Biomedical Engineering, 19, pp. 237-249.

[99] Rodriguez, E. K., Hoger, A., and McCulloch, A. D., 1994, "Stress-dependent finite growth in soft elastic tissues," Journal of Biomechanics, 27(4), pp. 455-467.

[100] Lee, E. H., 1969, "Elastic-plastic deformation at finite strains," Journal of Applied Mechanics, 36, pp. 1-6.

[101] Wolff, J., 1986, The law of bone remodeling, Springer, Berlin.

[102] Cowin, S. C., and Van Buskirk, W. C., 1979, "Surface bone remodeling induced by a medullary pin," Journal of Biomechanics, 12, pp. 269-276.

[103] Hart, R. T., Davy, D. T., and Heiple, K. G., 1984, "A computational model for stress analysis of adaptive elastic materials with a view toward applications in strain-induced bone remodeling," Journal of Biomechanics, 106, pp. 342-350.

[104] Cowin, S. C., 1986, "Wolff's law of trabecular architecture at remodeling equilibrium," Journal of Biomechanical Engineering, 108, pp. 83-88.

[105] Cowin, S. C., 1990, "Structural adaptation of bones," Applied Mechanics Reviews, 43, pp. S126-S133.

[106] Cowin, S. C., and Sadegh, A. M., 1992, "An evolutionary Wolff's law for trabecular architecture," Journal of Biomechanical Engineering, 114, pp. 129-136.

[107] Torezen, A., and Skalak, R., 1988, "Interaction of stress and growth in a fibrous tissue," Journal of Theoretical Biology, 130, pp. 337-350.

[108] Carter, D. R., 1987, "Mechanical loading history and skeletal biology," Journal of Biomechanics, 20, pp. 1095-1109.

[109] Carter, D. R., Wong, M., and Orr, T. E., 1991, "Musculoskeletal ontogeny, phylogeny, and functional adaptation," Journal of Biomechanics, 24, pp. 3-16.

[110] Cowin, S. C., 1984, "Mechanical modeling of stress adaptation process in bone," Calcified Tissue International, 36, pp. S98-S103.

[111] Carter, D. R., Fyhrie, D. P., and Whalen, R. T., 1987, "Trabecular bone density and loading history: regulation of connective tissue biology by mechanical energy," Journal of Biomechanics, 20, pp. 785-794.

[112] Mow, V. C., Hou, J. S., Owens, J. M., and Ratcliffe, A., 1990, Biphasic and quasilinear viscoelastic theories for hydrated soft tissues, Springer-Verlag, New York.

[113] Carter, D. R., and Hayes, W. C., 1977, "The compressive behavior of bone as a two-phase porous structure," The Journal of Bone and Joint Surgery, 59(7), pp. 954-962.

[114] Hayes, W. C., Keer, L. M., Herrmann, G., and Mockros, L. F., 1972 "A mathematical analysis for indentation tests of articular cartilage," Journal of Biomechanics, 5(5), pp. 541-551.

[115] Mak, A. F., 1986b, "The apparent viscoelastic behavior of articular cartilage--the contributions from the intrinsic matrix viscoelasticity and interstitial fluid flows," Journal of Biomechanical Engineering, 108(2), pp. 123-130.

[116] Mak, A. F., 1986a, "Unconfined compression of hydrated viscoelastic tissues: a biphasic poroviscoelastic analysis," Journal of Biorheology, 23(4), pp. 371-383.

[117] Li, L. P., Soulhat, J., Buschmann, M. D., and Shirazi-Adl, A., 1999, "Nonlinear analysis of cartilage in unconfined ramp compression using a fibril reinforced poroelastic model," Journal of Clinical Biomechanics, 14(9), pp. 673-682.

[118] Wilson, W., Donkellar, C. C. v., Rietgergen, B. v., Ito, K., and Huiskes, R., 2004, "Stresses in the local collagen network of articular cartilage: a poroviscoelastic fibril-reinforced finite element study," Journal of Biomechanics, 37, pp. 357–366.

[119] Garcıa, J. J., Altiero, N. J., and Haut, R. C., 1998, "An approach for stress analysis of transversely isotropic cartilage under impact load," Journal of Biomechanical Engineering, 120, pp. 608–613.

[120] Truesdell, C., and Noll, W., 1965, "The Non-Linear Field Theories of Mechanics/Die Nicht-Linearen Feldtheorien der Mechanik," Handbuch der Physik (Encyclopedia of Physics), S. Flügge, ed., Springer-Verlag, Berlin-Heidelberg-New York.

[121] Kwan, M. K., Lai, W. M., and Mow, V. C., 1990, "A finite deformation theory for cratilage and other soft hydrated connective tissues-I. equilibrium results," Journal of Biomechanics, 23(2), pp. 145-155.

[122] Holmes, M. H., 1986, "Finite deformation of soft tissue: analysis of a mixture model in uni-axial compression," Journal of Biomechanical Engineering, 108(4), pp. 372-381.

[123] Mak, A. F., 1986, "The apparent viscoelastic behavior of articular cartilage--the contributions from the intrinsic matrix viscoelasticity and interstitial fluid flows," Journal of Biomechanical Engineering, 108(2), pp. 123-130.

[124] Fung, Y. C., 1981, Biomechanics: Mechanical Properties of Living Tissues, Springer-Verlag, New York.

[125] Bursać, P. M., Obitz, T. W., Eisenberg, S. R., and Stamenović, D., 1999, "Confined and unconfined stress relaxation of cartilage: appropriateness of a transversely isotropic analysis," Journal of Biomechanics, 32(10), pp. 1125-1130.

[126] Curnier, A., He, Q.-C., and Zysset, P., 1995, "Conewise linear elastic materials " Journal of Elasticity, 37(1), pp. 1-38.

[127] Soltz, M. A., and Ateshian, G. A., 1998, "Experimental verification and theoretical prediction of cartilage interstitial fluid pressurization at an impermeable contact interface in confined compression," Journal of Biomechanics, 31(10), pp. 927-934.

[128] Huang, C. Y., and Ateshian, G. A., 2001, "The role of flow-independent viscoelasticity in the biphasic tensile and compressive responses of articular cartilage," Journal of Biomechanical Engineering, 123(5), pp. 410-417.

[129] Huang, C. Y., Soltz, M. A., Kopacz, M., Mow, V. C., and Ateshian, G. A., 2003, "Experimental verification of the roles of intrinsic matrix viscoelasticity and tension-compression nonlinearity in the biphasic response of cartilage," Journal of Biomechanical Engineering, 125(1), pp. 84-93.

[130] Lai, W. M., and Mow, V. C., 1980, "Drag-induced compression of articular cartilage during a permeation experiment," Biorheology, 17(2-2), pp. 111-123.

[131] Ateshian, G. A., Warden, W. H., Kim, J. J., Grelsamer, R. P., and Mow, V. C., 1997, "Finite deformation biphasic material properties of bovine articular cartilage from confined compression experiments," Journal of Biomechanics, 30(11-12), pp. 1157-1164.

[132] Mow, V. C., Holmes, M. H., and Lai, W. M., 1984, "Fluid transport and mechanical properties of articular cartilage: a review," Journal of Biomechanics, 17, pp. 377-394.

[133] Simon, B. R., 1992, "Multiphasic poroelastic finite element models for soft tissue structures," Applied Mechanics Reviews, 45, pp. 191-218.

[134] Panjabi, M. M., Oda, T., J.J. Crisco, r., Oxland, T. R., Katz, L., and Nolte, L. P., 1991, "Experimental study of atlas injuries. I. Biomechanical analysis of their mechanisms and fracture patterns," Spine, 16 S, pp. 460-465.

[135] Kvalseth, T. O., 1985, "Cautionary note about R2," The American Statistician, 39(4), pp. 279-285.

[136] Prendergast, P. J., Driel, W. D. v., and Kuiper, J. H., 1996, "A comparison of finite element codes for the solution of biphasic poroelastic problems," Proceedings of the Institution of Mechanical Engineers. Part H, Journal of engineering in medicine, 210(2), pp. 131-136.

[137] van der Voet, A. F., 1997, "A comparison of finite element codes for the solution of biphasic poroelastic problems," Proceedings of the Institution of Mechanical Engineers, Part H: Journal of Mechanical Engineering Science, 211(2), pp. 209-211.

[138] van der Voet, A. F., Shrive, N. G., and Schachar, N. S., 1993, "Numerical modelling of articular cartilage in synovial joints - poroelasticity and boundary conditions," Computer methods in biomechanics and biomedical engineering, J. Middleton, G. N. Pande, and K. R. Willimas, eds., IBJ Publishers, Swansea, pp. 200-209.

[139] Wu, J. Z., Herzog, W., and Epstein, M., 1998, "Evaluation of the finite element software ABAQUS for biomechanical modelling of biphasic tissues " Journal of Biomechanics, 31(2), pp. 165-169.

[140] Argoubi, M., and Shirazi-Adl, A., 1996, "Poroelastic creep response analysis of a lumbar motion segment in compression," Journal of Biomechanics, 29(10), pp. 1331-1339.

[141] Federico, S., Rosa, G. L., Herzog, W., and Wu, J. Z., 2004, "Effect of fluid boundary conditions on joint contact mechanics and applications to the modeling of osteoarthritic joints," Journal of Biomechanical Engineering, 126(2), pp. 220-225.

[142] Ferguson, S. J., Bryant, J. T., Ganz, R., and Ito, K., 2000, "The influence of the acetabular labrum on hip joint cartilage consolidation: a poroelastic finite element model," Journal of Biomechanics, 33(8), pp. 953-960.

[143] Korhonen, R. K., Wong, M., Arokoski, J., Lindgren, R., Helminen, H. J., Hunziker, E. B., and Jurvelin, J. S., 2002, "Importance of the superficial tissue layer for the indentation stiffness of articular cartilage," Medical engineering & physics, 24(2), pp. 99-108.

[144] Hibbitt, Karlsson, and Sorensen, 2006, "Abaqus Documentation."

[145] Belytschko, T., Liu, W. K., and Moran, B., 2000, Nonlinear finite elements for continua and structures, John Wiley and Sons, Inc., NYC.

[146] Holzapfel, G. A., 2000, Nonlinear solid mechanics, John Wiley and Sons Ltd., West Sussex, England.

[147] Taber, L. A., 2004, Nonlinear Theory of Elasticity: Applications in Biomechanics, World Scientific Publishing Co., Singapore.

[148] Jacobs, C. R., 1994, "Numerical simulation of bone adaptation to mechanical loading," Stanford University.

[149] Morrissy, R. T., and Weinstein, S. L., 2001, Lovell and Winter's Pediatric Orthopaedics, Lippincott Williams & Wilkins, Philadelphia.

[150] Klein, T. J., Chaudhry, M., Bae, W. C., and Sah, R. L., 2007, "Depth-dependent biomechanical and biochemical properties of fetal, newborn, and tissue-engineered articular cartilage," Journal of Biomechanics, 40(1), pp. 182-190.

[151] Williamson, A. K., Chen, A. C., and Sah, R. L., 2001, "Compressive properties and function-composition relationships of developing bovine articular cartilage," Journal of Orthopaedic Research, 19(6), pp. 1113 - 1121.

[152] Treppo, S., Koepp, H., Quan, E. C., Cole, A. A., Kuettner, K. E., and Gordinsky, A. J., 2000, "Comparison of biomechanical and biochemical properties of cartilage from human knee and ankle pairs," Journal of Orthopaedic Research, 18(5), pp. 739-748.

[153] Grodzinsky, A. J., 1983, "Electromechanical and physicochemical properties of connective tissue," Critical Reviews in Biomedical Engineering, 9(2), pp. 133-199.

[154] Mow, V. C., Ratcliffe, A., and Poole, A. R., 1992, "Cartilage and diarthrodial joints as paradigms for hierarchical materials and structures," Biomaterials, 13(2), pp. 67-97.

[155] Kiviranta, P., Rieppo, J., Korhonen, R. K., Julkunen, P., Toyras, J., and Jurvelin, J. S., 2006, "Collagen network primarily controls Poisson's ratio of bovine articular cartilage in compression," Journal of Orthopaedic Research, 24(4), pp. 690 - 699.

[156] Bank, R. A., Soudry, M., Maroudas, A., Mizrahi, J., and TeKoppele, J. M., 2000, "The increased swelling and instantaneous deformation of osteoarthritic cartilage is highly correlated with collagen degradation," Arthritis and Rheumatism, 43(10), pp. 2202-2210.

[157] Ficklin, T., Thomas, G., Barthel, J. C., Asanbaeva, A., Thonar, E. J., Masuda, K., Chen, A. C., Sah, R. L., Davol, A., and Klisch, S. M., 2007, "Articular cartilage mechanical and biochemical property relations before and after in vitro growth," Journal of Biomechanics, 40(16), pp. 3607-3014.

[158] Kelly, D. J., Crawford, A., Dickinson, S. C., Sims, T. J., Mundy, J., Hollander, A. P., Prendergast, P. J., and Hatton, P. V., 2007, "Biochemical markers of the mechanical quality of engineered hyaline cartilage," Journal of Materials Science: Materials in Medicine, 18(2), pp. 273-281.

[159] Khalsa, P. S., and Eisenberg, S. R., 1997, "Compressive behavior of articular cartilage is not completely explained by proteoglycan osmotic pressure," Journal of Biomechanics, 30(6), pp. 589-594.

[160] Maroudas, A., Wachtel, E., Grushko, G., Katz, E. P., and Weinberg, P., 1991, "The effect of osmotic and mechanical pressures on water partitioning in articular cartilage," Biochimica et Biophysica Acta, 1073(2), pp. 285-294.

[161] van Turnhout, M. C., Kranenbarg, S., and van Leeuwen, J. L., 2010, "Contribution of postnatal collagen reorientation to depth-dependent mechanical properties of articular cartilage," Biomechanics and Modeling in Mechanobiology, June 6 (Epub ahead of print).

[162] Williams, G. M., Dills, K. J., Flores, C. R., Stender, M. E., Stewart, K. M., Nelson, L. M., Chen, A. C., Masuda, K., Hazelwood, S. J., Klisch, S. M., and Sah, R. L., 2010, "Differential regulation of immature articular cartilage compressive moduli and Poisson's ratios by in vitro stimulation with IGF-1 and TGF-beta1," Journal of Biomechanics, 43(13), pp. 2501-2507.

[163] Wilson, W., Huyghe, J. M., and van Donkelaar, C. C., 2007, "Depth-dependent compressive equilibrium properties of articular cartilage explained by its composition," Biomechanics and Modeling in Mechanobiology, 6(1-2), pp. 43-53.

[164] Mow, V. C., Ratcliffe, A., and Poole, A. R., 1992, "Cartilage and diarthrodial joints as paradigms for hierarchical materials and structures," Journal of Biomaterials, 13(2), pp. 67-97.

[165] Mahmoodian, R., Leasure, J., Gadikota, H., Capaldi, F., and Siegler, S., 2009, "Mechanical properties of human fetal talus," Clinical Orthopaedics and Related Research, 467(5), pp. 1186-1194.

[166] Cohen, B., Chorney, G. S., Phillips, D. P., Dick, H. M., and Mow, V. C., 1994, "Compressive stress-relaxation behavior of bovine growth plate may be described by the nonlinear biphasic theory," Journal of Orthopaedic Research, 12(6), pp. 804-813.

[167] Kempson, G., Spivey, C., Swanson, S., and Freeman, M., 1971, "Patterns of cartilage stiffness on normal and degenerate human femoral heads," Journal of Biomechanics, 4(6), pp. 597-609.

[168] Hayes, W. C., and Mockros, L. F., 1971, "Viscoelastic properties of human articular cartilage," Journal of Applied Physiology, 31(4), pp. 562-568.

[169] Hori, R. Y., and Mockros, L. F., 1976, "Indentation tests of human articular cartilage," Journal of Biomechanics, 9(4), pp. 259-268.

[170] Sergerie, K., Lacoursiere, M.-O., Levesque, M., and Villemure, I., 2009, "Mechanical properties of the porcine growth plate and its three zones from unconfined compression tests," Journal of Biomechanics, 42(4), pp. 510-516.

[171] Wong, M., Ponticiello, M., Kovanen, V., and Jurvelin, J. S., 2000, "Volumetric changes of articular cartilage during stress relaxation in unconfined compression," Journal of Biomechanics, 33, pp. 1049-1054.

[172] Armstrong, C. G., and Mow, V. C., 1982, "Variations in the intrinsic mechanical properties of human articular cartilage with age, degeneration, and water content," The Journal of Bone and Joint Surgery, 64(1), pp. 88-94.

[173] Williamson, A. K., Chen, A. C., and Sah, R. L., 2001, "Compressive properties and function-composition relationships of developng bovine articular cartilage," Journal of Orthopaedic Research, 19(6), pp. 1113 - 1121.

[174] Goldsmith, A. A., Hayes, A., and Clift, S. E., 1996, "Application of finite elements to the stress analysis of articular cartilage," Medical engineering & physics, 18(2), pp. 89-98.

[175] Suh, J. K., and Spilker, R. L., 1994, "Indentation analysis of biphasic articular cartilage: nonlinear phenomena under finite deformation," Journal of Biomechanical Engineering, 116(1), pp. 1-9.

[176] 2003, Clubfoot: Ponseti management, Global-HELP Publication.

[177] Cahuzac, J. P., Baunin, C., Luu, S., Estivalezes, E., and Gauzy, J. S. d., 1999, "Assessment of hindfoot deformity by three dimensional MRI in infant club foot," The Journal of Bone and Joint Surgery (British), 81(1), pp. 97-101.

[178] Itohara, T., Sugamoto, K., Ohno, N. S. I., Tanaka, H., Nakajima, Y., Sato, Y., and Yoshikawa, H., 2005, "Assessment of the three-dimensional relationship of the ossific nuclei and cartilaginous anlagen in congenital clubfoot by 3-D MRI," Journal of Orthopaedic Research, 23(5), pp. 1160-1164.

[179] Heywood, A., 1964, "The mechanics of the hindfoot in clubfoot as demonstrated radiographically," The Journal of Bone and Joint Surgery (British), 46, pp. 102-107.

[180] Simons, G., 1978, "A standardized method for evaluation of clubfeet," Clinical Orthopaedics and Related Research, 135, pp. 107-118.

[181] Beatson, T. R., and Pearson, J. R., 1966, "A method of assessing correction in clubfeet," The Journal of Bone and Joint Surgery (British), 48(1), pp. 40-50.

[182] Ponseti, I. V., El-Khoury, G. Y., Ippolito, E., and Weinstein, S. L., 1981, "A radiographic study of skeletal deformities in treated clubfeet," Clinical Orthopaedics and Related Research, 160, pp. 30-42.

[183] Vanderwilde, R., Staheli, L. T., Chew, D. E., and Malagon, V., 1988, "Measurements on radiographs of the foot in normal infants and children," The Journal of Bone and Joint Surgery (American), 70(3), pp. 407-415.

[184] Pauwels, F., 1940, "Eine neue theorie über den einflu mechanischer reize auf die differenzierung der stützgewebe," Z. Anat. Entwickl. Gesch, 121, pp. 478-515 [Transl. 1980 A new theory concerning the influence of mechanical stimuli on the differentiation of the supporting tissues. In Biomechanics of the Locomotor Apparatus (eds P. Maquet , R. Furlong), pp. 375–407, Springer, Berlin]

[185] Carter, D. R., Orr, T. E., Fyhrie, D. P., and Schurman, D. J., 1987, "Influences of mechanical stress on prenatal and postnatal skeletal development," Clinical Orthopaedics and Related Research, 219, pp. 237-250.

[186] Hall, B. K., 1968, "In vitro studies on the mechanical evocation of adventitious cartilage in the chick," Journal of Experimental Zoology, 168(3), pp. 283–305.

[187] Hall, B. K., 1972, "Immobilization and cartilage transformation into bone in the embryonic chick," The Anatomical Record, 173(4), pp. 391-403.

[188] de-Rooij, P. P., Siebrecht, M. A. N., Tägil, M., and Aspenberg, P., 2001, "The fate of mechanically induced cartilage in an unloaded environment," Journal of Biomechanics, 34(7), pp. 961-966

[189] Prendergast, P. J., and Huiskes, R., 1996, "Finite element analysis of fibrous tissue morphogenesis — A study of the osteogenic index with a biphasic approach " Mechanics of Composite Materials, 32(2), pp. 144-150.

[190] Carter, D. R., Rapperport, D. J., Fyhrie, D. P., Schurman, D. J., and Orr, T. E., 1986, "Mechanical regulation of the chondro-osseous skeleton," Orthopaedic Transactions, 10, pp. 325-327.

[191] Agrawal, P., Atre, P. R., and Kulkarni, D. S., 1984, "The role of cartilage canals in in the ossification of talus," Acta Anatomica (Basel), 119(4), pp. 238-240.

[192] Cheng, X., Wang, Y., and Qu, H., 1997, "Intrachondral microvasculature in the human fetal talus," Foot & Ankle International, 18(6), pp. 335-338.

[193] Ben-Menachem, Y., and Butler, J. E., 1974, "Arteriography of the foot in congenital deformities," The Journal of Bone and Joint Surgery (American), 56(8), pp. 1625-1630.

[194] Dobbs, M. B., Gordon, J. E., and Schoenecker, P. L., 2004, "Absent posterior tibial artery associated with idiopathic clubfoot. A report of two cases.," The Journal of Bone and Joint Surgery (American), 86(3), pp. 599–602.

[195] Greider, T. D., Siff, S. J., Gerson, P., and Donovan, M. M., 1982, "Arteriography in club foot," The Journal of Bone and Joint Surgery (American), 64(6), pp. 837-840.

[196] Kitziger, K., and Wilkins, K., 1991, "Absent posterior tibial artery in an infant with talipes equinovarus," Journal of Pediatric Orthopaedics, 11(6), pp. 777–778.

[197] Quillin, S. P., and Hicks, M. E., 1994, "Absent posterior tibial artery associated with clubfoot deformity: an unusual variant," Journal of Vascular and Interventional Radiology, 5(3), pp. 497-499.

[198] Sodre, H., Bruschini, S., Mestriner, L. A., Jr, F. M., Levinsohn, E. M., Packard, D. S., Jr, R. J. C., Schwartz, R., and Hootnick, D. R., 1990, "Arterial abnormalities in talipes equinovarus as assessed by angiography and the Doppler technique," Journal of Pediatric Orthopaedics, 10(1), pp. 101-104.

[199] Kruse, L., Gurnett, C. A., Hootnick, D., and Dobbs, M. B., 2009, "Magnetic resonance angiography in clubfoot and vertical talus: a feasibility study," Clinical Orthopaedics and Related Research, 467(5), pp. 1250-1255.

[200] Haliburton, R. A., Sullivan, C. R., Kelly, P. J., and PETERSON, L. F., 1958, "The extra-osseous and intra-osseous blood supply of the talus," The Journal of Bone and Joint Surgery (American), 40(5), pp. 1115-1120.

[201] Mulfinger, G. L., and Trueta, J., 1970, "The blood supply of the talus," The Journal of Bone and Joint Surgery, 52(1), pp. 160-167.

[202] Ponseti, I. V., 1998, "Correction of the talar neck angle in congenital clubfoot with sequential manipulation and casting," The Iowa Orthopaedic Journal, 18, pp. 74-75.

[203] Wilson, W., Donkelaar, C. C. v., Rietbergen, B. v., and Huiskes, R., 2005, "A fibril-reinforced poroviscoelastic swelling model for articular cartilage," Journal of Biomechanics, 38(6), pp. 1195-1204.

APPENDIX A. DEFINITION OF FOOT MOTIONS AND DEFORMITIES

The three foot segments (forefoot, midfoot, and hindfoot) are linked together by strong ligaments. Because of this linkage, all foot movements occur concurrently. The following are the definitions of motions and deformities of the foot.

- Supination/Pronation: combination movements in the individual foot joints. Supination refers to the sole pointing inward, and pronation refers to sole turning outward (Figure A-1).

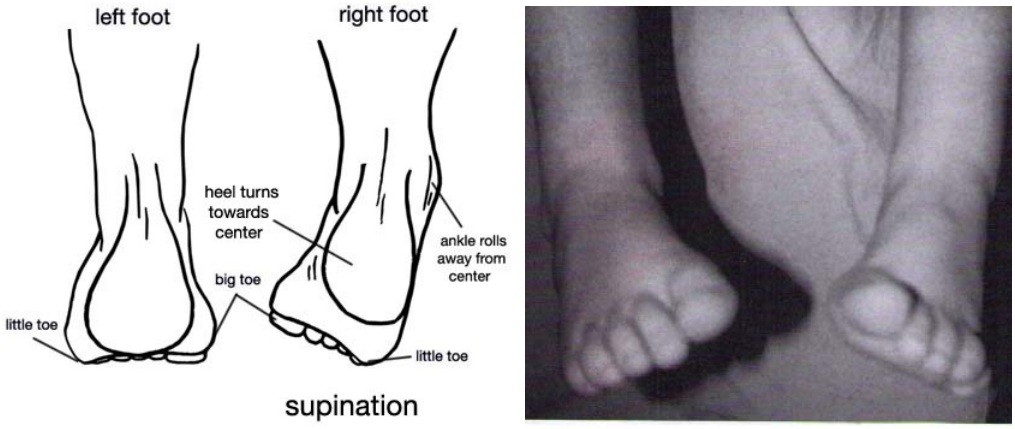

Figure A.1. Foot Supination: sole turning inward (From Turek's Orthopaedics [1]).

- Varus (inversion)/Valgus (eversion): motions of a foot segment on a theoretic longitudinal axis (Figures A-2, A-3).

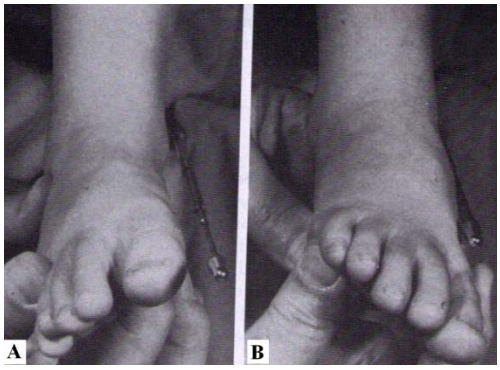

Figure A.2. Forefoot varus (inversion; A) and forefoot valgus (eversion; B). (From Turek's Orthopaedics [1]).

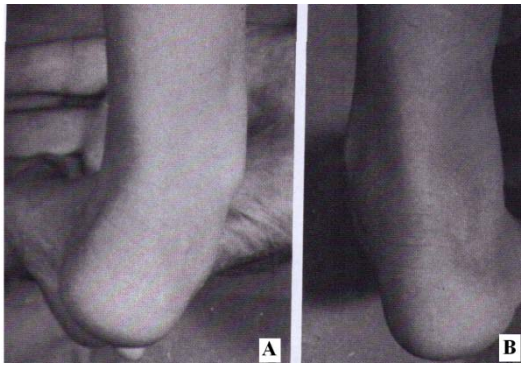

Figure A.3. (A) Heel valgus (eversion) when foot is pronated, (B) Heel varus (inversion) when foot is supinated (From Turek's Orthopaedics [1]).

- Adduction/Abduction: motions of the foot segment on a theoretic vertical axis (Figure A-4).

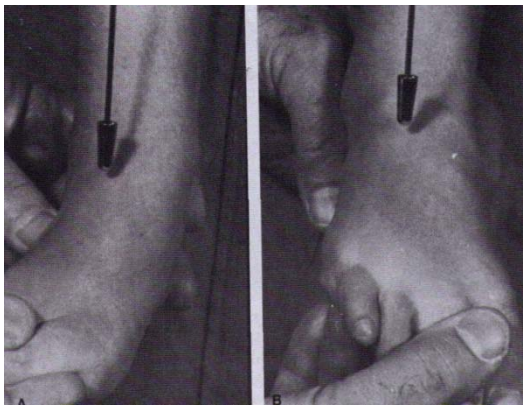

Figure A.4. (A) Forefoot adduction, (B) forefoot abduction (From Turek's Orthopaedics [1]).

Figure A.5. Equinus.

- Equinus: a congenital deformity of the foot in which the sole is permanently flexed so that walking is done on the toes without touching the heel to the ground – normally due to tight heel cord and shortened calf muscles (Figure A-5).

- Cavus: a foot deformity characterized by an abnormally high arch due to fixed plantar flexion of the forefoot. Because of this high arch, an excessive amount of weight is placed on the ball and heel of the foot when standing (figure A-6).

Figure A.6. (A) Normal foot, (B) Cavus deformity.

APPENDIX B. ANATOMICAL PLANES AND DIRECTIONS

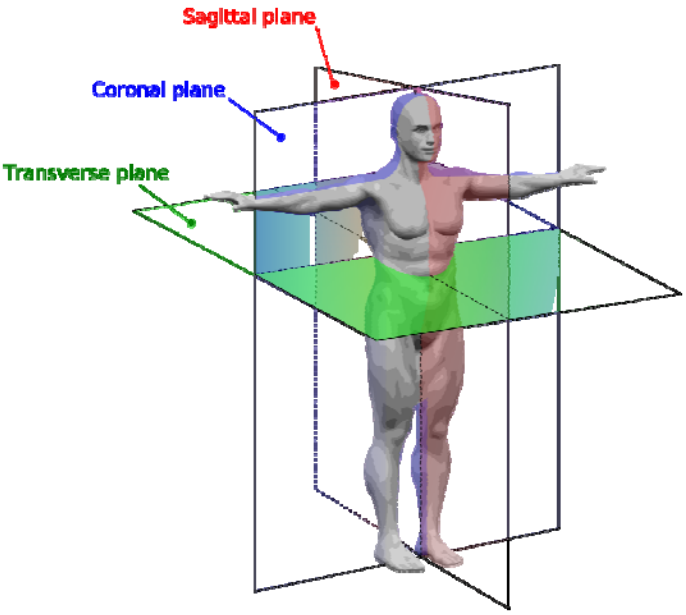

Figure B.1. Anatomical planes (From Wikipedia).

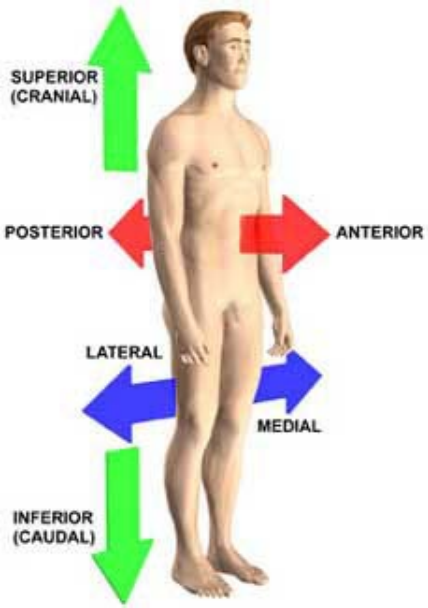

Figure B.2. Anatomical directions (From Wikipedia).

- Proximal: where the appendage joins the body; Distal: toward furthest from the point of attachment to the body.
- Anterior: toward the front (belly) of the body; Posterior (dorsal): toward the back of the body.
- Medial: toward the midline of the body; Lateral: toward the side of the body.
- Superior (above): in a higher position; Inferior (below): in a lower position.
- Cranial: toward the head; Caudal: toward the lower end of the spine.
- Ventral: pertaining to the front or anterior of any structure. The ventral surfaces of the body include the chest, abdomen, shins, palms, and soles; Dorsal: relating to the back or

posterior of a structure. Some of the dorsal surfaces of the body are the back, buttocks, calves, and the knuckle side of the hand.

VITA

Education

***Drexel University**, College of Engineering* — *Philadelphia, PA*
Ph.D., Mechanical Engineering and Mechanics — Dec. 2010
Dissertation Title: Mechanics and development of tarsal cartilage anlagen – Insights from a human study

***University of Virginia**, School of Engineering and Applied Science* — *Charlottesville, VA*
M.S., Mechanical and Aerospace Engineering — Aug. 2006
Thesis Title: Formal parameter estimation for self-sensing magnetic bearings

***University of Tehran**, School of Engineering* — *Tehran, Iran*
B.S., Mechanical Engineering — Mar. 2004
Thesis Title: Design, fabrication and control of a ball-on-beam balancer system

Journal Publications

R. Mahmoodian, J. Leasure, P. Philip, N. Pleshko, F. Capaldi, R. Brand, S. Siegler, "Changes in the mechanics and composition of human talar cartilage anlage during fetal development," *Osteoarthritis and Cartilage*, 2011 (Accepted).
R. Mahmoodian, S. Siegler, F. Capaldi, "A finite element implementation of the finite deformation biphasic theory," (In review).
R. Mahmoodian, S. Siegler, F. Capaldi, J. Leasure, H. Gadikota, "Mechanical properties of human fetal talus," *Clinical Orthopaedic Research and Related Research*. Vol. 467, 1186-1194, 2009.
E. Maslen, T. Iwasaki, and **R. Mahmoodian**, "Field and gap estimation in magnetic bearings: a Lyapunov approach," *Journal of the Japan Society of Applied Electromagnetics and Mechanics*, Vol. 16, 256-265, 2008.

Conference Proceedings, Presentations, and Posters

R. Mahmoodian, S. Siegler, "Development of a finite element framework for studying growth of cartilage anlage," *ASME Summer Bioengineering Conference*, 2009, Lake Tahoe, CA (Poster).
R. Mahmoodian, J. Leasure, S. Siegler, F. Capaldi, "Characterization of compressive behavior of developing human talus," *Proceedings of the ASME International Mechanical Engineering Congress and Exposition*, 2008, Boston, MA (Presentation).
R. Mahmoodian, S. Siegler, "Effect of Ponseti technique on development of tarsal bones in clubfoot patients," *Drexel Engineering Research Symposium*, 2007, Drexel University, Philadelphia, PA (Poster).
R. Mahmoodian, S. Siegler, "Effect of loads applied to the infant clubfoot through serial casting on shape, growth and ossification of hindfoot anlagen," *Drexel Research, Innovation, Scholarship, and Creativity Day*, 2007, Drexel University, Philadelphia, PA (Poster).
R. Mahmoodian, S. Siegler, "An MRI based study of tarsal development during manipulation and casting therapy of infant clubfoot," *Proceedings of the ASME International Mechanical Engineering Congress and Exposition*, 2007, Seattle, WA (Presentation).

Honors

- Nominated for the College of Engineering award for academic excellence — 2008
- Dissertation Award from the International Society of Biomechanics — 2007
- Fellowship of the University of Virginia — 2004
- Award of the School of Engineering of the University of Tehran for outstanding results in the public universities' entrance exam and maintaining academic excellence — 1999, 2000
- Ranked 190th among more than 250,000 participants in the nationwide public universities' entrance exam for undergraduate studies. — 1999
- Silver Medal in the National Physics Olympiads — 1998